Converting quantum information to mechanical motion

by

Adam P. Reed

B.S., The Ohio State University, 2011

M.S., University of Colorado, 2015

A thesis submitted to the

Faculty of the Graduate School of the

University of Colorado in partial fulfillment

of the requirements for the degree of

Doctor of Philosophy

Department of Physics

2017

This thesis entitled:
Converting quantum information to mechanical motion
written by Adam P. Reed
has been approved for the Department of Physics

Konrad Lehnert

John Teufel

Date

The final copy of this thesis has been examined by the signatories, and we find that both the content and the form meet acceptable presentation standards of scholarly work in the above mentioned discipline.

Reed, Adam P. (Ph.D., Physics)

Converting quantum information to mechanical motion

Thesis directed by Prof. Konrad Lehnert

Mechanical systems that combine motion and electricity are often used to process information. They are employed as compact clocks, filters, and sensors in almost all modern electronic devices. Yet these devices are limited to processing classical information. To exploit mechanical systems in emerging quantum communication and computation technologies, such systems must process fragile quantum bits of information. In this thesis, I experimentally demonstrate the conversion of quantum bits encoded in electrical signals to the motion of a micron-scale mechanical resonator. This capability is crucial for harnessing mechanical systems as memories for quantum signals, or as converters of information between electronic quantum processors and telecommunications light. Beyond quantum information processing, this work opens up the possibility to test quantum theory in objects of an unprecedented mass scale.

Dedication

To my family

Acknowledgements

I'd like to thank my PhD mentor Konrad Lehnert who worked with me since I started graduate school in 2011. Konrad taught me many things about low-temperature physics and microwave engineering, and more importantly he showed me how to grow as a scientist. He also taught me how to effectively communicate scientific ideas to my peers and the community. Furthermore, he was willing to consider new ideas and ways to solve any sort of challenge that emerged during my time in graduate school. All of these qualities will serve me well beyond the work in his lab.

In addition to Konrad, I've been very grateful to have John Teufel as my second mentor during graduate school. John was always willing to take the time to chat with me when I was learning about electromechanics or trying find a direction for my thesis work. His patience and positive attitude was a constant source of encouragement that kept my spirits high.

I'd also like to thank Cindy Regal, Dave Wineland, and Zoya Popovich for serving on my PhD defense committee. In particular, I'd like to thank Dave Wineland for providing thoughtful revisions to my thesis.

I'm very grateful for our theory collaborators at NIST. In particular, I'm indebted to Karl Mayer for his contributions to this thesis. Karl was always very patient when I asked silly theory questions, and he provided thorough yet easy to understand answers. He also took the responsibility to greatly improve upon my initial data analysis methods. Additionally, I'd like to thank Scott Glancy and Manny Knill for carefully reading our manuscript and providing valuable feedback.

I'd like to thank many other collaborators at NIST. Florent Lecocq has kindly shared his knowledge of quantum circuits with me. He also mentored me while I was designing my thesis

experiment, and provided valuable feedback regarding my very rough manuscript drafts. Manuel Castellanos-Beltran helped me understand the limitations of JPAs, and taught me the nuances of commercial microwave test equipment. Kat Cicak helped me with fabrication and related work in the NIST clean room. Additionally, I'd like to thank Leila Vale and Martin Sandberg for showing me how to process Josephson junctions at NIST.

At JILA, I'd like to thank Michael Schroer and Will Kindel for getting me started in the superconducting qubit world. Michael showed me how to set up a qubit experiment from scratch, and how to execute many important qubit measurements. Will not only developed the qubit-based photon source used in this thesis, but also taught me how make my own source and integrate it with our electromechanics experiments.

It has been a pleasure working with many other current and former Lehnert lab members. Jen Harlow taught me how to analyze microwave circuits when I first joined the lab. She also thoughtfully mentored me while I was searching for a thesis topic. Reed Andrews showed me how to attack problems from new angles, and taught me effective troubleshooting skills both in the clean room and in the lab. Tauno Palomaki was always very patient when I asked him endless questions about his experiment. Brad Mitchell joined me in our efforts to adopt and understand waveguide microwave cavities for use in our lab. Lucas Sletten and Xizheng Ma patiently pushed forward our efforts to operate cavities and qubits with long coherence times. Rob Delaney spearheaded new ways to operate our electromechanical device as an amplifier.

I'd also like to thank everyone else who has supported me in the Lehnert lab: Andrew Higginbotham, Brad Moores, Max Malnou, Jeremie Viennot, Joe Kerchoff, Hsiang-Sheng Ku, Pete Burns, Dan Palken, Ben Chapman, Eric Rosenthal, Max Urmey, Nicole Ehrlich, Tim Menke, Mehmet Anil, and Gerwin Koolstra. In many ways, my lab mates have helped me out on a day-to-day basis and have served as a source of encouragement during my time in graduate school.

I've also had the pleasure to learn optics knowledge from Bob Peterson, Tom Purdy, and Ben Yu in the Regal lab.

JILA has a unique and amazing set of technical shops, and I benefited from their expertise.

The members of the electronics shop have helped me design and build many custom pieces of electronics. The members of the machine shop not only built many things for our lab and provided their technical support, but also taught me many important machine shop skills.

Additionally, members of the computing services have helped me out on numerous occasions when I had to deal with the agonies of software. In particular, I'd like to thank the computer wizard JR for helping me connect up the network of computers used in our experiment.

I'd like to thank Mark Carter for going out of his way to ensure that our experiments always had enough liquid helium to keep them running. In the extraordinary event that liquid helium was not available, Ted Stauffer at NIST and Dave Erikson at JILA went out of their way to help me safely move a Dewar of liquid helium from NIST to JILA just to keep my experiment running.

In addition to my colleagues in Boulder, I'm very grateful have the opportunity to collaborate with Rob Schoelkopf and his team at Yale. This extraordinary team is world-class and friendly. Matt Reagor got me off the ground with the collaboration, and was always willing to patiently answer my numerous questions about operating transmon qubits. Luke Burkhart fabricated the awesome transmon qubit used in this thesis, and answered many questions about it. Wolfgang Pfaff provided his expertise in creating flying microwave quantum states. Chris Axline shared with me many important experimental details. Luigi Frunzio enthusiastically helped me troubleshoot many of the issues we had when shipping transmon qubits from Yale to JILA.

Outside the lab I've had the good fortune to discuss my experiments with Karl Mayer, Bryce Bjork, Steven Moses, and Rabin Paudel. And we enjoyed home-brewing many beers together, too.

Lastly, I'd like to thank my family for their support and encouragement as I pursed my interests in experimental physics. My mom and dad were very patient as I built trebuchets, lasers, Tesla coils, rockets, and many other things that could have killed me when I was young. My life-long partner Li-Wei Hung not only introduced me to powerful statistical analysis methods when I was trying to understand my data, but more importantly, she also supported me throughout the inevitable ups and downs of graduate school. Her love and support drove me to finish this thesis.

Contents

Chapter

Tables

Table

Figures

Figure

Chapter 1

Introduction

Motion contains information. In 1797, this simple idea enabled Henry Cavendish to accurately measure – for the first time – Earth's mass using mechanical motion[1]. His approach was to measure the gravitational interaction between two lead balls. One of the balls was freely suspended, and its motion was measured using light. Cavendish used the suspended ball to convert the force of gravity to mechanical motion. From motion, he gained information about the mass of Earth.

Light also contains information. And remarkably, it can be converted to motion. Even a century before Cavendish's famous experiment, Johannes Kepler made the observation that a comet's tail points away from the sun[2]. Put in another way, the deflection of the comet's tail contains information about the direction of the sun's rays[3]. This strange behavior was not rigorously explained until 1873 when Maxwell developed the theory of electromagnetism, which predicted that light can move objects[4]. By 1901, Maxwell's prediction was quantitatively verified by experiments that measured the displacement of vanes mounted on a spindle as they were illuminated with the gentle touch of light[5, 6]. However, these experiments suffered from thermal effects that obscured motion due to light.

By the 1970s, the invention of the laser led to a new era of manipulating objects using light. Because the laser provided high intensity light, it could easily trap and accelerate freely suspended dielectric spheres micrometers in diameter[7]. This advance inspired proposals aimed at harnessing light to trap and cool the motion of single atoms[8, 9, 10]. Such ideas were utilized in experiments that used laser light to damp the motion of a trapped atom[11, 12], which enabled cooling of an

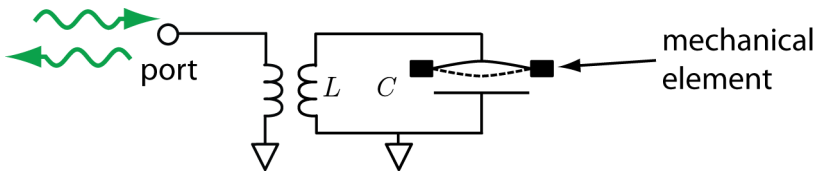

Figure 1.1: Schematic of an electromechanical device. A mechanical element forms part of a capacitor (C) which is shunted by an inductor (L). These two elements form an electrical resonant circuit that is inductively coupled to a transmission line. Propagating electrical signals (green) are injected into a port.

atom to its lowest possible energy state of motion[13]. This technique of laser cooling is now the workhorse of many atomic physics experiments in laboratories around the world, including ones here in Boulder at the National Institute of Standards and Technology (NIST) and JILA.

Apart from laser cooling, converting information between mechanical motion and light was studied in the context of improving the sensitivity of early gravitational wave detectors. Initial efforts in the 1960s made detectors using massive vibrating bars coupled to electrical circuits[14, 15, 16]. While controversial, such efforts inspired a new type of gravitational wave detector that used light to measure motion[17, 18]. The basic idea was to measure the disturbance caused by a gravitational wave on suspended masses in a laser interferometer. This led to the development of the Laser Interferometer Gravitational Wave Observatory (LIGO) which would – because of immensely heroic and resilient efforts – directly measure the amplitude and phase of a gravitational wave for the first time[19]. This stunning result provided a surprising amount of information about black holes billions of light years away from Earth[20].

The development of gravitational wave detectors – spanning over 40 years – led to fantastic progress in the understanding of how light and motion fundamentally affect each other. Experiments in the 1970s revealed that light shined on a mirror could not only move it, but also damp or amplify its motion[21]. As experimenters pushed the sensitivity of interferometers, it was discovered that quantum mechanics may limit how much information can be gained from motion[22, 23, 24]. From these investigations emerged the parallel fields of cavity optomechanics and circuit electromechanics[25, 26, 27]. Their aim is to advance fundamental science and technology by

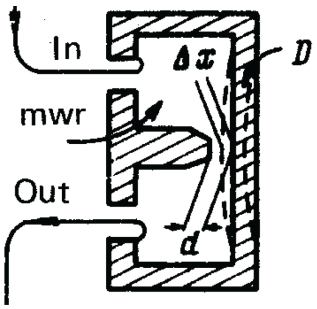

Figure 1.2: Schematic of an early electromechanical device. A microwave cavity (mwr) is covered by a flexible metal diaphragm (D) which forms a small capacitive gap (d). Mechanical displacements Δx of the diaphragm modulate microwave fields in the cavity. Image reproduced from Ref. [23].

harnessing light or electricity to manipulate mechanical motion. In this thesis, I will focus on circuit electromechanics.

A schematic of a circuit electromechanical system is shown in Fig. 1.1. The circuit is formed by an inductor (L) and capacitor (C) which resonate at the frequency defined by $\omega_0/2\pi = 1/(2\pi\sqrt{LC})$. The upper plate of the capacitor is a flexible element which is free to vibrate. Because the capacitance depends on the separation of the two plates, motion of the upper capacitor plate will modulate the electrical resonance. By injecting electrical signals into the circuit and measuring its response, information about the motion of the capacitor plate can be gained.

The initial goals of circuit electromechanics were to develop methods for measuring small mechanical displacements of macroscopic objects. In the early 1980s, an early electromechanical device consisted of a centimeter-sized bulk niobium cavity with a flexible diaphragm[23]. This device relies on the parametric coupling between motion and electricity in which vibrations of the flexible diaphragm modulate the resonant frequency of the cavity, as diagrammed in Fig. 1.2. Remarkably, the level of performance achieved was better than any optical methods for measuring displacements at the time. By the 1990s, advances in microfabrication techniques – due to the booming silicon industry – led to a drastic miniaturization of mechanical elements to the nanometer and micrometer scale. These capabilities enabled experiments to construct sensitive detectors by coupling micrometer- and nanometer-scale mechanical resonators to single-electron

transistors[28, 29, 30], atomic point contacts[31, 32], superconducting circuits[33, 34, 35], piezoelectric materials[36, 37], and even single-electron spins[38]. Apart from improving detectors, theoretical proposals emerged[39, 40, 31, 41, 42, 43, 44, 45, 46] that aimed to use circuit electromechanics to observe quantum states of motion in a macroscopic object for quantum information processing and foundational tests of quantum theory. A prerequisite to accessing quantum states of motion is the ability to cool mechanical motion to its quantum ground state.

Cooling mechanical motion to its quantum ground state requires minimizing undesired thermal effects that will obscure quantum behavior. For a mechanical resonator that oscillates at ω_{m} and is at a temperature T, reaching the ground state of motion requires reducing the resonator's thermal energy $k_{\mathrm{B}}T$ so that it is far below the mechanical quanta of energy $\hbar\omega_{\mathrm{m}}$ where k_{B} is the Boltzmann constant and $\hbar$ is the reduced Planck constant. In 2010, experimenters cooled a piezoelectric mechanical resonator that oscillates at $\omega_{\mathrm{m}}/2\pi \approx 6$ GHz to an environment temperature of $T < 100$ mK. This low temperature enabled the single 6-GHz mechanical mode to occupy its quantum ground state approximately 93% of the time[37]. Instead of simply reducing the environment temperature of the resonator, one can use optical or microwave fields to cool the motion to its quantum ground state. This idea spawned intense efforts both theoretically[47, 48] and experimentally[49, 50, 51, 34, 52] to develop methods – borrowed from early experiments with trapped ions[13] – for reaching the quantum quantum state of motion in a macroscopic object. When I started graduate school in 2011, two experiments reached this regime. One experiment used microwave fields to cool the motion of a micrometer-scale aluminum membrane in a microwave-frequency superconducting circuit[53]. A separate experiment used optical fields to cool the motion of a nanometer-scale crystal in a photonic cavity[54].

The ability to prepare mechanical motion in its ground state enabled experiments to probe profoundly quantum phenomena in macroscopic objects. One of the most basic phenomena is the inherent fluctuations of a mechanical resonator even while in its ground state. These zero-point fluctuations have been observed in optomechanical[55] and electromechanical[56, 57] devices, and then manipulated to produce squeezed states with displacement fluctuations less than the

resonator's zero-point motion[57, 58, 59]. Furthermore, the zero-point motion of a mechanical resonator was entangled with a propagating microwave field.[60].

These experiments enable electromechanical devices to serve as general-purpose signal processing elements that could be used in emerging quantum communication[61, 62] and modular quantum computing architectures[63]. In a single electromechanical device, the parametric coupling between motion and electricity can be rapidly varied. For example, the ability to suddenly turn off the interaction between electricity and motion allows the state of a propagating field to be converted to, and trapped in, the motion of the resonator[64]. From this ability emerges fantastic practical applications of the electromechanical device, such as an on-demand memory[64], a dynamic signal processing element[65], and a pulsed amplifier[60, 66] for propagating quantum signals. Other experiments have also demonstrated the ability to frequency convert or continuously amplify microwave fields using an electromechancial device[65, 67, 68].

To exploit the aforementioned signal-processing capabilities of an electromechanical device in a general quantum information processor, one must work with states that have non-Gaussian statistics such as a superposition of zero and one photons[69]. These states may enable information processing that cannot be performed classically[70]. Although Gaussian states can be harnessed for certain quantum information tasks[71], any process using only Gaussian states can be simulated efficiently on a classical computer[72]. But in the regime that electromechanical devices operate, the equations that describe the coupling are linear[27]. This linearity ensures that a Gaussian state of the microwave field or mechanical resonator will never evolve into a non-Gaussian state.

Accessing non-Gaussian mechanical states requires either a nonlinear detector such as a single photon counter or a source of non-Gaussian states. In optical systems, single photon counters have been used to generate and measure single-photon states[73]. This technique relies on 'heralding' the presence of a single photon generated by a source of correlated two-photon pairs. In an opto- and electromechanical device, correlated pairs of mechanical quanta – phonons – and photons can be produced[60]. Because the pairs of phonons and photons are correlated, detection of a single photon corresponds to the presence of a single *phonon* occupying the mechanical resonator[74]. For

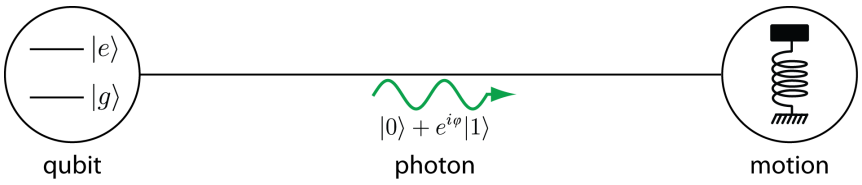

Figure 1.3: A source of quantum information coupled to a mechanical resonator. The source consists of a qubit with a ground $|g\rangle$ and excited state $|e\rangle$. Electrical signals (green) propagate in a transmission line (black). Such signals encode the qubit's state as superpositions of zero and one photons where φ is the phase of the qubit.

an electromechanical device, correlated single photons can in principle be resolved using a superconducting qubit[44, 75, 66]. Similarly, the use of a nonlinear detector has been recently explored in optomechanical systems[76, 77]. If a nonlinear detector is not used, the mechanical resonator can be coupled to a source of non-Gaussian states. This approach enabled an experiment in 2010 to take the first pioneering step towards deterministically converting quantum information from a non-Gaussian source to mechanical motion[37]. Specifically, the source was a superconducting qubit which strongly coupled to a piezoelectric mechanical resonator. However, the few-nanosecond lifetime of the mechanical resonator prohibited tomographic measurements of its state.

The strategy I pursue in this thesis is to exploit a superconducting qubit as a source of propagating photons that carry quantum information to an electromechanical device[78]. A diagram of the experiment concept is shown in Fig. 1.3. In this approach, the qubit and mechanical resonator are in two separate modules. As such, each module can be readily characterized and separately optimized to reach state-of-the-art levels of performance[79, 53]. Communication from the qubit to the mechancial resonator occurs naturally through the use of the propagating microwave-frequency photons. In the optical domain, the use of propagating photons has been considered as a route towards producing non-Gaussian mechanical states[80, 81, 82]. The benefit to working in the microwave domain is that superconducting qubits can deterministically produce arbitrary quantum states[83, 84, 85], which can also be encoded in propagating microwave photons[86].

After encoding the quantum state in a propagating photon, it can be converted to the state

of the mechancial resonator. As an initial test, I use the electromechanical device to capture, store, and amplify single photons generated by a superconducting qubit. To efficiently measure the mechanical state, I developed a new way of operating the electromechanical device as a low-noise amplifier. I exploit this capability in order to determine the density matrix of the mechanical state. I find that the quantum state can be stored on a timescale exceeding 100 μs, an improvement of over four orders of magnitude compared to previous work that demonstrated the storage of a non-Gaussian state in an electromechanical device[37]. To characterize how the capture *process* affects arbitrary propagating qubit states, I use the electromechanical device to capture superpositions of zero and one photons. The degree to which this process preserves quantum information is quantified by the average fidelity[87], which I find to be $F_{\text{avg}} = 0.83^{+0.03}_{-0.06}$ where the limits are the 90% confidence interval. This level of performance exceeds the fidelity achievable using only classical resources, indicating that the electromechanical device is suitable for the transduction of quantum information.

1.1 Thesis contents

Chapter 2 provides a brief introduction to quantum information encoded in continuous and discrete variables. This chapter is not meant to provide a rigorous derivation of the many rich topics in quantum information theory, but rather it introduces ideas that are relevant for subsequent chapters. Chapter 3 describes how incorporating a mechanical resonator in an electrical circuit forms an electromechanical device, which can be used to manipulate propagating microwave fields. Additionally, it describes the characterization of the electromechanical device. Chapter 4 describes how a circuit quantum electrodynamics (cQED) system forms a source of propagating single photons. Additionally, it briefly discusses characterization of the source. Chapter 5 demonstrates the ability to faithfully convert the propagating single photons to motion of the mechanical resonator. Lastly, Chapter 6 provides an outlook for future experiments that may utilize this conversion capability.

Chapter 2

Theory of continuous- and discrete-variable quantum information

Emerging quantum processors and quantum communication networks require the ability to manipulate information encoded in the state of a quantum system[88, 89]. There are numerous physical implementations of such quantum systems that include photons[90], ions[91], nuclear and electronic spins[92, 93, 94], ultracold atoms[95], and superconducting circuits[96]. Among these vastly different systems is a description of quantum information in terms of either a continuous or discrete variable[71, 69]. This dichotomy is analogous to how classical information can be encoded as either an analog or digital signal. To efficiently process and distribute information, virtually all modern computation and communication devices utilize both analog and digital encoding[97]. Similarly, emerging quantum technologies may rely on a combination of discrete- and continuous-variable quantum systems.

This chapter presents a brief overview of continuous- and discrete-variable systems that are relevant for subsequent chapters. Section 2.1 introduces classical and quantum harmonic oscillators, which are continuous-variable systems. Section 2.2 introduces qubits, which are discrete-variable systems. Section 2.3 describes how incorporating a qubit into an electromagnetic resonator can be exploited to generate single photons. Section 2.4 describes how quantum states are generated in stationary modes, and then transmitted using propagating modes in a transmission line. Section 2.5 describes how to characterize a propagating mode using quantum state tomography.

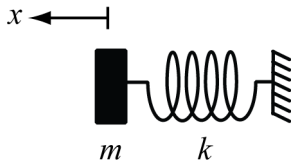

Figure 2.1: A mass connected to a spring.

2.1 Harmonic oscillators as continuous-variables systems

A continuous-variable system encodes quantum information in states that can have a continuum of eigenvalues. In this thesis, I employ two such systems: a mechanical resonator and a microwave field. The mechanical resonator can be described in terms of its position and momentum, whereas the microwave field can be described in terms of its amplitude and phase quadratures[98]. Although these two systems are physically quite different, they can both be modeled as harmonic oscillators.

2.1.1 Classical description

In classical mechanics, the prototypical harmonic oscillator is a mass connected to a spring as diagrammed in Fig. 2.1. The object has a mass m and it experiences a linear restoring force $F = -kx$ where k is the spring constant. Because of this force, the object is harmonically bound. The complete state of the object at time t is described by its position $x(t)$ and momentum $p(t) = mv(t)$ where $v(t)$ is the object's velocity. Both of these variables are governed by

$$\begin{aligned} \dot{p}(t) &= -kx(t) \\ \dot{x}(t) &= \frac{p(t)}{m} \end{aligned} \tag{2.1}$$

which are a set of coupled differential equations written in the Hamiltonian form[99]. If the mass is initially displaced by $x(0)$, solutions to the above equations reveal that its position oscillates at an angular frequency of $\omega = \sqrt{k/m}$ according to $x(t) = x(0)\cos(\omega t)$.

Hamilton's equations explicitly couple position and momentum for the spring-mass system.

To write a pair of equations that are decoupled, complex field amplitudes are used to describe the state of the system. Specifically, appropriate linear combinations of Eqns. 2.1 yield

$$\dot{a}(t) = -i\omega a(t) \quad \text{and} \quad \dot{a}^*(t) = +i\omega a^*(t) \tag{2.2}$$

where

$$a(t) = \frac{\sqrt{m}\omega}{2}\left(x(t) + \frac{ip(t)}{m\omega}\right) \quad \text{and} \quad a^*(t) = \frac{\sqrt{m}\omega}{2}\left(x(t) - \frac{ip(t)}{m\omega}\right) \tag{2.3}$$

are the complex field amplitudes[100]. These amplitudes have been normalized such that $|a(t)|^2$ describes exactly half of the system's total energy, given by $H = T + V$ where $T = p^2/(2m)$ and $V = \omega^2 x^2/2$ are the object's kinetic and potential energies, respectively. The utility of this approach is that the field amplitudes a and a^* are classical analogs of the annihilation and creation operators used in the formalism of the quantum harmonic oscillator.

2.1.2 Quantum description

The quantum analog of a classical harmonic oscillator is described by its total energy, as discussed in Ref. [101]. Briefly, the quantum harmonic oscillator has a total energy given by the Hamiltonian

$$\hat{H}_{\text{ho}} = \frac{\hat{p}^2}{2m} + \frac{1}{2}m\omega^2\hat{x}^2 \tag{2.4}$$

where $\hat{x}$ and $\hat{p}$ are operators that satisfy the canonical commutation relation given by

$$[\hat{x}, \hat{p}] = \hat{x}\hat{p} - \hat{p}\hat{x} = i\hbar \tag{2.5}$$

where $\hbar$ is Planck's constant h divided by 2π. Using this commutator relation, the Hamiltonian for the quantum harmonic oscillator can be cleverly written as

$$\hat{H}_{\text{ho}} = \hbar\omega\left(a^\dagger a + \frac{1}{2}\right) \tag{2.6}$$

where

$$a = \sqrt{\frac{m\omega}{2\hbar}}\left(\hat{x} + \frac{i\hat{p}}{m\omega}\right) \quad \text{and} \quad a^\dagger = \sqrt{\frac{m\omega}{2\hbar}}\left(\hat{x} - \frac{i\hat{p}}{m\omega}\right) \tag{2.7}$$

are the 'annihilation' and 'creation' operators, respectively. As written, they satisfy $[a, a^\dagger] = 1$.

Importantly, the quantum harmonic oscillator has an infinite set of discrete energy states $\{|n\rangle\}$ for any integer $n \geq 0$. Such states are defined by

$$\hat{H}_{\text{ho}} |n\rangle = E_n |n\rangle \tag{2.8}$$

where $E_n = \hbar\omega(n + 1/2)$ is the energy of each state. A given state can be generated using

$$|n\rangle = \frac{(a^\dagger)^n}{\sqrt{n!}}|0\rangle \tag{2.9}$$

where $|0\rangle$ is called the 'vacuum state' which is the state with the lowest allowed energy. Although the vacuum state contains no excitations ($n = 0$), its average energy $\langle 0| \hat{H}_{\text{ho}} |0\rangle = \hbar\omega/2$ is not zero.

To describe the time evolution of the quantum harmonic oscillator, I use the Heisenberg representation[102]. In this representation, the creation and annihilation operators obey the Heisenberg equations of motion given by

$$\dot{a}(t) = \frac{i}{\hbar}[\hat{H}_{\text{ho}}, a(t)] \tag{2.10}$$

and the Hermitian conjugate equation for $a^\dagger(t)$. The solutions to these equations are

$$a(t) = a(0)e^{-i\omega t} \quad \text{and} \quad a^\dagger(t) = a^\dagger(0)e^{i\omega t}. \tag{2.11}$$

In order to remove the free evolution of the amplitudes, it is natural to move into a rotating frame of reference. By making the transformation $a(t) \to a(t)e^{-i\omega t}$, the solutions are $a(0)$ and $a^\dagger(0)$.

In an experiment, the operators $a(0)$ and $a^\dagger(0)$ are not directly measured. Instead, one can employ a nonlinear detector (such as a single-photon counter) to measure the average occupancy $\langle a^\dagger(0)a(0)\rangle$ of the oscillator. Apart from nonlinear detection, one can employ a linear detector (such as a linear amplifier) to sense linear combinations of $a(0)$ and $a^\dagger(0)$ given by

$$X = \frac{1}{2}(a + a^\dagger) \quad \text{and} \quad Y = \frac{1}{2i}(a - a^\dagger) \tag{2.12}$$

which are written in a rotating frame at ω. The above quantities are 'quadrature operators,' and they are essentially dimensionless parameters for the position and momentum of a harmonic oscillator. In Section 2.5, I discuss two detection methods used to measure them.

2.1.3 Quantum states

An infinite set of states whose dynamics approach that of a classical harmonic oscillator are called coherent states. Such states are denoted by $|\alpha\rangle$ and satisfy $a\,|\alpha\rangle = \alpha\,|\alpha\rangle$, where the eigenvalue α is a complex number[98]. This number relates to the average occupation of a coherent state by $\langle n\rangle = \langle a^\dagger a\rangle = |\alpha|^2$. In terms of the measured scatter in the quadrature amplitudes X and Y, a coherent state yields a variance of $\mathrm{Var}(X) = \langle X^2\rangle - \langle X\rangle^2 = 1/4$ quanta and $\mathrm{Var}(Y) = 1/4$ quanta, where 'quanta' refers to a single excitation of the harmonic oscillator.

In contrast to a coherent state, the state $|n\rangle$ has no analogous representation in the formalism of the classical harmonic oscillator[98]. This 'number state' has n quanta, each with energy $\hbar\omega$. Although a number state has a well-defined number of quanta, its phase (the conjugate variable) is maximally uncertain. Regardless of n, a number state yields quadrature amplitudes X and Y that have a mean of zero. However, their total variance of $\mathrm{Var}(X) = \mathrm{Var}(Y) = (2n+1)/4$ quanta is non-zero for any integer $n \geq 0$.

To represent a statistical mixture of pure number states, one employs the density matrix ρ. For a single pure number state, the corresponding density matrix is $\rho = |n\rangle\langle n|$. However, if an ensemble of number states is prepared each with a statistical probability $P(n)$, the density matrix becomes

$$\rho = \sum_n P(n)\,|n\rangle\langle n| \tag{2.13}$$

where n labels each number state in the ensemble[98]. To calculate the expectation value of an observable, such as a quadrature operator X, one takes $\langle X\rangle = \mathrm{tr}(\rho X)$ where $\mathrm{tr}(\cdots)$ denotes a trace operation.

The density matrix provides a convenient description of an ensemble of number states held at a non-zero temperature T. The density matrix ρ_{th} that describes such a system has probabilities that follow a Boltzmann distribution. As such, they are given by

$$P(n) = \frac{\langle n\rangle^n}{(\langle n\rangle + 1)^{n+1}} \tag{2.14}$$

where $\langle n\rangle = (\exp(\hbar\omega/k_{\mathrm{B}}T) - 1)^{-1}$ is the average occupation[98]. When measured in the quadrature

basis, a thermal state yields quadrature amplitudes X and Y that have a mean of zero. However, the quadrature variance is the same as that of a pure number state with $\mathrm{Var}(X) = \mathrm{tr}(\rho X^2) = (2\langle n\rangle + 1)/4$ quanta and similarly for the Y amplitude.

2.1.4 Decoherence

Any harmonic oscillator in the laboratory will inevitably experience dissipation. For example, such dissipation could be a result of a frictional force $-c\dot{x}(t)$ which causes the oscillator to loose energy where c is a constant coefficient. Because of the fluctuation-dissipation theorem[103], this damping is also a source of a fluctuating force $F_0(t)$ that drives the oscillator. To include these two effects in the description of the classical harmonic oscillator, one can write Eqns. 2.1 as

$$\dot{p}(t) = -kx - c\dot{x}(t) + F_0(t) \tag{2.15}$$

where F_0 is the fluctuating variable that obeys a Gaussian distribution with mean zero and has a correlation function given by $\langle F_0(t)F_0(t')\rangle = 2ck_{\mathrm{B}}T_{\mathrm{env}}\delta(t-t')$ where T_{env} is the temperature of the oscillator's environment and $\langle\cdots\rangle$ represents an ensemble average[104]. This noise term ensures that the oscillator comes into thermal equilibrium with its environment. Eqn. 2.15 is a specific case of the Langevin equation, which was originally developed to describe the Brownian motion of a particle immersed in a fluid[105].

To introduce dissipation in a quantum harmonic oscillator, one can write Eqns. 2.10 in the form of the Langevin equation. In the presence of dampening κ and a fluctuating field $a_0(t)$, the field operators evolve according to

$$\dot{a}(t) = -i\omega a(t) - \frac{\kappa}{2}a(t) + \sqrt{\kappa}a_0(t) \tag{2.16}$$

where $\langle a_0^\dagger(t)a_0(t')\rangle = N\delta(t-t')$ is the correlation function for the fluctuating field $a_0(t)$ and $N = (\exp(\hbar\omega/k_{\mathrm{B}}T_{\mathrm{env}}) - 1)^{-1}$ is the occupation of the environment. Here, $\langle a_0^\dagger(t)a_0(t')\rangle$ is normalized to have units of photons/sec. Eqn. 2.16 and the Hermitian conjugate equation for $a^\dagger(t)$ constitute the Heisenberg-Langevin equations of motion for a quantum harmonic oscillator[106].

These equations provide a full description of how $a(t)$ and $a^\dagger(t)$ evolve for the oscillator as its energy decays because of dissipation.

In terms of the density matrix ρ, the quantum master equation provides a full description of the dissipative quantum harmonic oscillator. This approach takes the quantum harmonic oscillator as the system of interest and couples it to an external environment. The evolution of $\rho_{\text{tot}}(t)$ for this total system is governed by the von Neumann equation, an equivalent form of the Schrödinger equation, given by

$$\dot{\rho}_{\text{tot}}(t) = -\frac{i}{\hbar}[H_{\text{tot}}, \rho_{\text{tot}}(t)] \tag{2.17}$$

where the total Hamiltonian H_{tot} includes the system, its environment, and their mutual interactions. To calculate the state of the dissipative quantum harmonic oscillator, one performs a partial trace over the environment $\rho = \text{tr}_{\text{env}}(\rho_{\text{tot}})$. By modeling the environment as a collection of harmonic oscillators, one can derive a master equation for the system of interest. Numerous derivations exist[107, 108, 109], and so I simply state the result given by

$$\frac{d\rho}{dt} = -\frac{i}{\hbar}[H_{\text{sys}}, \rho] - \frac{(N+1)}{2}\kappa\left(a^\dagger a\rho + \rho a^\dagger a - 2a\rho a^\dagger\right) - \frac{N}{2}\kappa\left(aa^\dagger\rho + \rho aa^\dagger - 2a^\dagger\rho a\right) \tag{2.18}$$

where N is the average occupation of the environment, and κ is the rate of energy exchange between the environment and the oscillator. The first term on the right hand side describes the evolution of the system of interest described by H_{sys}, and the remaining two terms account for energy decay and random thermal jumps in the oscillator's energy states.

2.2 Qubits as discrete-variable systems

A discrete-variable system encodes quantum information in states that form a discrete and finite set. The prototypical discrete-variable system is a quantum bit (qubit), which is a fundamental unit of quantum information[70]. For this thesis, I utilize a qubit to generate quantum superpositions of harmonic oscillator states that encode the qubit's state.

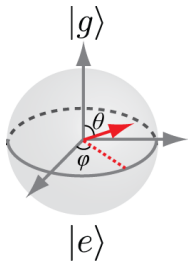

Figure 2.2: Diagram of a Bloch sphere. The red arrow denotes a pure qubit state $|\psi\rangle$ parameterized by φ and θ. The qubit's ground and excited states are denoted by $|g\rangle$ and $|e\rangle$. For a pure state, the arrow has unit length.

2.2.1 Representation on the Bloch sphere

A single qubit is a two-state system, typically taken to be the ground $|g\rangle$ and excited $|e\rangle$ states of an atom. Because of quantum mechanics, these states can exist in a superposition state $|\psi\rangle = a\,|g\rangle + b\,|e\rangle$ where a and b are complex amplitudes such that $|a|^2$ and $|b|^2$ yield the probability of occupying the $|g\rangle$ and $|e\rangle$ states, respectively. Because the square of these amplitudes correspond to probabilities, they must satisfy $|a|^2 + |b|^2 = 1$. This normalization condition removes one degree of freedom, and so the qubit's state vector can be represented as

$$|\psi\rangle = \cos(\theta/2)\,|g\rangle + e^{i\varphi}\sin(\theta/2)\,|e\rangle \tag{2.19}$$

where θ and φ parametrize the state's relative populations and their phase, respectively. Importantly, these parameters can be conveniently mapped onto spherical coordinates for a 'Bloch sphere' as diagrammed in Fig. 2.2.

2.2.2 Rotations on the Bloch sphere

Alterations to the qubit's state correspond to rotations on the Bloch sphere. For example, if the qubit state is $|\psi\rangle = |g\rangle$, it can be rotated by $\theta = \pi$ using $\sigma_x\,|\psi\rangle = |e\rangle$ where σ_x is a Pauli matrix. In general, an arbitrary rotation is represented by a 2×2 unitary matrix U. Any such matrix can be written as $\exp(i\theta H/\hbar)$ where H is a Hermitian matrix that is a linear combination of the Pauli matrices. This operator corresponds to a rotation on the Bloch sphere. For example,

to rotate the qubit state about the x axis by an angle of θ, one would use $\exp(-i\theta\sigma_x/2)$.

2.3 A qubit coupled to a harmonic oscillator

To deterministically generate arbitrary quantum states of a harmonic oscillator, it must couple to a discrete-variable system. The archetypal qubit and harmonic oscillator system is an atom with two energy levels coupled to a single mode of an electromagnetic resonator. Here, I refer to a 'qubit' as one bit of quantum information, and I call the 'atom' the physical object that initially encodes the qubit. For the harmonic oscillator, the resonator is typically taken to be an optical cavity, and its lower-frequency counterpart is a microwave cavity or circuit. When the atom is excited, it can decay in such a way as to create a single excitation of the cavity mode–that is, a single photon. By preparing the atom in an arbitrary superposition state, this qubit can be transferred to the cavity mode manifest as a superposition of zero and one photons.

2.3.1 Jaynes-Cummings model

The Jaynes-Cummings model describes the interaction between an atom and a single quantized mode of a cavity[98, 109]. This fundamental interaction has been realized using real atoms[110], quantum dots[111, 112], and superconducting circuits[113, 114]. Regardless of the physical system, the Hamiltonian for the atom is that of a qubit: $H_{\mathrm{q}} = \hbar\omega_{\mathrm{q}}\sigma_z/2$ where ω_{q} is its ground to excited state transition frequency. In contrast to the qubit, the cavity mode oscillates at ω_{c} and is a quantized harmonic oscillator with the Hamiltonian $H_{\mathrm{ho}} = \hbar\omega_{\mathrm{c}}(a^\dagger a + 1/2)$ as described in Section 2.1.2.

By coupling the atom's dipole operator $\hat{d}$ to the electric field operator $\hat{E}$ of the cavity, these two systems can interact with each other. Here, I take the dipole moment to be the matrix element $d = \langle e|\hat{d}|g\rangle$, and I assume d is real so that $\hat{d} = \sigma_x d$. Because $E \propto (a^\dagger + a)$, the resulting dipole interaction $-\hat{d}\cdot\hat{E}$ is described by the Hamiltonian $H_{\mathrm{int}} = \hbar g\sigma_x(a^\dagger + a)$ where g is the coupling rate between the two systems.

To obtain the Jaynes-Cummings model from H_{int}, the system must satisfy $|\omega_{\mathrm{c}} - \omega_{\mathrm{q}}| \ll \omega_{\mathrm{c}} + \omega_{\mathrm{q}}$.

In this regime, the rotating wave approximation is valid and so one can neglect rapidly oscillating terms at $\omega_{\mathrm{q}} + \omega_{\mathrm{c}}$. Using this approximation and $\sigma_x = \sigma_- + \sigma_+$, one obtains the Jaynes-Cummings Hamiltonian

$$H_{\mathrm{JC}} = \hbar\omega_{\mathrm{c}} a^\dagger a + \hbar\omega_{\mathrm{q}} \frac{\sigma_z}{2} + \frac{\hbar g}{2}(a\sigma_+ + a^\dagger \sigma_-) \tag{2.20}$$

where σ_+ (σ_-) excites (de-excites) the atom and I shifted the energy reference by removing the term $\hbar\omega_{\mathrm{c}}/2$. If the atom and cavity are detuned by $|\omega_{\mathrm{q}} - \omega_{\mathrm{c}}| \ll g$, they are resonant with each other and thus can directly exchange energy. The system can also be engineered to enter the dispersive regime in which the atom and cavity are not resonant with each other.

2.3.2 Dispersive regime

To extract information from the qubit while minimally altering its state, the qubit-cavity system must enter the dispersive regime. In this regime the qubit's transition frequency and cavity frequency are far-detuned from each other with a detuning of $\Delta = \omega_{\mathrm{q}} - \omega_{\mathrm{c}}$ and their coupling rate satisfies $g \ll |\Delta|$. By expanding the Jaynes-Cummings Hamiltonian to second order in g/Δ, one obtains the dispersive Hamiltonian[115]

$$H_{\mathrm{d}}/\hbar = \omega_{\mathrm{c}} a^\dagger a + \omega_{\mathrm{q}} \frac{\sigma_z}{2} + 2\chi \frac{\sigma_z}{2} a^\dagger a \tag{2.21}$$

where $\chi = g^2/\Delta$ is the dispersive shift. The energy spectrum of the dispersive Hamiltonian is depicted in Fig. 2.3 assuming $\Delta < 0$ as is the case for the cQED system discussed in Chapter 4.

The dispersive Hamiltonian reveals how the presence or absence of a single photon in the cavity substantially alters the qubit's transition frequency and reciprocally, how the qubit's state affects the cavity frequency[116]. By collecting terms with factors of $\sigma_z/2$, one finds that the qubit's frequency $\omega_{\mathrm{q}} \to \omega_{\mathrm{q}} + 2\chi n$ where n is the number of photons in the cavity. As such, the qubit's transition frequency is a function of how many photons are in the cavity. Furthermore, by collecting terms with factors of $a^\dagger a$, one finds that the cavity frequency depends on the qubit state according to $\omega_{\mathrm{c}} \to \omega_{\mathrm{c}} + \chi\langle\sigma_z\rangle$ where $\langle\sigma_z\rangle = \pm 1$ depending on the qubit's state. As such, one can determine the qubit state by measuring the response of the cavity.

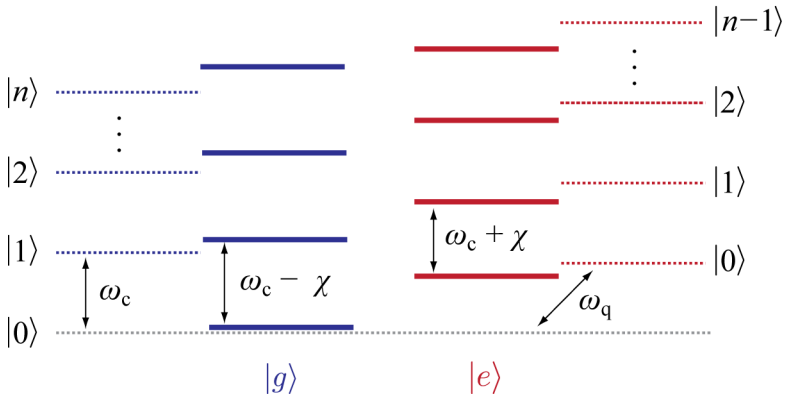

Figure 2.3: Energy level diagram of the coupled qubit-cavity system. The dashed lines correspond to the eigenstates of the uncoupled Hamiltonian, where the cavity photon states are denoted by $|n\rangle$ and the qubit levels are denoted by $|g\rangle$ and $|e\rangle$. When the qubit and cavity are coupled in the dispersive regime such that $|\omega_q - \omega_c| \gg g$, the energy levels shift as indicated by the solid lines.

2.3.3 Rabi oscillations

In the presence of a drive field, the qubit's state $|\psi(t)\rangle$ can undergo 'Rabi oscillations' between its two levels. The time evolution of $|\psi(t)\rangle$ is given by the unitary operator $U(t) = e^{-iHt/\hbar}$ where H is the system's Hamiltonian. If the center frequency of the drive is near the qubit's transition, the system's interaction Hamiltonian is $H_{\text{int}} = \frac{1}{2}\hbar\Omega\vec{n}\cdot\vec{\sigma}$ where $\vec{n}$ is a unit vector that specifies the rotation axis on the Bloch sphere, $\vec{\sigma}$ is a vector of the Pauli matrices, and Ω is the coupling rate between the drive field and the qubit.

To understand how the drive affects the qubit state, consider the simple case in which $\vec{n} = \hat{x}$. The corresponding unitary operator is $U(t) = \cos(\Omega t/2)I_2 - i\sin(\Omega t/2)\sigma_x$ where I_2 is the 2×2 identity matrix.[1] Suppose the qubit is initially prepared in its $|g\rangle$ state. After the drive is on for a time $t = T$, the probability of the qubit occupying the excited state is

$$P_e(T) = |\langle e|U(T)|g\rangle|^2 = \sin^2(\Omega T/2). \tag{2.22}$$

Because the qubit's population oscillates between its ground and excited states, the qubit can be prepared in any superposition state $|\psi(t)\rangle = a(t)|g\rangle + b(t)|e\rangle$ using a pulsed drive field with an

[1] To derive this expression for a 2×2 matrix A that satisfies $A^2 = I_2$, use the identity $\exp(i\theta A) = \cos(\theta)I_2 + i\sin(\theta)A$ where θ is a real angle[102].

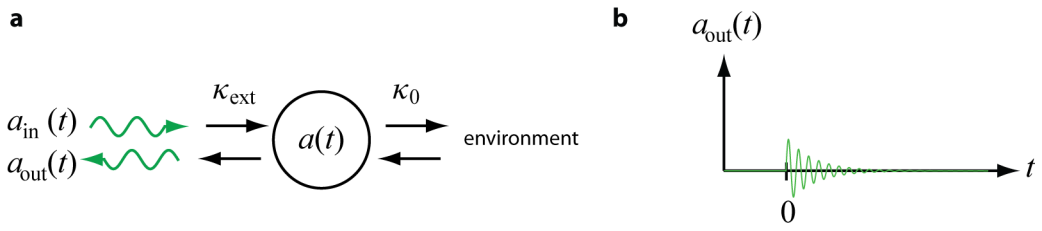

Figure 2.4: Evolution of a stationary mode into a propagating mode. **a,** The diagram depicts a single stationary mode $a(t)$ coupled to the modes $a_{\text{in}}(t)$ and $a_{\text{out}}(t)$ that propagate in a transmission line. The stationary mode oscillates at ω_0 and couples to the propagating mode at a rate of κ_{ext}. Additionally, the stationary mode couples to the environment at a rate of κ_0. At time $t = 0$, the amplitude of the stationary mode is $a(0)$. **b,** The plot depicts $a_{\text{out}}(t)$ emitted from the stationary mode. This field can be measured using either homodyne or heterodyne detection (see Section 2.5).

appropriate duration T and coupling rate Ω. For instance, the choice of $T = \pi/\Omega$ drives the qubit into its excited state. Such a drive is called a 'π-pulse' because the qubit's state rotates by $\theta = \pi$.

2.3.4 Blue sideband transition

The blue sideband transition provides a mechanism for creating an interaction between the qubit and the cavity[117, 118]. Although these two systems do not directly exchange energy in the dispersive regime, driving the blue sideband transition at $\omega_{\text{b}} = \omega_{\text{c}} + \omega_{\text{q}}$ creates a simultaneous excitation of both the qubit and the cavity. For the transmon-style qubit used in this thesis (see Chapter 4), the blue sideband transition occurs only as a two-photon process[115, 117]. The simplest method of accessing this transition is to drive it using a strong, detuned tone at $\omega_{\text{b}}/2$. When driven in this manner, the qubit-cavity system oscillates between the joint states $|g\rangle\,|0\rangle$ and $|e\rangle\,|1\rangle$. As such, the blue sideband transition enables the creation of a single cavity photon[119]. By coupling the cavity to a transmission line, the photon will decay into a propagating mode.

2.4 Stationary and propagating modes

A quantum state stored in an electromagnetic resonator is confined to a stationary mode. This mode is essentially a standing wave because it does not, on average, propagate energy in any net direction. To communicate information contained in the quantum state to a physically-

separate system of interest, one must release the energy stored in the stationary mode. This release can be achieved by coupling the electromagnetic resonator to a transmission line as depicted in Fig. 2.4. If this coupling is constant, the stationary mode will evolve into a propagating mode in the transmission line at a rate set by the bandwidth of the resonator.

2.4.1 Input-output theory for a one-port resonator

To mathematically describe a single stationary mode of an electromagnetic resonator, I model it as a harmonic oscillator with dissipation. As such, the evolution of the complex field amplitude $a(t)$ for this mode is governed by Eqn. 2.16. In a frame rotating at the center frequency of the resonator ω_0, the equation for $a(t)$ becomes

$$\dot{a}(t) = -\frac{\kappa}{2}a(t) + \sqrt{\kappa_{\text{ext}}}a_{\text{in}}(t) \tag{2.23}$$

where $\kappa = \kappa_{\text{ext}} + \kappa_0$ is the total energy decay rate of the resonator, which includes the external coupling rate κ_{ext} to the transmission line and the unwanted 'internal' decay rate κ_0 of energy to an unmeasured port. The external coupling is set by the resonator design, whereas the internal loss rate is determined by its fabrication details[120]. Here, I assume $a_{\text{in}}(t)$ is in the vacuum state, and so $\langle a_{\text{in}}^\dagger(t)a_{\text{in}}(t')\rangle = 0$ and $\langle a_{\text{in}}(t)\rangle = 0$ as discussed in Section 2.1.4.

2.4.2 Resonator state evolves into a propagating mode

Upon energizing the resonator, its field evolves into a mode that propagates in the transmission line. The amplitude of this propagating field is described by the input-output relation $a_{\text{out}}(t) = \sqrt{\kappa_{\text{ext}}}a(t) - a_{\text{in}}(t)$ where $a(t)$ is defined in Eqn. 2.23. To simplify its solution, I assume $\kappa_0 \ll \kappa_{\text{ext}}$ and so

$$a_{\text{out}}(t) = \sqrt{\kappa}a(0)h(t) + \kappa \cdot (h \star a_{\text{in}})(t) - a_{\text{in}}(t) \tag{2.24}$$

where $h(t) = \exp(-\kappa t/2)$, the $\star$ denotes the convolution operation,[2] and $a(0)$ is the initial field amplitude in the resonator.

[2] Its definition is $(h \star a_{\text{in}})(t) = \int_0^t h(t-\tau)a_{\text{in}}(\tau)\,\mathrm{d}\tau$.

To extract $a(0)$ from the continuum of modes in the transmission line, one must define a particular temporal envelope for the mode of interest[121]. Ideally, for a decaying field emitted from the resonator, this envelope is given by $f(t) = \sqrt{\kappa}e^{-\kappa t/2}\Theta(t)$ where $\Theta(t)$ is the Heaviside function. By weighting $a_{\text{out}}(t)$ with $f(t)$, one obtains the time-independent output mode

$$A = \int f(t)a_{\text{out}}(t)\,\mathrm{d}t = a(0) \tag{2.25}$$

which does not contain the noise term $a_{\text{out}}(t)$. Because $A = a(0)$, tomography on mode A reveals the quantum state of the cavity mode at $t = 0$.

2.5 Quantum state tomography of a propagating mode

To characterize the state of a propagating mode, I employ quantum state tomography[122]. The goal of quantum state tomography is to determine the density matrix ρ that completely specifies the quantum state of interest. For a propagating mode, one does not directly measure ρ in an experiment. Instead, it can be reconstructed from a set of quadrature amplitudes X and Y measured using either homodyne or heterodyne detection[123]. The set is constructed by performing repeated measurements on an ensemble of identically prepared states. From this set, one extracts ρ by using the statistical method of maximum likelihood.

2.5.1 Homodyne detection

Homodyne detection yields a single quadrature measurement of a field. In the optical domain, a beamsplitter combines the field to be measured and a field called the local oscillator that provides an adjustable phase reference. Specifically, this phase reference defines an angle ϕ between the local oscillator and the field to be measured. At the beamsplitter's two output ports, a pair of photodetectors produce a signal that is proportional to the field's quadrature amplitude X. In the microwave domain[121, 124], one utilizes a phase-sensitive linear amplifier to measure the quadrature amplitude of a given field. Because phase-sensitive amplification can ideally add zero noise during the amplification process, it enables efficient single-quadrature measurements of a

microwave field[125].

By making repeated single-quadrature measurements of identically-prepared quantum states described by ρ, one samples from its marginal distribution. For a given local oscillator phase, this probability density function is given by

$$\Pr(X|\phi) = \langle X| U^{\dagger}(\phi)\rho U(\phi) |X\rangle \tag{2.26}$$

where $U(\phi) = \exp\left(-i\phi a^{\dagger}a\right)$ accounts for the aforementioned phase reference[123]. To obtain a complete reconstruction of ρ, one must rotate θ throughout the entire phase space of the quantum state. This technique is analogous to medical imagining in which a doctor reconstructs a three-dimensional picture of a person's tissue using a collection of two-dimensional images acquired from a known set of angles.

2.5.2 Heterodyne detection

In contrast to homodyne detection, heterodyne detection yields a set of simultaneous quadrature measurements. These joint measurements provide enough information for complete quantum state reconstruction. In the optical domain, heterodyne detection is performed by splitting a state of interest on a beamsplitter and measuring a single orthogonal quadrature of each output mode relative to a common local oscillator[123]. The microwave equivalent of this technique is phase-insensitive linear amplification[124]. This approach amplifies a signal's quadratures amplitudes regardless of its phase relative to the local oscillator.

For quantum-limited heterodyne detection, performing simultaneous measurements of both quadratures adds at least half a quantum of noise[126]. This noise is accounted for in the probability density for obtaining a pair of quadrature values X and Y, given by the Husimi Q-function[127]

$$Q(\alpha) = \frac{1}{\pi} \langle \alpha| \rho |\alpha\rangle \tag{2.27}$$

where $\alpha = X + iY$ and $Q(\alpha)$ is normalized to unity such that $0 \leq Q(\alpha) \leq \pi^{-1}$ for all complex values of α. If ρ is in the vacuum state, the Q-function is Gaussian distribution given by

$$Q(\alpha) = \frac{1}{\pi} e^{-|\alpha|^2}. \tag{2.28}$$

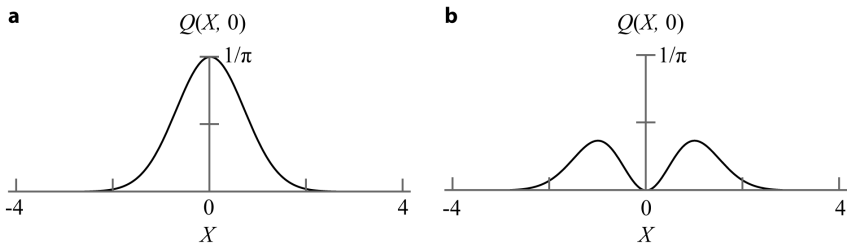

Figure 2.5: Plots of Q-functions for ideal vacuum and single-photon states. To clearly represent the distributions, the plots show a linecuts through the Q-functions for $Y = 0$ assuming ρ is in the **a,** vacuum state and **b,** single-photon state. The vacuum state follows a Gaussian distribution, whereas the single-photon state does not.

A plot of a linecut through this function is presented in Fig. 2.5a. In contrast, if ρ is a single-photon state, the distribution is given by

$$Q(\alpha) = \frac{1}{\pi} e^{-|\alpha|^2} |\alpha|^2. \tag{2.29}$$

The above distribution is not Gaussian as shown in Fig. 2.5b, and so one refers to ρ in this case as a 'non-Gaussian' state.

2.5.3 Method of maximum likelihood

The method of maximum likelihood converts a set of measured quadrature amplitudes into a density matrix ρ. This technique is a general statistical method used to estimate the parameters of an assumed model, given a set of observed data. For quantum state tomography, the parameters to be estimated are the elements of ρ and the statistical model is the assumed probability distribution that the measured quadrature amplitudes are expected to obey.

The goal of maximum likelihood tomography is to find the density matrix which maximizes the likelihood function for a given set of measurements. In general, given a set of N measurement outcomes $\{x_k\}$, each outcome is described mathematically by a positive-operator valued measure (POVM) element E_k [128]. If the system is in the state given by density matrix ρ, the probability of observing measurement outcome x_k is $\Pr(x_k) = \mathrm{tr}(\rho E_k)$. The probability of obtaining the entire data set is then the product of the probabilities of each measurement outcome. This product defines

the likelihood function

$$L = \prod_k \mathrm{tr}(\rho E_k). \tag{2.30}$$

Maximizing L may not be computationally efficient because ρ can be a large matrix. Instead, an equivalent approach is to maximize the log-Likelihood function given by

$$\mathcal{L} = \sum_k \log(\mathrm{tr}(\rho E_k)) \tag{2.31}$$

where the logarithm converts the product into a sum.

A robust method for maximizing the log-likelihood function is the RρR algorithm[129]. The algorithm begins with the maximally mixed state $\rho^{(0)} = \mathbb{I}/d$ as the initial estimate, where $\mathbb{I}$ is the identity matrix and d is the Hilbert space dimension. With each iteration, ρ is then updated according to

$$\rho^{(i+1)} = \mathcal{N}\,\mathrm{R}(\rho^{(i)})\rho^{(i)}\mathrm{R}(\rho^{(i)}), \tag{2.32}$$

where $\mathcal{N}$ is an overall normalization to ensure that $\mathrm{tr}(\rho) = 1$ at each step, and $\mathrm{R}(\rho)$ is a matrix given by[3]

$$\mathrm{R}(\rho) = \frac{1}{N}\sum_k \frac{E_k}{\mathrm{tr}(\rho E_k)}. \tag{2.33}$$

The RρR transformation leaves the maximum-likely state unchanged, and while the algorithm is not guaranteed to converge[130], it does so in almost all practical cases, including the cases considered in this thesis.

The choice of E_k in Eqn. 2.33 depends the level of added noise in the detection method. If the detection employs the heterodyne method and is quantum-limited, the probability density for obtaining a pair of quadrature values (X_k, Y_k) is given by the Husimi Q-function[127]:

$$\Pr(X_k, Y_k) = Q(X_k, Y_k) = \frac{1}{\pi}\langle\alpha_k|\,\rho\,|\alpha_k\rangle = \frac{1}{\pi}\mathrm{tr}(\rho\,|\alpha_k\rangle\langle\alpha_k|) \tag{2.34}$$

Here $|\alpha_k\rangle$ is a coherent state with $\alpha_k = X_k + iY_k$. From the above equation, note that the POVM elements for the measurement outcomes are projections onto coherent states:

$$E_k = \frac{1}{\pi}\,|\alpha_k\rangle\langle\alpha_k|\,. \tag{2.35}$$

[3] A heuristic way to understand the R matrix is that it is a derivative of $\log\mathcal{L}$ with respect to ρ.

However, if the added noise in the detection method is not quantum-limited, the POVM elements are no longer projections onto coherent states. For this case, the POVM operators are projections onto displaced thermal states:

$$E_k = \frac{1}{\pi} D(\alpha_k)\rho_{\text{th}} D^\dagger(\alpha_k). \tag{2.36}$$

where $D(\alpha) = \exp\left(\alpha a^\dagger - \alpha^* a\right)$ is the displacement operator and ρ_{th} is a thermal state with thermal occupancy n_{th}. To derive Eqn. 2.36, note that because the added noise of the amplifier is not quantum limited, the probability density for obtaining quadrature values $\{(X_k, Y_k)\}$ is no longer the Q-function of the input microwave mode but rather the convolution of the Q-function with the added thermal noise:

$$\begin{aligned}
\Pr(X,Y) &= \int d\alpha' Q(\alpha') e^{-|\alpha-\alpha'|^2/2n_{\text{th}}} \\
&= \int d\alpha' \frac{1}{\pi} \text{tr}(\rho \left|\alpha'\right\rangle \left\langle\alpha'\right|) e^{-|\alpha-\alpha'|^2/2n_{\text{th}}} \\
&= \frac{1}{\pi} \text{tr} \int d\alpha' \rho \left|\alpha+\alpha'\right\rangle \left\langle\alpha+\alpha'\right| e^{-|\alpha'|^2/2n_{\text{th}}} \\
&= \frac{1}{\pi} \text{tr} \rho D(\alpha) \left(\int d\alpha' \left|\alpha'\right\rangle \left\langle\alpha'\right| e^{-|\alpha'|^2/2n_{\text{th}}} \right) D^\dagger(\alpha)
\end{aligned} \tag{2.37}$$

The third equality is from the change of variables $\alpha' \to \alpha + \alpha'$, and the integral in the fourth line of Eqn. 2.37 is equivalent to a thermal state ρ_{th} with mean excitation number n_{th}. To see how a thermal state emerges in this calculation, note that the P-representation for a thermal state is[123]

$$\rho_{\text{th}} = \int \text{d}^2\alpha \left|\alpha\right\rangle \left\langle\alpha\right| P(\alpha) \tag{2.38}$$

where $P(\alpha) = e^{-|\alpha'|^2/2n_{\text{th}}}$ is taken from the fourth line of Eqn. 2.37. Thus, we find

$$P(\alpha_k) = \frac{1}{\pi} \text{tr}(\rho E_k) \tag{2.39}$$

where E_k is POVM element for a coherent state.

Chapter 3

Theory and characterization of the electromechanical device

An electromechanical device converts information between the motion of a mechanical resonator and a microwave field. This device can be exploited in two ways. First, it can capture the state of a microwave field propagating in a transmission line. Once captured, the state is mechanically-stored and later released. This 'capture and store' capability enables the electromechanical device to be utilized as an on-demand memory for microwave qubits[64]. Second, the electromechanical device can amplify a feeble signal with quantum-limited noise performance. While similar types of amplifiers are aggressively being developed for measuring superconducting circuits[131, 132], the electromechanical device provides the benefit of directly amplifying a signal that is contained in either a microwave field or the mechanical resonator. This benefit enables a microwave or mechanical quantum state to be efficiently characterized as shown in Chapter 5.

In this chapter, I introduce a theoretical understanding of the electromechanical device and its initial experimental characterization. Section 3.1 establishes a mathematical framework that describes how the device converts information between the microwave and mechanical domains. As part of this section, I show how a tunable capacitor enables the electromechanical device to enhance its operation bandwidth. In Section 3.2, I characterize the parameters of the electromechanical device that are discussed in the theory section.

3.1 Theory of the electromechanical device

To combine electricity with mechanical motion, the electromechanical device utilizes an inductor-capacitor (LC) circuit with a variable capacitor. Charge q sloshes back and forth between the inductor and capacitor, oscillating at about seven billion times a second (a microwave frequency). One plate of the capacitor is free to move, and so any displacement x alters the position-dependent capacitance. Because part of the capacitor is flexible, its motion is affected by the electrostatic force

$$F_{\text{es}} \propto q^2. \tag{3.1}$$

From this inherent nonlinearity emerges the ability to damp or amplify the motion of the flexible capacitor plate, or to control its spring constant.

In this section, I mathematically describe these phenomena. Although the classical dynamics of the electromechanical device can be calculated by taking the charge on the capacitor plate q and the plate displacement x as dynamical variables[133], its quantum dynamics are more naturally modeled using the well-described framework of input-output theory[134, 109, 108]. First, I introduce the Heisenberg-Langevin equations of motion that model linear electromechanics. Next, I show how the inherent time-dependence in these equations enables the electromechanical device to capture, store, and amplify a signal. Lastly, I show how the capacitor plate can be electrostatically actuated in order to make the center frequency of the electromechanical device tunable.

3.1.1 Heisenberg-Langevin equations of motion

As pointed out in Section 2.1.4, the Heisenberg-Langevin equations of motion provide a framework to describe a harmonic oscillator with dissipation. Because both the mechanical resonator and LC circuit can be modeled as dissipative harmonic oscillators, the Heisenberg-Langevin equations can describe the dynamics of the electromechanical device. In this section, I start by modeling the classical dynamics of the electromechanical device. Specifically, I formulate a set of Heisenberg-Langevin equations that describe the position of the mechanical resonator and how it couples to

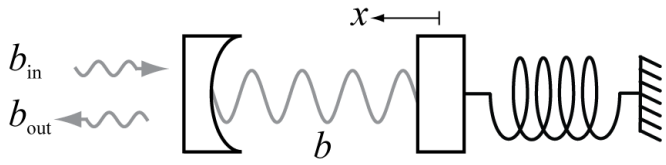

Figure 3.1: Diagram of a cavity optomechanical system. Two mirrors form an optical cavity, one of which is harmonically bound. An input field b_{in} probes the cavity, and a circulating field b builds up in the cavity. The reflected outgoing field b_{out} contains information about the state of the system.

the complex field amplitude of the circuit mode.[1] I conclude by replacing the amplitudes with operators in order to describe the quantum dynamics of the electromechanical device.

Formally, the electromechanical device is equivalent to an optical cavity with one of its mirrors harmonically bound as diagrammed in Fig. 3.1. The cavity is analogous to the LC circuit, and the mechanically-compliant mirror is analogous to the flexible capacitor plate. Because the circuit is addressed by a transmission line, the cavity also is addressed by a propagating mode. This model of a 'cavity optomechanical' system provides a description of how the mirror's motion and dynamics of the cavity field affect each other.

Motion of the mirror alters the resonant frequency of the cavity. When the mirror moves by a displacement x, the resonant frequency of the cavity shifts by Gx where $G = \partial\omega_0/\partial x$ denotes the shift in the cavity resonant frequency per change in displacement of the mirror. This shift of the resonant frequency is due to the parametric coupling between the mirror's motion and the cavity mode. For the cavity depicted in Fig. 3.1, $G \approx \omega_0/L$ where L is the separation between the two mirrors and ω_0 is the cavity's resonant frequency[27]. However, for an electromechanical circuit, $G \approx \omega_0/2d$ where d is the static separation between the capacitor plates[136].

To model the dynamics of the cavity field $b(t)$, I incorporate the parametric coupling mechanism into the equations of motion for a one-port cavity. Although one of the cavity mirrors is mechanically-compliant, the other mirror is partially transmissive so that energy in the cavity

[1] This complex field amplitude is a properly normalized variable for the electric field in the circuit mode as discussed in Ref. [135].

decays out at a rate of κ_{ext}. The corresponding equation for the cavity is

$$\dot{b}(t) = \left(-i\left(\omega_0 + Gx(t)\right) - \frac{\kappa}{2}\right) b(t) + \sqrt{\kappa_{\text{ext}}} b_{\text{in}}(t) \tag{3.2}$$

where κ is the total linewidth of the cavity and b_{in} is the amplitude of an input drive field.

Because the cavity field exerts a force on the mirrors, the displacement $x(t)$ of the mechanically-compliant mirror depends on $b(t)$. The force per photon is $\hbar G$, and for $|b(t)|^2$ photons in the cavity the total force is $F = -\hbar G|b(t)|^2$. By including F, along with the restoring force of the spring and mechanical dissipation, the equation of motion for the position becomes

$$\ddot{x}(t) = -\kappa_{\text{m}}\dot{x}(t) - \omega_{\text{m}}^2 x(t) - \hbar G|b(t)|^2/m_{\text{eff}} + \eta_{\text{m}}(t)/m_{\text{eff}} \tag{3.3}$$

where m_{eff} is the effective mass of the mechanical resonator[27], ω_{m} its resonant frequency, and $\eta_{\text{m}}(t)$ is a fluctuating force that drives mechanical resonator, as discussed in Section 2.1.4. The motion of the mechanical resonator is damped because of the dissipative force term with $\dot{x}(t)$ where κ_{m} is the mechanical resonator's intrinsic damping rate.

The equations of motion for a cavity optomechanical system are weakly nonlinear in the field amplitude. The scale of the nonlinear interaction is set by G and the zero-point fluctuations of the mechanical resonator $x_{\text{zp}} = \sqrt{\hbar/(2m_{\text{eff}}\omega_{\text{m}})}$. In most experiments to date [27], the cavity decay rate is overwhelming with $\kappa \gg Gx_{\text{zp}}$ and so the inherent parametric coupling is quite feeble. However, by pumping the cavity with a strong field, one can boost the coupling rate Gx_{zp} by many orders of magnitude.

In order pump the cavity, it is driven by an input field of the form $b_{\text{in}}(t) = \bar{b}_{\text{in}} e^{-i\omega_{\text{p}}t}$. This field induces an average of $|\bar{b}|^2$ circulating cavity photons, which impart a static displacement $\bar{x}$ on the mechanical resonator. The equilibrium field $\bar{b}$ and static displacement $\bar{x}$ are calculated by solving Eqns. 3.2 and 3.3 with $\dot{b}(t) = \ddot{x}(t) = \dot{x}(t) = 0$, which yield solutions[2]

$$\bar{b} = \frac{\sqrt{\kappa_{\text{ext}}}}{-i\Delta + \kappa/2}\bar{b}_{\text{in}} \quad \text{and} \quad \bar{x} = -\frac{\hbar G}{m_{\text{eff}}\omega_{\text{m}}^2}|\bar{b}|^2 \tag{3.4}$$

[2] The relation for $\bar{x}$ can also be derived by using Hooke's Law $\bar{x} = -k^{-1}F_p N_{\text{c}}$ where $k = \omega_{\text{m}}^2 m_{\text{eff}}$ is the spring constant, $F_p = \hbar G$ is the force per photon, and $N_{\text{c}} = |\bar{b}|^2$ is the number of photons in the cavity.

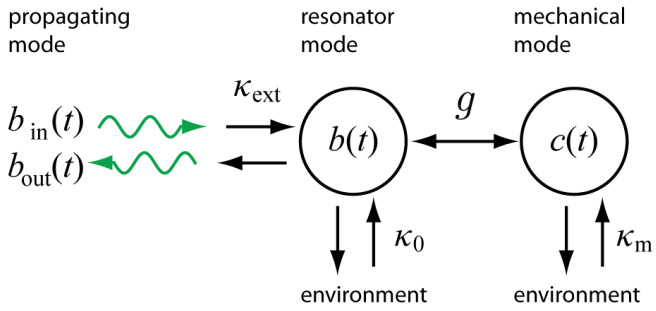

Figure 3.2: Diagram of the coupled propagating modes, electromagnetic resonator, and mechanical resonator. The propagating modes $b_{\rm in}(t)$ and $b_{\rm out}(t)$ couple to the electromagnetic resonator at a rate of $\kappa_{\rm ext}$. The resonator mode is $b(t)$, which couples to its environment at a rate of κ_0. Additionally, the resonator couples to the mechanical resonator at a rate of g. The mechanical resonator couples to an environment at a rate of $\kappa_{\rm m}$.

where $\Delta = \omega_{\rm p} - \omega_0 - G\bar{x}$ has a dependence on $\bar{b}$ via $\bar{x}$. This dependence is the analog to the Kerr effect, and it leads to phenomena such as bistability[137, 138, 139].

Dynamic solutions are obtained by examining fluctuations of the field amplitude $b(t)$ and position $x(t)$ about their average values. To simplify the equations of motion, I assume steady state solutions exist[140, 137, 27] and they are of the form $b(t) \to (\bar{b} + b(t))e^{-i\omega_{\rm p}t}$ and $x(t) \to \bar{x} + x(t)$. By inserting these replacements into Eqns. 3.2 and 3.3 and assuming $|b(t)| \ll |\bar{b}|$, the linearized equations of motion are

$$\begin{aligned}
\dot{b}(t) &= (i\Delta - \kappa/2)b(t) - iG\bar{b}x(t) + \sqrt{\kappa_{\rm ext}}b_{\rm in}(t) \\
\ddot{x}(t) &= -\omega_{\rm m}^2 x(t) - \kappa_{\rm m}\dot{x}(t) - \frac{\hbar G}{m_{\rm eff}}\left(\bar{b}b^*(t) + \bar{b}^* b(t)\right) + \eta_{\rm m}(t)/m_{\rm eff}
\end{aligned} \tag{3.5}$$

where the parametric coupling is enhanced because every instance of G is scaled by $\bar{b}$ or $\bar{b}^*$. Thus, the simple increase of the pump amplitude boosts the parametric coupling.

To highlight the similarity between the dynamics of the cavity and mechanical resonator, I recast Eqns. 3.5 in terms of the mechanical resonator's field amplitude $x(t) = x_{\rm zp}\left(c(t) + c^*(t)\right)$ and the pump-enhanced coupling $g = Gx_{\rm zp}\bar{b}$. In a frame rotating with the pump at $\omega_{\rm p}$, these two

substitutions yield

$$\dot{b}(t) = (i\Delta - \kappa/2)b(t) - ig(c(t) + c^*(t)) + \sqrt{\kappa_{\text{ext}}}b_{\text{in}}(t) + \sqrt{\kappa_0}b_0(t)$$
$$\dot{c}(t) = (-i\omega_{\text{m}} - \kappa_{\text{m}}/2)c(t) - i\left(gb^*(t) + g^*b(t)\right) + \sqrt{\kappa_{\text{m}}}c_0(t) \tag{3.6}$$

where the terms with b_0 and c_0 are the fluctuating fields that drive the cavity or the mechanical resonator (see Section 2.1.4), respectively, and the magnitude squared of such terms is normalized to have units of photons/second. As pointed out in Section 2.4.2, the propagating mode $b_{\text{in}}(t)$ is normalized so that $|b_{\text{in}}(t)|^2$ has units of photons/second whereas $|b(t)|^2$ and $|c(t)|^2$ are in units of quanta. Lastly, $b(t)$ couples to $b_{\text{in}}(t)$ and $b_{\text{out}}(t)$ by the input-output relation $b_{\text{out}}(t) = \sqrt{\kappa_{\text{ext}}}b(t) - b_{\text{in}}(t)$. This equation, together with Eqns. 3.6, describes the linearized behavior of the optomechanical system shown in Fig. 3.1. A schematic representation of these equations is shown in Fig. 3.2.

To describe the quantum dynamics of an optomechanical system[48], one promotes the field amplitudes to operators (e.g., take $b \to \hat{b}$) and demands that they satisfy the canonical commutation relations (e.g., require $[\hat{b}, \hat{b}^\dagger] = 1$). This procedure results in the Heisenberg-Langevin equations of motion, which provides a quantum description for the cavity optomechanical system shown in Fig. 3.1. These equations of motion (i.e., the quantized version of Eqns. 3.6) can be generated[141] by starting with the Hamiltonian (here, I drop the hats on the operators)

$$H = \hbar\omega_0\left(b^\dagger b + \frac{1}{2}\right) + \hbar\omega_{\text{m}}\left(c^\dagger c + \frac{1}{2}\right) + \hbar g_0 b^\dagger b\left(c + c^\dagger\right) \tag{3.7}$$

where $g_0 = Gx_{\text{zp}}$ is the single-photon coupling rate. In the above expression, the first two terms describe the harmonic modes of the cavity and resonator, and the last term is the coupling between the field in the cavity and the mechanical resonator.

After writing Eqns. 3.6 in terms of field operators, an asymmetry emerges in the correlation functions for the noise operators. For instance, the fluctuating field that drives the mechanical resonator obeys $\langle c_0^\dagger(t)c_0(t')\rangle = n_{\text{m}}\delta(t - t')$ where n_{m} is the occupation of the mechanical resonator's environment. Because of the commutator relations, the field operator also obeys $\langle c_0(t)c_0^\dagger(t')\rangle = (n_{\text{m}} + 1)\delta(t - t')$. Such correlation functions account for quantum noise present in

the system[131]. To recover a classical description of the system, one simply takes ensemble averages, e.g., take $c_0(t) \rightarrow \langle c_0(t) \rangle$ where $\langle \cdots \rangle$ denotes an ensemble average.

3.1.2 Time-dependent dynamics

The coupling $g = G x_{\mathrm{zp}} \bar{b}$ factor in Eqns. 3.6 depends on the time-dependent pump $\bar{b}$. By varying its strength $\bar{b}$ in time, the coupling becomes $g \rightarrow g(t)$. This time-dependent coupling provides a simple way to rapidly vary the parametric interaction between a propagating microwave field and mechanical motion. By rapidly varying this interaction, two key capabilities emerge. First, the state of a propagating microwave field can be captured and stored in the electromechanical device. Second, it can amplify both the propagating field and the motion of the mechanical resonator.

3.1.2.1 Optimal capture of a propagating microwave field

A propagating microwave field parametrically couples to motion of the mechanical resonator. To capture the state of the propagating microwave field, one utilizes a pump that is detuned below (red-detuned) the microwave circuit resonance with detuning $\Delta_{\mathrm{r}} = -\omega_{\mathrm{m}}$. For this detuning, I eliminate the evolution of the field amplitudes in Eqns. 3.6 by using the replacements $b(t) \rightarrow b(t)e^{-i\omega_{\mathrm{m}}t}$ and $c(t) \rightarrow c(t)e^{-i\omega_{\mathrm{m}}t}$ to move into a frame rotating with the detuned pump. The dynamics are simplified by making the rotating wave approximation, which neglects terms oscillating at $2\omega_{\mathrm{m}}$ because they oscillate significantly faster than any other rates in the equations of motion. In order for this approximation to be valid, the condition $4\omega_{\mathrm{m}} \gg \kappa$ emerges which places the system in the 'resolved sideband' regime[142]. In this regime, Eqns. 3.6 reduce to

$$\begin{aligned} \dot{b}(t) &= -\frac{\kappa}{2} b(t) - i g(t) c(t) + \sqrt{\kappa_{\mathrm{ext}}} b_{\mathrm{in}}(t) \\ \dot{c}(t) &= -\frac{\kappa_{\mathrm{m}}}{2} c(t) - i g^{*}(t) b(t) \end{aligned} \tag{3.8}$$

where I set $c_0(t) = b_0(t) = 0$ for brevity.

Eqns. 3.8 can be generated by using the following Hamiltonian

$$H_{\mathrm{r}} = \hbar g (b c^{\dagger} + c b^{\dagger}). \tag{3.9}$$

This interaction is similar to a beamsplitter Hamiltonian in that it coherently swaps states of the microwave field and the mechanical resonator. Crucially, the time-dependent coupling $g(t)$ enables the beamsplitter's transmission to be rapidly varied. In order to transfer information between a propagating field, $b_{\mathrm{in}}(t)$, and the mechanical resonator, the coupling rate g must be slower than the energy decay of the circuit κ. For $g < \kappa/2$, the dynamics of the circuit follow $b(t)$. Specifically, the evolution of the field in the circuit is $\dot{b}(t) \ll b(t)\kappa/2$ and so its dynamics can be adiabatically eliminated[143, 144].

I make this approximation by setting $\dot{b}(t) = 0$ and so Eqns. 3.8 reduce to a single differential equation given by

$$\dot{c}(t) = -\frac{1}{2}\left(\kappa_{\mathrm{m}} + \frac{4|g|^2}{\kappa}\right) c(t) - \frac{2ig^*}{\sqrt{\kappa}}\frac{\sqrt{\kappa_{\mathrm{ext}}}}{\sqrt{\kappa}} b_{\mathrm{in}}(t). \tag{3.10}$$

The above equation describes how a propagating field couples to mechanical motion. To describe the converse situation, one must use $b_{\mathrm{out}}(t) = \sqrt{\kappa_{\mathrm{ext}}}b(t) - b_{\mathrm{in}}(t)$ together with Eqns. 3.8. After making the adiabatic approximation, one obtains

$$b_{\mathrm{out}}(t) = -\frac{2ig}{\kappa}\frac{\sqrt{\kappa_{\mathrm{ext}}}}{\sqrt{\kappa}} c(t) + \left(2\frac{\sqrt{\kappa_{\mathrm{ext}}}}{\sqrt{\kappa}} - 1\right) b_{\mathrm{in}}(t) \tag{3.11}$$

where $b_{\mathrm{out}}(t)$ depends on the motion of the mechanical resonator.

Crucially, Eqns. 3.10 and 3.11 reveal that the rate at which energy is transferred between motion of the mechanical resonator and the propagating field is simply $\Gamma(t) = 4|g(t)|^2/\kappa$ as depicted in Fig. 3.3a. In terms of $\Gamma(t)$, these two equations reduce to

$$\begin{aligned} \dot{c}(t) &= -\frac{1}{2}(\Gamma(t) + \kappa_{\mathrm{m}})c(t) - e^{-i\psi}\sqrt{\eta\Gamma(t)}b_{\mathrm{in}}(t) \\ b_{\mathrm{out}}(t) &= e^{i\psi}\sqrt{\eta\Gamma(t)}c(t) + (2\eta - 1)b_{\mathrm{in}}(t) \end{aligned} \tag{3.12}$$

where $\eta = \kappa_{\mathrm{ext}}/\kappa$ is the coupling efficiency and $\psi = \mathrm{Arg}(-ig)$ is the phase of the pump. Eqns. 3.12 concisely describe how a propagating field interacts with the mechanical resonator.

To understand how Eqns. 3.12 reveal the ability to cool the mechanical resonator's motion, consider capturing a noisy field $b_{\mathrm{in}}(t)$. For this case, I assume that this field is emitted from a

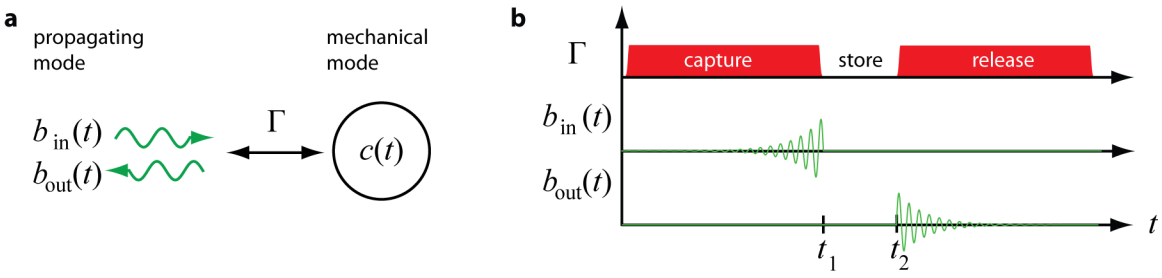

Figure 3.3: Diagram depicting the capture, storage, release of a propagating field. **a,** The diagram depicts the propagating modes $b_{\rm in}(t)$ and $b_{\rm out}(t)$ coupled to the mechanical mode $c(t)$ at a rate of Γ. In this case, the circuit mode was adiabatically eliminated and the mechanical dissipation was neglected. **b,** The plots depict the coupling Γ and propagating modes as a function of time. At time $t < t_1$, the electromechanical device captures an input field $b_{\rm in}(t)$ and converts it to mechanical motion. During storage, $\Gamma = 0$. After storage, the coupling pulses on at $t > t_2$ and converts the energy in the mechanical mode back into a propagating field.

source of Johnson noise, and that the mechanical resonator is driven by a noisy field $c_0(t)$. The noise properties of these two fields are succinctly described by[131]

$$\langle b_{\rm in}^\dagger(t) b_{\rm in}(t')\rangle = n_{\rm e}\delta(t-t') \quad \text{and} \quad \langle c_0^\dagger(t) c_0(t')\rangle = n_{\rm m}\delta(t-t') \tag{3.13}$$

where $n_{\rm e}$ and $n_{\rm m}$ are the average occupations for the electrical and mechanical mode, respectively, and $\delta(t-t')$ is a delta function. The solutions to Eqns. 3.12 contain integrals that consume the delta functions, and for constant coupling $\Gamma(t) \to \Gamma$ they reveal that the mechanical resonator's occupation $\langle c^\dagger(t)c(t)\rangle$ decays in time:

$$\langle c^\dagger(t)c(t)\rangle = \langle c^\dagger(0)c(0)\rangle e^{-(\Gamma+\kappa_{\rm m})t} + \frac{\kappa_{\rm m}}{\Gamma+\kappa_{\rm m}} n_{\rm m} \tag{3.14}$$

where $c(0)$ is the initial state of the mechancial resonator. Additionally, I assumed that the microwave mode is in a 'cold' vacuum state such that $n_{\rm e} = 0$, and the mechanical mode is 'hot' with $n_{\rm m} \gg 1$. The above expression shows that by capturing a cold microwave field, one can cool the mechanical resonator to its quantum ground state provided that $\Gamma \gg \kappa_{\rm m} n_{\rm m}$. In this regime, the electromechanical device is said to be 'quantum-enabled' because it can process a quantum signal with low-added noise.

Beyond capturing a noisy field, one can efficiently capture an arbitrary input field $b_{\rm in}(t)$. For

this task, one must choose an optimal $\Gamma(t)$. If $b_{\rm in}(t)$ has a temporal envelope that rises exponentially in time as depicted in Fig. 3.3b, then $\Gamma(t)$ is simply a piecewise constant function[64]. However, efficient capture of a field with an arbitrary temporal envelope requires modulating $\Gamma(t)$ beyond that of a piecewise constant function.

For $\eta \approx 1$, efficient capture of an input field is equivalent to minimizing the reflected energy. To determine the form of $\Gamma(t)$ required to minimize the reflected energy[144], one can use the Euler-Lagrange equation to calculate the stationary point of the reflected energy, $\int_0^T |b_{\rm out}(t)|^2 dt$, where $b_{\rm out}(t)$ is a functional of $\Gamma(t)$ given by Eqns. 3.12. The result of this minimization procedure yields

$$\Gamma(t) = \frac{e^{\kappa_{\rm m} t}|b_{\rm in}(t)|^2}{\frac{b_{\rm in}(0)^2}{\Gamma(0)} + \int_0^t e^{\kappa_{\rm m} t'}|b_{\rm in}(t')|^2 dt'} \tag{3.15}$$

where $\Gamma(0)$ is the coupling at $t = 0$. This expression shows that simply by modulating $\Gamma(t)$, one can efficiently capture an arbitrary $b_{\rm in}(t)$. I use this capability to efficiently capture fields emitted from the photon source discussed in Chapter 4.

3.1.2.2 Pulsed amplification of a microwave field and mechanical motion

To amplify a propagating field and motion of the mechanical resonator, one utilizes a blue-detuned pump with detuning $\Delta_{\rm b} = +\omega_{\rm m}$. For this detuning, Eqns. 3.6 can be recast in terms of $\Gamma(t) = 4|g(t)|^2/\kappa$ where $g(t)$ is the coupling between the field in the circuit and the mechanical resonator due to the blue-detuned pump. As in the previous section, I can reduce Eqns. 3.6 to

$$\begin{aligned} \dot{c}^*(t) &= \frac{1}{2}\Gamma(t)c^*(t) + \sqrt{\eta\Gamma(t)}b_{\rm in}(t)e^{-i\psi} \\ b_{\rm out}(t) &= \sqrt{\eta\Gamma(t)}e^{i\psi}c^*(t) + (2\eta - 1)b_{\rm in}(t) \end{aligned} \tag{3.16}$$

where $\eta = \kappa_{\rm ext}/\kappa$ is the coupling efficiency and $\psi = {\rm Arg}(-ig)$ is determined by phase of the blue-detuned pump.

To generate the equations of motion used to obtain Eqns. 3.16, one employs the Hamiltonian

$$H_{\rm b} = \hbar g(b^\dagger c^\dagger + bc). \tag{3.17}$$

This interaction is similar to that of a two-mode squeezer Hamiltonian[145, 98] which amplifies[44] the energy in the two coupled modes. For Eqns. 3.16, the mechanical and microwave modes are coupled through $\Gamma(t)$. While $\Gamma(t)$ is pulsed on, the circuit emits a propagating field with a temporal envelope that rises exponentially at a rate of $\Gamma/2$. Crucially, the state of the emitted field depends on both the states of the mechanical resonator and the input field before amplification.

To see this dependence, I solve Eqns. 3.16 using a piecewise constant coupling $\Gamma(t) \to \Gamma$ that is pulsed on at time $t = 0$. For this coupling, the output field is

$$b_{\text{out}}(t) = c^*(0)\sqrt{\eta\Gamma} \cdot e^{i\psi} h(t) + \Gamma\eta \cdot (h \star b_{\text{in}})(t) + (2\eta - 1) b_{\text{in}}(t) \tag{3.18}$$

where $h(t) = \exp(\Gamma t/2)$ and $\star$ denotes the convolution operation. This field depends on both the initial state of the resonator at $t = 0$ and the input field while the coupling is pulsed on.

For $b_{\text{in}}(t) = 0$ at $t \geq 0$, a field emerges from the circuit that contains the initial state of the resonator. This state can be prepared by capturing a propagating field while $t < 0$. After capture, $\Gamma(t)$ is pulsed on and the output field is

$$b_{\text{out}}(t) = c^*(0)\sqrt{\Gamma\eta} \cdot e^{i\psi} h(t) \tag{3.19}$$

which has a conjugated phase relative to that of the mechanical resonator.

If instead a field $b_{\text{in}}(t)$ is injected while the coupling is pulsed on, a pulse emerges from the circuit that depends on the state of the input field. Consider a propagating field that emerges from a cavity. This field has a temporal envelope given approximately by

$$b_{\text{in}}(t) = \sqrt{\gamma} B e^{-\gamma t/2} \Theta(t) \tag{3.20}$$

where $\int_{-\infty}^{\infty} |b_{\text{in}}(t)|^2 \, \mathrm{d}t = |B|^2$ is the total energy contained in the field and γ is its power decay rate. This field is chosen to be similar to what is emitted by the photon source. While the coupling is pulsed on, the expression for the output field takes on a simple form when $\gamma = \Gamma$. In this case, Eqn. 3.18 reduces to

$$b_{\text{out}}(t) = 2\sqrt{\eta\Gamma} B \sinh(\Gamma t/2) + (2\eta - 1) b_{\text{in}}(t) \tag{3.21}$$

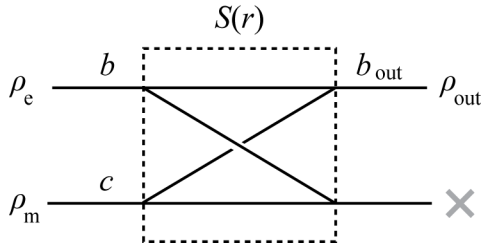

Figure 3.4: Model of a two-mode parametric amplifier. The electrical mode b interacts with the mechanical mode c through the two-mode squeezer interaction $S(r)$ where r is the squeezing parameter. The output mode is b_{out}. In terms of density matrices, the input electrical and mechanical states are ρ_{e} and ρ_{m}, respectively, and the output state is ρ_{out}. The cross indicates the output mechanical mode is not measured.

The above expression shows that the temporal envelope of the output field is approximately a rising exponential, and the phase of the output field is independent of the blue-detuned pump's phase.

3.1.3 Operation as a linear amplifier

The two-mode squeezer interaction introduced in the previous section enables the electromechanical device to function as a phase-insensitive parametric amplifier. Such an amplifier increases the amplitude of a signal regardless of its input phase. For an ideal, phase-insensitive parametric amplifier, the absolute minimum amount of added noise is half a quantum[126]. Because the added noise can in principle be limited by Heisenberg's uncertainty principle, this type of amplifier is well-suited for measuring a signal at the quantum level[121, 124]. When operating the electromechanical device as an amplifier, the signal to be measured is either a quantum state of the input microwave field or the mechanical resonator.

A model of the parametric amplifier realized using the electromechanical device is diagrammed in Fig. 3.4. This model has two input modes b and c that represent the microwave field and mechanical resonator, respectively. For the amplifier's output, we measure the outgoing microwave field b_{out}. This field relates to the amplifier's two inputs through the two-mode squeezer operator S defined by

$$b_{\text{out}} = S^{\dagger} b S = b \cosh(r) - c^{\dagger} \sinh(r) \tag{3.22}$$

where $S(r) = \exp\big(r(bc - b^\dagger c^\dagger)\big)$ and r is the squeezing parameter[146, 147, 148]. Crucially, this parameter determines the gain of the parametric amplifier.

To model how the amplifier transforms a quantum state, I describe its input and output in terms of density matrices. Specifically, the input electrical and mechanical states are taken to be ρ_e and ρ_m, respectively, and the output is ρ_out. Ideally, one of the two input modes is in its quantum ground state. Prior to executing the two-mode squeezer operation, the second input mode is in the quantum state of interest. For example, it could be a single-photon state. The result of the two-mode squeezer operation is a joint entangled state $S\rho_\mathrm{e} \otimes \rho_\mathrm{m} S^\dagger$ where $\otimes$ denotes a tensor product. Because I only measure the outgoing electrical mode, the resulting output state is

$$\rho_\mathrm{out} = \mathrm{tr}_\mathrm{m}\left(S\rho_\mathrm{e} \otimes \rho_\mathrm{m} S^\dagger\right) \tag{3.23}$$

where tr_m denotes a partial trace over the mechanical mode.

Experimentally, one does not measure ρ_out directly. Instead, it can be determined by using quantum state tomography as discussed in Section 2.5. In this approach, I simultaneously measure the quadrature amplitudes X and Y of b_out. Repeated measurements of these quadrature amplitudes are sampled from the Husimi Q-function that describe the output state. This function is given by

$$Q_\mathrm{out}(\alpha) = \frac{1}{\pi}\langle\alpha|\,\rho_\mathrm{out}\,|\alpha\rangle \tag{3.24}$$

where $\alpha = X + iY$. In order to determine the input state of interest from the above expression, it must be related to the Q-function of that state.

Conveniently[126], the output Q-function is a scaled version of the input Q-function when $r \gg 1$. If the primary mode contains the signal of interest and the secondary mode is in its quantum ground state, the output Q-function is simply

$$Q_\mathrm{out}(\alpha) = Q_\mathrm{in}(\alpha/\sqrt{\mathcal{G}})/\mathcal{G} \tag{3.25}$$

where $\sqrt{\mathcal{G}} = \cosh(r)$. This result demonstrates that obtaining Q_out is equivalent to Q_in up to a scale factor. Having obtained Q_in, one determines the input state ρ_in using the method of maximum

likelihood parameter estimation discussed in Section 2.5.3. Importantly, ρ_{in} could either be ρ_{e} or ρ_{m} because either the electrical or mechanical mode can be regarded as the primary mode.

The expression given by Eqn. 3.25 is only true if the secondary mode is in its quantum ground state. When this is not the case, the input Q-function of the signal becomes convolved with the noise in the second mode. Suppose the input signal is in the primary mode, and the secondary mode is in a thermal state with a mean occupation of n_{th}. Then the output Q-function is

$$Q_{\mathrm{out}}(\alpha) \propto (Q_{\mathrm{in}} \star \mathcal{N})\,(\alpha/\sqrt{\mathcal{G}}) \tag{3.26}$$

where $\star$ denotes a convolution operation, $\mathcal{N}$ is a Gaussian distribution with a variance of n_{th} in each quadrature, and the proportionality is made exact by enforcing proper normalization of Q_{out}. From this expression, one can determine ρ_{in} from Q_{out} simply by taking the thermal occupation of the secondary mode into account.

3.1.4 Frequency-tunable device using electrostatic actuation

The previous two sections showed how a single electromechanical device can mode-convert and amplify a signal. But these capabilities are limited to a narrow bandwidth if the device is fixed in frequency. By making the device tunable in frequency, it can manipulate a signal centered anywhere in its operation band. This tunability enables the electromechanical device to be compatible with the fixed-frequency photon source discussed in Chapter 4.

The center frequency of the electromechanical device is inherently tunable because it employs a variable capacitor. By applying a force that pulls the flexible capacitor plate towards its other plate, the capacitance and thus resonant frequency of the device can be made tunable. A simple way to generate this force is by imposing a static voltage across the two plates, which results in an attractive electrostatic potential between them. This design is inherently limited in its tunability because the electrostatic force can cause the flexible capacitor plate to collapse and stick to the other plate. A way to circumvent this limitation is to introduce a third electrode into the design[149].

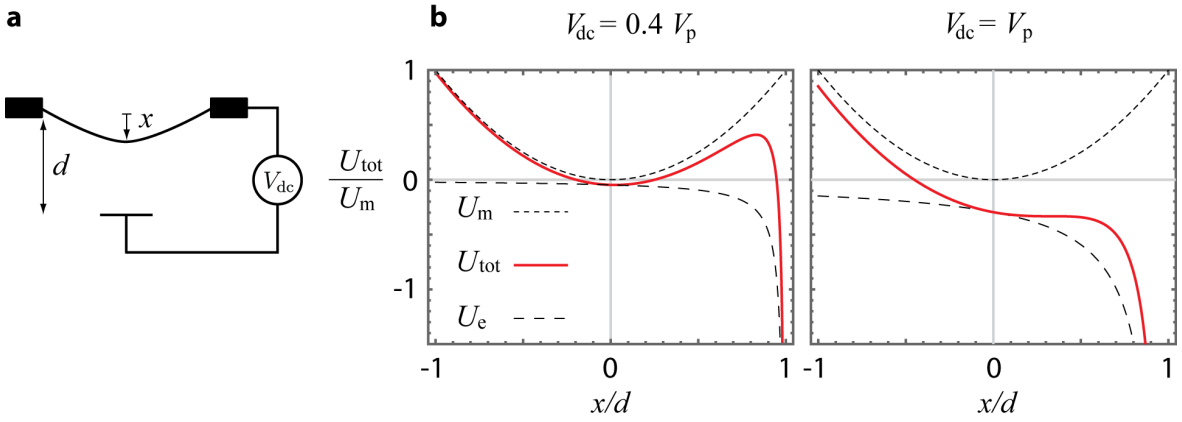

Figure 3.5: Two-electrode model of a tunable capacitor. **a,** The diagram shows a capacitor whose upper plate is a flexible membrane. A source imposes a voltage V_{dc} across the two electrodes of the capacitor. **b,** The plots show the total potential energy U_{tot} of the capacitor as a function of the membrane deflection, where U_m and U_e are the mechanical and electrostatic contributions to the total energy. When the applied voltage V_{dc} is less than the pull-in voltage V_p, the total potential has a stable local minimum near $x = 0$. But once $V_{dc} > V_p$, the local minimum near $x = 0$ vanishes and so the membrane collapses towards the lower plate.

3.1.4.1 Two-electrode model for static tuning

To understand how a static voltage can tune a capacitor, consider the simple model shown in Fig. 3.5a. The upper plate of the capacitor is a flexible metallic membrane, and the lower plate is a fixed electrode. These two plates are separated by a distance d. In order to deflect the flexible plate by a displacement x, an external source imposes a constant voltage V_{dc} across the two plates and thus creates an attractive electrostatic force between them. This force is described by the electrostatic potential energy $U_e = -C(x)V_{dc}^2/2$ where the minus sign is due to the work performed by the source in order to keep V_{dc} constant. As the electrostatic force deflects the flexible plate, it experiences a restoring force that is approximately harmonic given by $U_m = kx^2/2$ where k is the effective spring constant of the membrane. As such, the net force that the membrane experiences is described by the total energy $U_{tot} = U_e + U_m$. This energy is minimized when the two plates stick together at $x = d$. However, the mechanical restoring force of the membrane enables a stable local minimum to exist near $x \approx 0$ as shown in Fig. 3.5b.

Once the electrostatic force overwhelms the mechanical restoring force, the membrane col-

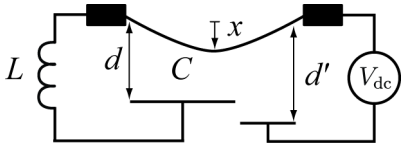

Figure 3.6: A three-electrode tunable capacitor incorporated in a microwave circuit. The diagram shows a variable capacitor (C) shunted by an inductor (L). A third electrode electrostatically actuates the flexible membrane. This electrode is recessed so that $d' > d$.

lapses and sticks to the other plate. This effect occurs when the minimum near $x \approx 0$ vanishes due to $V_{\rm dc}$ exceeding a certain 'pull-in' voltage $V_{\rm p}$ as shown in Fig. 3.5b. Both the capacitor's geometry and membrane's spring constant set the scale for the pull-in voltage. Regardless of this scale, the equilibrium position of the membrane when $V_{\rm dc} = V_{\rm p}$ is $x = d/3$.

The inherent pull-in effect limits the smallest gap achievable in a two-electrode capacitor to be no more than $2d/3$. As such, if one were to incorporate this capacitor into an inductor-capacitor (LC) microwave circuit, its resonant frequency $\omega_{\rm LC}$ could not be reduced below $\sqrt{2/3}\omega_{\rm LC}$ or about 80% of its initial value. In practice, parasitic capacitance in the circuit will provide a further reduction in this dynamic range. To enhance the dynamic range of the tunable capacitor, its design must be altered.

3.1.4.2 Benefit of a third electrode

The addition of a third electrode can avoid the pull-in effect that limits the tuning of a two-electrode capacitor. A schematic of this approach is depicted in Fig. 3.6. The variable capacitor is shunted by an inductor in order to form an LC circuit. To tune its center frequency, a third electrode creates an electrostatic force on the flexible membrane. The key to the design is a recessed third electrode. This design choice enables the membrane's deflection to approach $x \to d$, and so the circuit's resonant frequency can in principle assume $\omega_{\rm LC} \to 0$. In practice, this tuning is limited by effects such as the Casmir force and bound charges on the two electrodes[65].

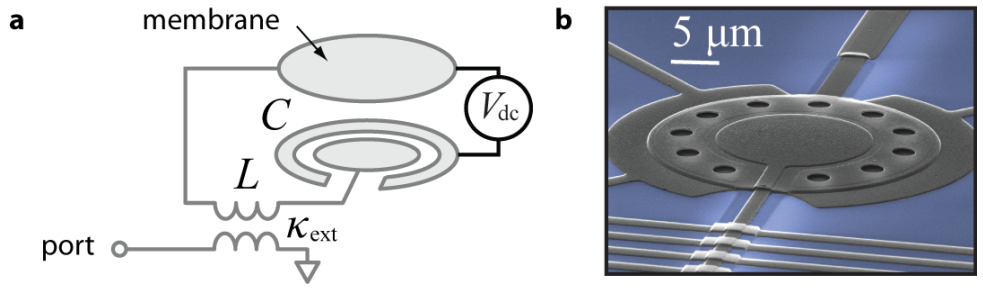

Figure 3.7: Schematic and micrograph of the electromechanical device. **a,** The diagram shows a simplified schematic of the electromechanical device. The upper plate of the capacitor is a thin (100nm) tensioned membrane, and beneath it is a microwave electrode (center) and an actuation electrode (annular region). A voltage source imposes a voltage V_{dc} between the actuation electrode and the membrane. The circuit elements have parameters of $L \approx 10$ nH and $C \approx 40$ fF, thereby creating an inductor-capacitor (LC) circuit that resonates at a microwave frequency. Microwave power is delivered to the circuit via a port connected to a transmission line, which inductively couples to the circuit at a rate of κ_{ext}. **b,** A false-color scanning electron micrograph of the aluminium membrane and nearby circuitry. The circuit (gray) is fabricated on a sapphire substrate (blue).

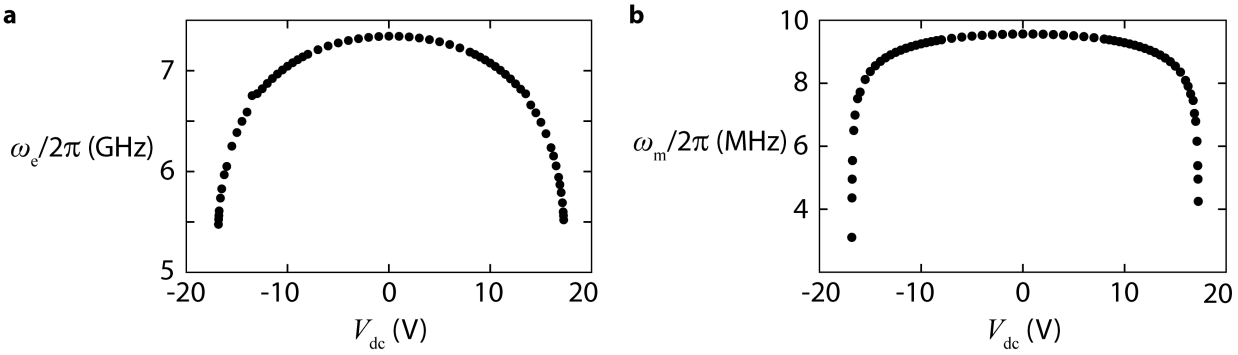

Figure 3.8: Frequency tuning of the electromechanical device. **a,** The plot shows the measured center frequency ω_e of the microwave circuit as a function of the applied voltage V_{dc}. **b,** The plot is similar to **a** but for the mechanical resonant frequency ω_m.

3.2 Characterization of the electromechanical device

In order to operate the electromechanical device, it is cooled to a temperature of less than 25 mK in a dilution refrigerator so that its aluminium circuitry superconducts. A diagram and picture of the electromechanical device is shown in Fig. 3.7. Design and construction methods of the device are discussed elsewhere[150, 149].

Table 3.1: Parameters of the electromechanical device. All parameters were measured with an applied dc voltage of $V_{\mathrm{dc}} = 5.83$ V.

Symbol	Description	Value and units
$\omega_{\mathrm{LC}}/2\pi$	Circuit resonant frequency	7.283 360 GHz
$\kappa_{\mathrm{LC}}/2\pi$	Circuit decay rate	3 ± 0.1 MHz
$\kappa_{\mathrm{ext}}/2\pi$	Circuit decay rate into the transmission line	2.59 ± 0.01 MHz
$\omega_{\mathrm{m}}/2\pi$	Mechanical resonant frequency	9.345 MHz
$\kappa_{\mathrm{m}}/2\pi$	Mechanical decay rate	14.5 ± 1 Hz
n_{m}	Average occupancy of the mechanical oscillator	42 ± 2
$g_0/2\pi$	Electromechanical coupling	283 ± 14 Hz

Parameters of the electromechanical device are determined by measuring its microwave response. The device has one port, which provides electrical access to the LC circuit. A microwave probe with an amplitude V_{in} is injected into the port. After the probe interacts with the device, the reflected outgoing field V_{out} is then measured. This measurement technique enables one to determine the response of the circuit and properties of the mechanical resonator. The parameters for the electromechanical device are presented in Table 3.1.

3.2.1 Circuit parameters and frequency tuning

The measured response of the device to a microwave probe tone reveals its circuit parameters. By injecting a microwave tone into the device and comparing it to the reflected signal, one obtains a single scattering parameter $S_{11}(\omega) = V_{\mathrm{out}}/V_{\mathrm{in}}$ that characterizes the device response at a particular frequency[151]. This probe is then swept over a range of frequencies that encompass the circuit's bandwidth. Fitting the resulting measurements of $S_{11}(\omega)$ enables one to extract the resonant frequency of the circuit (ω_{LC}), its external coupling rate (κ_{ext}), and total coupling rate (κ_{LC}). Parameters of the electromechanical device are presented in Table 3.1.

To verify the frequency tuning of the electromechanical device, we measure its response while varying the voltage V_{dc} applied to the actuation electrode. For both positive and negative voltages, the resonant frequency of the circuit is reduced as shown in Fig. 3.8a. At the lowest achievable resonant frequency, the circuit tunes by more than 600 times its total bandwidth. At $V_{\mathrm{dc}} \approx 17$ V,

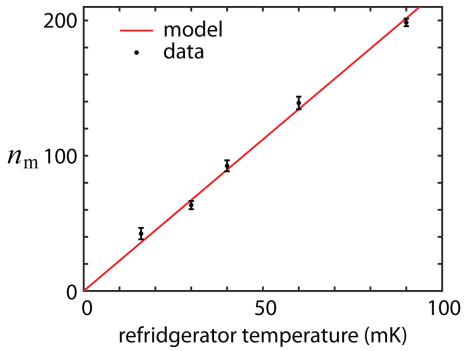

Figure 3.9: Electromechanical coupling rate and equilibrium occupation of the aluminium membrane. The black points show the average energy of the mechanical resonator (in units of quanta) as the refrigerator's base temperature was varied. Error bars show the standard error of the mean from five consecutive measurements. The solid line represents the expected mechanical occupation n_{m} assuming the resonator is in equilibrium with its environment at temperatures between 30 mK and 100 mK and an electromechanical coupling rate $g_0/2\pi = 283 \pm 14$ Hz.

an instability emerges that causes the membrane to stick to the electrode beneath it as evidenced by $\omega_{\mathrm{m}} \to 0$ as shown in Fig. 3.8b. However, when the applied voltage is reset to $V_{\mathrm{dc}} = 0$, the circuit returns to within $\sim 5\%$ of its initial center frequency. Operation of the device past the point of instability is not recommended.

3.2.2 Electromechanical coupling and mechanical occupation

The electromechanical coupling g_0 as defined by Eqns. 3.7 is determined by measuring the microwave response of the electromechanical device. A microwave pump is injected into the device, and motion of the aluminum membrane modulates the pump and produces modulation sidebands on the reflected pump. The difference between the upper sideband and pump frequency is the resonant frequency of the membrane (ω_{m}), whereas the magnitude of the sidebands indicate the coupling strength between the microwave circuit and the aluminum membrane. The amount of power in the sideband (P_{m}) at a frequency ω_{m} above the injected microwave pump is proportional to the amount of power in the injected microwave pump (P_{c}):

$$\frac{P_{\mathrm{m}}}{P_{\mathrm{c}}} = \frac{g_0^2}{2}\frac{\langle x^2 \rangle}{x_{\mathrm{zp}}^2}\frac{\kappa_{\mathrm{ext}}^2}{\Delta^2 + (\kappa_{\mathrm{ext}} - \kappa/2)^2}\frac{1}{(\Delta + \omega_{\mathrm{m}})^2 + (\kappa/2)^2} \tag{3.27}$$

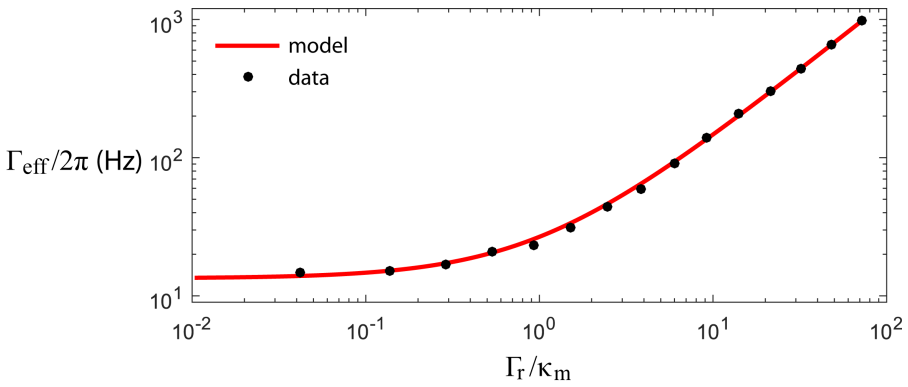

Figure 3.10: Mechanical relaxation rate. The plot shows the measured effective mechanical damping $\Gamma_{\rm eff} = \kappa_{\rm m} + \Gamma_{\rm r}$ as a function of the pump strength $\Gamma_{\rm r}$ normalized to the intrinsic mechanical linewidth $\kappa_{\rm m}$. The solid line is a fit to the data that yields $\kappa_{\rm m}/2\pi = 14.5$ Hz.

where Δ is the difference between the pump frequency and the microwave circuit's resonant frequency, $x_{\rm zp}$ is the zero-point fluctuations of the membrane, and $\langle x^2 \rangle$ describes the motion of the membrane. For a membrane in equilibrium with the thermal environment provided by the dilution fridge, $\langle x^2 \rangle = 2x_{\rm zp}^2 n_{\rm m}$, where $n_{\rm m} \approx k_{\rm B}T/\hbar\omega_{\rm m}$ is the average phonon occupation of the membrane for dilution refrigerator base temperature T.

To determine g_0, we vary the refrigerator temperature and monitor the ratio $P_{\rm m}/P_{\rm c}$. We express this ratio as an effective phonon occupation, $n_{\rm m}$. At high temperatures (30-100 mK), the membrane is in thermal equilibrium with the refrigerator as evidenced by the linear relationship between T and $n_{\rm m}$ shown in Fig. 3.9. From this relationship, we extract an electromechanical coupling of $g_0/2\pi = 283 \pm 14$ Hz. At the refrigerator base temperature of approximately 19 mK, the phonon occupation number saturates to $n_{\rm m} = 42 \pm 2$. Although this occupation is well above the ground state, it can be further reduced by actively cooling the motion of the membrane as pointed out in Section 3.1.2.1.

3.2.3 Mechanical relaxation rate

In order to determine the intrinsic mechanical relaxation rate $\kappa_{\rm m}$, we measure the ringdown time of the aluminium membrane. We probe the membrane's motion by injecting a tone with a

detuning $\Delta_r = -\omega_m$ into the circuit. To coherently drive the membrane's motion, we briefly pulse on an additional tone centered at the circuit's resonance. These two tones create a time-varying force that drives the motion of the membrane at its resonant frequency of ω_m. Immediately after the drive tone pulses off, we measure the amplitude decay of the probe's upper modulation sideband.

Because this tone also damps the motion of the membrane (see Section 3.1.2.1), we monitor the ringdown decay time as a function of the probe strength as shown in Fig. 3.10. A fit to this decay yields the effective mechanical damping $\Gamma_{eff} = \kappa_m + \Gamma_r$ where Γ_r is the damping rate that the probe induces. For $\Gamma_r \gg \kappa_m$, the intrinsic mechanical relaxation rate is obscured because $\Gamma_{eff} \approx \Gamma_r$. At low damping, the ringdown measurements reveal that Γ_{eff} asymptotes to the intrinsic mechanical relaxation rate.

Chapter 4

Design and characterization of the photon source

Photons are ideal carriers of quantum information because they can rapidly and efficiently propagate in cables or optical fibers[152, 153]. At microwave frequencies, photons are electrical signals[116] that propagate in a transmission line. Such photons are crucial for emerging applications in quantum information processing using superconducting circuits. As such, single-photon sources at microwave frequencies are actively under development[154, 155, 121, 156, 124, 157, 158, 159, 119, 160, 86]. Here, I realize a photon source by coupling a quantum bit (qubit) to one mode of a microwave cavity. The qubit enables a single photon to be created in the cavity mode, which then decays into a mode that propagates in the transmission line. Crucially, this source enables the communication of quantum information because it can generate propagating qubits[161] encoded as superpositions of zero and one photons.

In this chapter, I describe the design and characterization of an on-demand photon source that is compatible with the electromechanical device. Section 4.1 describes the design of the photon source, which consists of a cQED system formed by a qubit in a cavity. Section 4.2 presents the characterization of these two elements. Lastly, Section 4.3 demonstrates that the cQED system can efficiently emit single photons with spectral and temporal content that is compatible with the electromechanical device.

4.1 Design of the photon source

The electromechanical device processes narrow-bandwidth signals at microwave frequencies, as discussed in Section 5.3. To ensure compatibility of the electromechanical device with a single photon source, the source must produce propagating microwave-frequency photons with a sufficiently narrow spectrum. As such, entering this regime requires a highly coherent circuit quantum electrodynamics (cQED) system[115, 96]. This system is a superconducting quantum circuit realized by embedding a transmon qubit in a high-quality microwave cavity[79].

4.1.1 Qubit design

The qubit is formed by an inductor-capacitor (LC) circuit[162, 163]. To operate it as a qubit, the circuit must have an anharmonic energy spectrum so that individual transitions can be addressed. Such an anharmonic energy-level spacing is achieved by making the circuit nonlinear. The linear part of the circuit is described by the Hamiltonian

$$H = \frac{Q^2}{2C} + \frac{\Phi^2}{2L} \tag{4.1}$$

where Q is the charge on the capacitor and Φ is the flux through the inductor. This Hamiltonian is the same as a harmonic oscillator with

$$H = \hbar\omega_0 \left(a^\dagger a + \frac{1}{2}\right) \tag{4.2}$$

where $\omega_0 = 1/\sqrt{LC}$ and a is a linear combination of charge and flux operators[133]. Because all the energy levels are equally-spaced by $\hbar\omega_0$ as discussed in Section 2.1, this circuit cannot act as a qubit. However, it can be made nonlinear by writing Eqn. 4.2 as

$$H = \hbar\omega_0 \left(a^\dagger a + \frac{1}{2}\right) - \hbar\frac{K}{2}(a^\dagger a)^2 \tag{4.3}$$

where K is the shift in the resonant frequency for each excitation in the oscillator. This parameter characterizes the circuit's anharmonanicity at the quantum level[164], and the effect is a direct analog to the optical Kerr effect[165]. If the nonlinearity in the circuit is sufficiently strong such

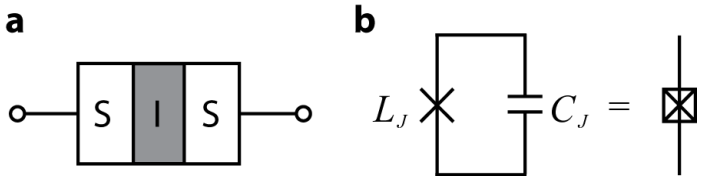

Figure 4.1: Schematic of a Josephson junction. **a,** The diagram depicts two superconducting electrodes (S) separated by an insulating layer (I). This device forms a Josephson junction. **b,** A circuit model of a Josephson junction with inductance L_J and capacitance C_J. The circuit symbol for a Josephson junction with the parasitic capacitance is shown on the right.

that $|K|$ is much larger than the effective linewidth of the circuit, then it is possible to individually address two energy levels and treat them as a qubit. Entering this regime with a circuit requires a Josephson junction, which functions as a nonlinear inductor that does not introduce dissipation or dephasing into the circuit.

4.1.1.1 A Josephson junction provides the nonlinearity

The key nonlinear element in a superconducting qubit is a Josephson junction[166]. It is formed by connecting together two superconducting electrodes with a weak link[167]. A single Josephson junction is depicted in Fig. 4.1a. In each superconducting electrode, electrons bind together to form Cooper pairs with charge $2e$. All the Cooper pairs in each electrode are in the same quantum state and can described by a single wave function with a phase. Because the wave functions overlap in the junction, Cooper pairs tunnel through the weak link. Crucially, the collective behavior of all the Cooper pairs in the Josephson junction are parameterized by the difference in the phases δ between the wave functions for each electrode.

A pair of constitutive relations describe the flow of Cooper pairs through the junction[168, 169]. Without any voltage applied across the electrodes, a supercurrent will flow according to

$$I_{\mathrm{s}} = I_{\mathrm{c}} \sin(\delta) \tag{4.4}$$

where I_{c} is the maximum supercurrent the junction can support before it switches to a dissipative

state. If a voltage V is applied across the electrodes, the phase evolves according to

$$V = \frac{\Phi_0}{2\pi}\frac{\partial \delta}{\partial t} \tag{4.5}$$

where $\Phi_0 = h/2e$ is the magnetic flux quantum.

The constitutive relations for a Josephson junction reveal that it is a nonlinear circuit element. By using the expression for the voltage drop across an inductor, together with Eqn. 4.5, one finds that the inductance is

$$L = \frac{L_J}{\cos(\delta)} \tag{4.6}$$

where $L_J = \Phi_0/I_c$ is the Josephson inductance and I_c is its critical current. Importantly, I_c is the sole parameter that determines the strength of the nonlinear inductance. In addition to an inductance, the junction has capacitance C_J from the electrodes. These two elements form a circuit as shown in Fig. 4.1b. This circuit is analogous to an LC resonator with a resonant frequency of

$$\omega_p = \sqrt{\frac{1}{L_J C_J}}, \tag{4.7}$$

called the 'plasma frequency' because charge sloshes back and forth in a way that is similar to that of a bulk plasma oscillation[170]. For $\delta \ll 1$, this frequency can be expressed as

$$\hbar\omega_p = \sqrt{8E_J E_C} \tag{4.8}$$

where the Josephnson energy $E_J = \Phi_0 I_c/2\pi$ is the characteristic energy stored in the Josephson inductance, and the charging energy $E_C = e^2/2C_J$ is the energy required to charge the capacitor with one electron.

Both the charging energy and Josephson energy determine the energy spectrum of the nonlinear circuit shown in Fig. 4.1. The nonlinear contribution to the Hamiltonian is from the Josephson energy of the junction given by

$$H_J = -E_J\left(1 - \cos\delta\right). \tag{4.9}$$

By expanding H_J to fourth order, linear and nonlinear terms for the inductance emerge. The nonlinear term relates to the anharmonicity K in Eqn. 4.3 by

$$\frac{K}{2} = \frac{E_J}{4!}\delta^4 \tag{4.10}$$

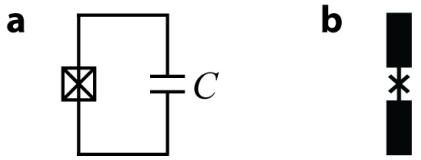

Figure 4.2: Schematic of a transmon. **a,** A Josephson junction is shunted by an external capacitance C. **b,** Incorporating a Josephson junction in a coplanar capacitor realizes a transmon qubit. The metal paddles above and below the junction form its shunting capacitance, and they provide the circuit with an effective dipole moment.

This term sets the scale of the nonlinearity, and is responsible for making the circuit's energy spectrum anharmonic.

4.1.1.2 Introduction to the transmon qubit

The transmon is a charge qubit with improved coherence times[171, 172]. It consists of a Josephson junction shunted by an external capacitance, as shown in Fig. 4.2. This capacitance is key to the circuit design because it reduces the sensitivity of the qubit's transition frequency to charge fluctuations on the junction. As such, the transmon suppresses the undesired influence of charge fluctuations on the qubit's coherence times[173]. These times have increased from nanoseconds[174, 175, 176] to microseconds[172, 177] because of the transmon circuit design.

Operating a charge qubit in the transmon regime requires $E_J/E_C \gg 1$, which is well-described in the literature[171]. Briefly, operating in this regime enables the variation in the circuit's energy level spacing to be suppressed exponentially in E_J/E_C. As such, the transition frequency used for the qubit is approximately independent of any charge noise. Fortunately, the anharmonicity decreases only as a weak a power in E_J/E_C, and it remains sufficiently anharmonic for selective control over individual transitions. In the transmon regime, the anharmonicity is given by $|K_q| \approx -E_C$.

4.1.1.3 Transmon qubit parameter constraints

The E_J and E_C parameters for my qubit design are constrained for three reasons. First, in order to have a highly coherent qubit, we want to operate it deep in the transmon regime with

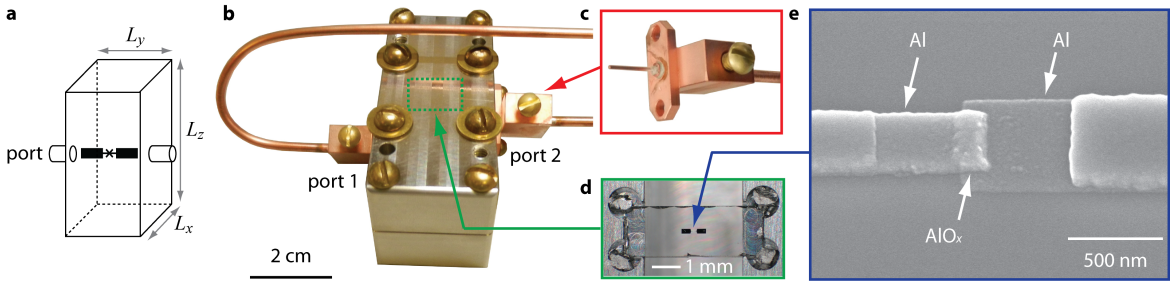

Figure 4.3: Schematic and picture of the qubit in a cavity. **a,** A schematic depicts the transmon qubit incorporated in a superconducting cavity. The cavity has dimensions set by $L_y < L_x < L_z$. **b,** A picture of the assembled cavity with two copper cables connected to the ports. **c,** The picture shows the launcher made from a non-magnetic coaxial cable (UT-85C-LL Microcoax). **d,** Optical microscope image of a single-junction transmon qubit fabricated on a sapphire substrate. The chip rests inside the cavity near a region indicated by the dotted box. **e,** A scanning electron micrograph of the single-junction transmon qubit. Layers of aluminium (Al), aluminium oxide (AlO_x), and aluminium form the junction. Micrograph courtesy of Luke Burkhart.

$E_J/E_C \sim 50$. This regime enables the qubit to have coherence times that exceed 10 μs, which are readily achievable using standard superconducting circuit designs[173]. Second, the qubit's transition frequency $\omega_q/2\pi \approx \sqrt{8E_JE_C}/h$ must be sufficiently detuned from the cavity so that the coupled qubit-cavity system can be in the dispersive limit[178, 116]. As part of entering this limit, we choose a qubit frequency to be in the range of approximately $5.5 - 6.5$ GHz. Third, we want to drive individual transitions with fast, transform-limited pulses. In terms of the anharmonicitiy[171], the minimum pulse duration is $\tau_{\mathrm{p}} \sim |2\pi K|^{-1}$. For $\tau_{\mathrm{p}} = 10$ ns, the required anharmonicity is $|K|/2\pi > 10$ MHz. These three conditions are satisfied by using $E_J/h \sim 15$ GHz and $E_C/h \sim 300$ MHz.

4.1.2 Cavity design

The qubit is embedded in a superconducting cavity, as shown in Fig. 4.3a. This system enables a narrow-band and efficient photon source for two reasons. First, the cavity protects the qubit from unintended interactions with the environment. As such, the qubit can have coherence times that are a hundred times longer than chip-based implementations[79, 179, 180]. Such long coherence

times are necessary in order to generate photons with high spectral purity[119]. Second, the cavity provides a well-controlled electromagnetic environment with low dissipation. This environment couples to a transmission line, thereby enabling single photons in the cavity to evolve into a mode that propagates in the transmission line as discussed in Section 2.4.

The geometry of the cavity determines its electromagnetic mode structure. For the idealized cavity depicted in Fig. 4.3, its geometry is essentially that of a rectangular waveguide shorted at both ends with two metal plates. This 'waveguide cavity' has mode frequencies given by

$$\frac{\omega_{\ell nm}}{2\pi} = c\pi\sqrt{\left(\frac{\ell}{L_x}\right)^2 + \left(\frac{m}{L_y}\right)^2 + \left(\frac{n}{L_z}\right)^2} \tag{4.11}$$

where $\ell, n, m \geq 0$ are integers for each mode and c is the speed of light[170, 151]. Although the cavity supports more than one mode, we couple the dipole moment of the qubit to the fundamental TE_{101} mode with $\ell, n = 1$ and $m = 0$. This coupling is maximized by placing the qubit in the center of the cavity[79]. For a cavity with $L_x = 50$ mm and $L_z = 25$ mm, the fundamental mode resonates at $\omega_{101}/2\pi \sim 7$ GHz. Because the transmon circuit perturbs the electromagnetic environment, finite element software packages are used to accurately predict the mode spectrum of the cavity[181].

Two ports provide access to the electromagnetic environment of the cavity[120]. In order to excite either the qubit or cavity, a weakly-coupled port delivers energy to the cavity at a rate of κ_2. The second port of the cavity is its output, which decays into a transmission line at a rate of $\kappa_2 \gg \kappa_1$. These two couping rates contribute to the total linewidth of the cavity $\kappa_\mathrm{c} = \kappa_0 + \kappa_1 + \kappa_2$ where κ_0 represents any undesired 'internal loss' in the cavity. In order to realize an efficient photon source, it is important minimize κ_1 and κ_0 because the probability that a cavity photon decays into the output port is set by $\kappa_2/\kappa_\mathrm{c}$. This ratio is the 'coupling efficiency' of the cavity.

The coupling rate for each port is set by two design constraints. First, the total linewidth of the cavity must be smaller than the bandwidth required to efficiently capture single photons using the electromechanical device. As discussed in Section 5.3, this bandwidth is $\lesssim 100$ kHz. Second, the internal loss of the cavity must be small compared to κ_2. For a rectangular cavity[1] cooled to

[1] The cavity was made out of 6061 aluminium alloy and it contained a qubit sample fabricated on a sapphire substrate.

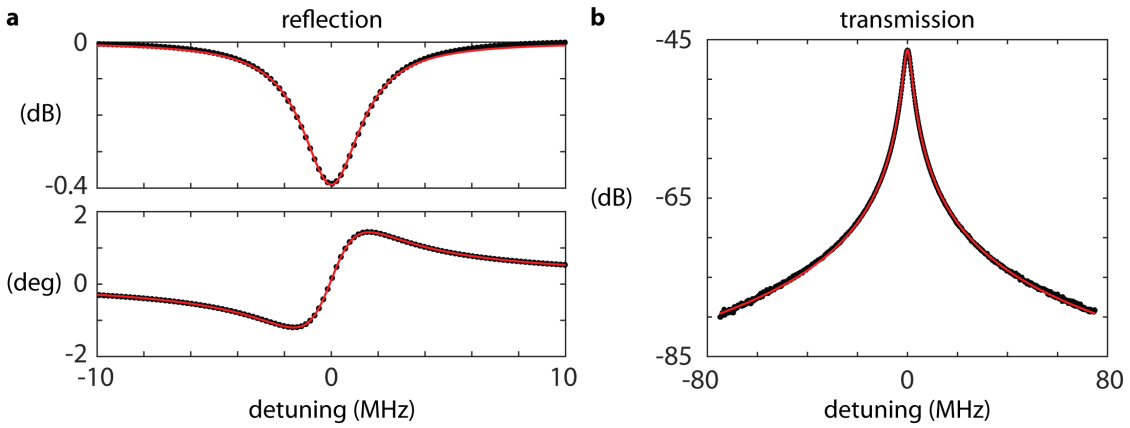

Figure 4.4: Cavity spectroscopy at room temperature. **a,** Measured cavity response of the strongly-coupled port in reflection. The cavity contains the chip with the transmon qubit. A fit (solid line) yields the total linewidth $\kappa_c/2\pi = 3.2$ MHz and the decay rate of the strongly-coupled port $\kappa_2/2\pi = 70$ kHz. The top plot shows the measured power and the bottom plot shows the measured phase response. **b,** Measured transmitted power. A fit (solid line) yields the total linewidth and $\kappa_1/2\pi = 600$ Hz with κ_2 determined in **a** held fixed.

less than 25 mK, we experimentally found that the internal loss rate ranges from approximately 5 kHz to 10 kHz. Given these constraints, we set κ_2 in the range of 50 kHz to 100 kHz. Because we cannot make the input coupling rate arbitrarily small, we set $\kappa_1 < 1$ kHz.

By injecting microwave power into the cavity and measuring its response at room temperature, we determine the coupling rate for each port. Initially, the reflected power off the strongly-coupled port of the cavity is measured. A fit to the amplitude and phase response yields κ_2 and κ_c. Next, the transmitted power through the cavity is measured. Knowing κ_2 and keeping it fixed during the fit yields κ_1 to within measurement error. Example measurements for this procedure are presented in Fig. 4.4.

4.1.3 Coupled qubit and cavity

The qubit couples to a single mode of the cavity. This system can be treated as two harmonic oscillators with a perturbation introduced by the transmon circuit[181]. The harmonic oscillator modes for the cavity and transmon circuit are described by a and b, which acquire their non-linearity from the fourth-order term in the expansion of the Josephson energy relation discussed in

section 4.1.1.1. By keeping terms up to fourth-order in δ, the Hamiltonian for the cQED system is

$$\frac{H}{\hbar} \approx \omega_{\mathrm{c}} a^{\dagger} a + \omega_{\mathrm{q}} b^{\dagger} b - \frac{K_{\mathrm{c}}}{2}(a^{\dagger} a)^2 - \frac{K_{\mathrm{q}}}{2}(b^{\dagger} b)^2 - 2\chi a^{\dagger} a b^{\dagger} b \tag{4.12}$$

where K_{c} (K_{q}) is the anharmonicity of the cavity (qubit) mode and χ is the 'cross-Kerr' interaction that causes a state dependent shift between the qubit and cavity mode[164].

In order to understand how the cross-Kerr interaction affects the cavity response, I write Eqn. 4.12 in terms of the Pauli spin operator σ_z. First, I restrict the transmon circuit to its ground and excited states by taking $b^{\dagger}|1\rangle = 0$ and neglecting terms with factors of $(b^{\dagger} b)^2$. In this truncated Hilbert space, the Pauli spin operate emerges as $b^{\dagger} b \rightarrow \sigma_z/2$. Second, I neglect terms with factors of $(a^{\dagger} a)^2$ because K_{c} is small compared to the linewidth of the cavity. Applying these substitutions to Eqn. 4.12 yields

$$\frac{H}{\hbar} = \omega_{\mathrm{q}} \frac{\sigma_z}{2} + (\omega_{\mathrm{c}} + \chi \sigma_z)\, a^{\dagger} a \tag{4.13}$$

where the terms have been rearranged so that its form is of the dispersive limit for the Jaynes-Cummings Hamiltonian[110, 116]. As pointed out in Section 2.3.2, the effective resonant frequency of the cavity is $\omega_{\mathrm{c}}^{i} = \omega_{\mathrm{c}} + \chi \sigma_z$ where $i = \{g, e\}$ is a function of the qubit in either its ground or excited states $|g\rangle$ and $|e\rangle$, respectively. Measuring this effective cavity resonance provides a way to characterize both the qubit and cavity.

4.2 Characterization of the qubit and cavity

Before we can operate the cQED system as a single-photon source, we first determine the cavity parameters discussed in Section 4.1.2 and the qubit parameters defined by Eqn. 4.13. We then calibrate a set of control pulses used to readout and control the qubit state. Lastly, we confirm that the coherence times of the qubit are sufficiently long for the photon generation protocol discussed in Section 4.3. The parameters for the cQED system are presented in Table 4.1.

Table 4.1: Parameters of the cQED system.

Symbol	Description	Value and units
$\omega_c/2\pi$	Cavity resonant frequency[a] (high power)	7.276 781 GHz
$\omega_g/2\pi$	Cavity resonant frequency[b] (qubit in ground state)	7.290 156 GHz
$\omega_e/2\pi$	Cavity resonant frequency[b] (qubit in excited state)	7.283 360 GHz
$\kappa_1/2\pi$	Weakly coupled cavity port decay rate	< 200 Hz
$\kappa_2/2\pi$	Strongly coupled cavity port decay rate[c]	50 kHz
$\kappa_c/2\pi$	Total cavity decay rate[c]	60 kHz
$\chi/2\pi$	Dispersive shift	-3.413 MHz
$\omega_{eg}/2\pi$	Ground to excited state transition frequency	5.652 MHz
$\omega_{sb}/2\pi$	Blue sideband transition frequency	2×6.462 GHz
$K_q/2\pi$	Qubit anharmonicity	380 MHz
T_1	Energy relaxation time	~ 60 μs
$T_2^\star$	Coherence time	~ 14 μs

[a] Measured at 10^4 fW (see Fig. 4.5a).
[b] Measured at 10^{-4} fW (see Fig. 4.5b).
[c] In this chapter, $\kappa_2/2\pi = 70$ kHz. For the experiment in Chapter 5, it was reduced to 50 kHz.

4.2.1 Cavity spectroscopy

Upon cooling down the cQED system, the nonlinearily of the qubit reveals itself in the power-dependent cavity response[182, 183]. To measure its response, we inject a pulsed probe tone into the weakly-coupled port of the cavity and monitor the transmitted amplitude from the output port. This scheme measures the scattering parameter $|S_{21}| = |V_2/V_1|$ where V_1 and V_2 are the amplitudes for the input and output voltage waves, respectively. To observe the nonlinear response of the cavity, we measure $|S_{21}|$ as a function of the probe power, as shown in Fig. 4.5a. At high powers, the transmission peaks are at the bare resonant frequency of the cavity $\omega_b/2\pi = 7.277$ GHz. As the probe power is reduced, the cavity response becomes highly nonlinear because of the dispersive interaction between the cavity and the qubit.

At low probe powers, the response is linear and it reveals the qubit state-dependent dispersive shift of the cavity. When the qubit is in its ground state $|g\rangle$, the transmission peaks at $\omega_c^g = \omega_c - \chi$ where $\omega_c^g/2\pi = 7.290$ GHz. There is faint transmission centered at $\omega_c^e/2\pi = 7.283$ GHz because of residual occupation of the qubit's excited state $|e\rangle$. One can determine the dispersive shift of the

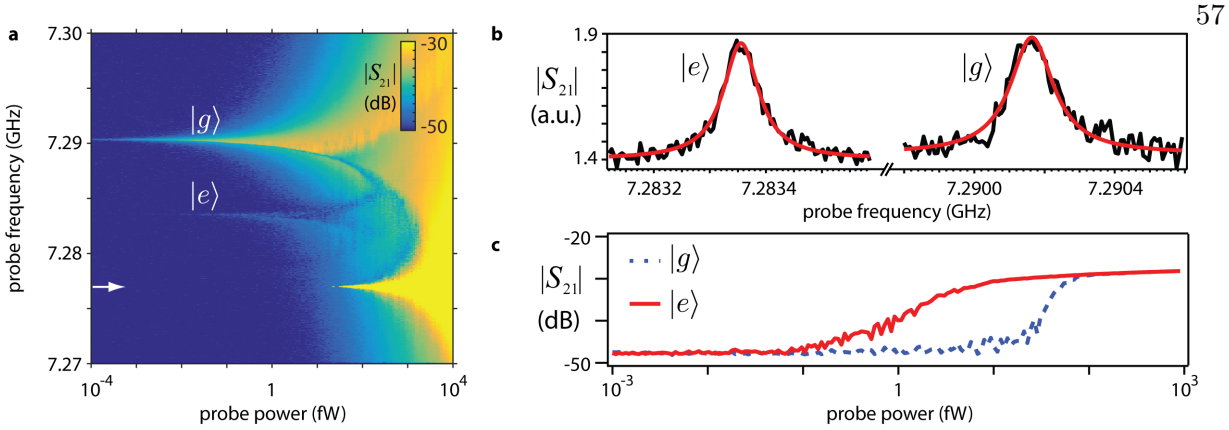

Figure 4.5: Cavity transmission as a function of probe power and frequency. **a,** The plot shows the measured cavity transmission (log magnitude) as a function of the probe frequency and power. The probe power is referenced to the input port of the cavity. At high probe power (> 10 fW), the response of the cavity is centered at its bare resonant frequency of $\omega_b/2\pi = 7.277$ GHz (indicated by the arrow). At low probe power ($< 10^{-3}$ fW), the cavity response is linear and it exhibits two peaks corresponding to the qubit in its ground and excited states $|g\rangle$ and $|e\rangle$, respectively. **b,** The plot shows the measured transmission at low power (at 10^{-4} fW) with the qubit prepared in either its $|g\rangle$ or $|e\rangle$ states. The solid line indicates a Lorentzian fit with a linewidth of $\kappa_c/2\pi = 80$ kHz. **c,** The plot shows a line cut of the cavity transmission at ω_b as the probe power is varied. When the probe power exceeds a sufficiently high power, the transmission exhibits a sharp jump that corresponds to the emergence of the bare cavity resonance. The onset of this sharp jump depends on the state of the qubit, which was initialized in either its $|g\rangle$ or $|e\rangle$ state.

cavity χ by taking $\omega_c^g - \omega_c^e = -2\chi$. For the data presented in Fig. 4.5b, the visibility of these two resonant features reveals that $\chi/2\pi = -3.5$ MHz. Additionally, by probing the low-power response of the cavity centered at ω_c^g, we determine its total linewidth $\kappa_c/2\pi = 80$ kHz and output port coupling rate $\kappa_c/2\pi = 70$ kHz. Having determined the parameters that characterize the response of the cavity, we can now exploit its nonlinear response to measure the qubit state.

4.2.2 Measuring the qubit state

In this thesis, we employ two qubit-state measurement schemes. The first scheme enables a simple and robust measurement protocol that can determine the qubit state with high fidelity[182]. For this scheme, a high-power tone probes the cavity state to destructively determine the qubit state. In contrast, the second scheme probes the linear response of the cavity at low powers and

can be used to project the qubit state via measurement[184, 185, 186].

In order to obtain a comparable signal-to-noise ratio using the low-power scheme, it requires a relatively low-noise amplifier. Such amplifiers using Josephson junction-based devices have been developed for qubit readout[187, 188, 189, 119]. However, integrating these amplifiers with the electromechanical device comes at the cost of additional complexity to the measurement protocol. We overcome this challenge by using the electromechanical device itself as a low-noise amplifier. This approach is unique to my experiment because it removes the complexity of the JPA and is readily integrable with the conversion experiment presented in Chapter 5.

4.2.2.1 High-power readout

The high-power readout scheme uses the nonlinear dispersive interaction to project the qubit state onto the classical state of the cavity. This approach effectively harnesses the cQED system an amplifier, and does not require the use of a subsequent low-noise amplifier such as the JPA. To infer the qubit state, a strong probe tone measures the cavity response in transmission[182]. The probe tone is centered at the bare resonant frequency of the cavity ω_{b}. When the power of the probe exceeds a critical value, the onset of a high-transmission 'bright state' emerges as shown in Fig. 4.5a.

Because the power level at which this onset occurs depends on the qubit state, this effect can be used to determine the initial state of the qubit as shown in Fig. 4.5c. To measure the qubit's state, one must choose a probe power that maximizes the difference in transmission for the two states. Crucially, the difference in transmission can be much larger than the noise in the detector used to measure the probe signal. While this readout scheme is relatively straight forward to implement, it is not a non-demolition measurement[2] because the high-power probe induces a substantial photon population in the cavity that drives the transmon qubit out of its $|g\rangle$ and $|e\rangle$ subspace. In order perform a non-demolition measurement of the qubit's state, one must use a low-power probe and a nearly quantum-limited amplifier to detect it[191].

[2] A non-demolition measurement leaves the qubit in a state that is unaffected by subsequent measurements[22, 190].

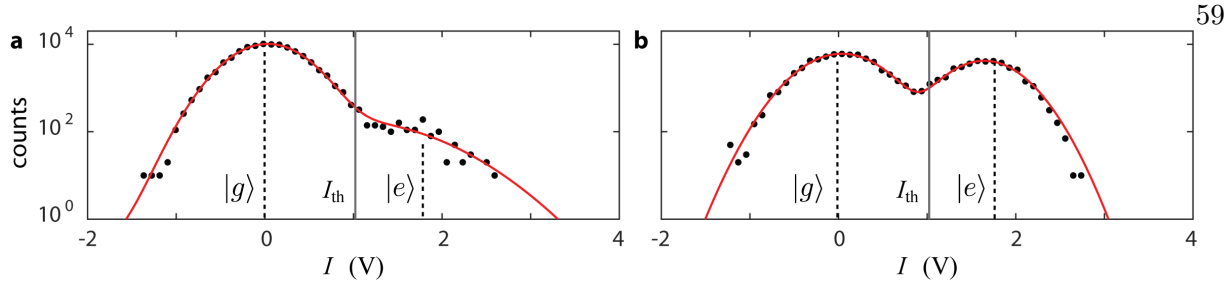

Figure 4.6: Histograms of single-shot measurements using the JPA. Each single-shot measurement outcome is the in-phase quadrature I of the transmitted probe signal through the cavity. The probe signal was pulsed on for 10 μs and it induced ~ 10 circulating photons in the cavity. **a,** The qubit was left in thermal equilibrium with the environment and its state was measured. The red solid line indicates a fit to a sum of two normal distributions, which reveals a residual excited state population of $P(e) = 2\%$. The gray solid line indicates the threshold $I_{\rm th}$ used to discern the two qubit states. **b,** When approximately half the qubit population is driven to its excited state $|e\rangle$, the separation between the two distributions becomes evident.

4.2.2.2 Low-power readout

The low-power readout scheme relies on the qubit state-dependent dispersive shift of the cavity. To infer the qubit state, a weak probe tone measures the cavity response in transmission[178, 192]. This response is probed by either measuring the amplitude or phase of the transmitted tone. Because my cQED system operates in the regime where the dispersive shift is $\chi \gg \kappa_c$, the ability to discern the qubit state is optimized by centering the probe frequency at the cavity's response and measuring the transmitted amplitude[193]. For example, consider centering the probe at $\omega_{\rm c}^e$. When the qubit's state is $|e\rangle$, the cavity response peaks at $\omega_{\rm c}^e$ and the probe will be transmitted. Conversely, when the qubit's state is $|g\rangle$, the cavity will be at $\omega_{\rm c}^g$ and the probe will not be transmitted. Thus, this scheme can discriminate the qubit states by probing the cavity response.

Employing a Josephson parametric amplifier (JPA) at the front end of the detector provides a way to perform efficient single-shot measurements of the qubit state. To access the single-shot regime, the measurement duration must be substantially shorter than the excited to ground state relaxation time of the qubit. The signal-to-noise of this measurement is determined by its duration, power level, the cavity bandwidth, and the detector efficiency[186]. Because the JPA enhances the detector efficiency, the measurement duration and power level can be significantly reduced and thus

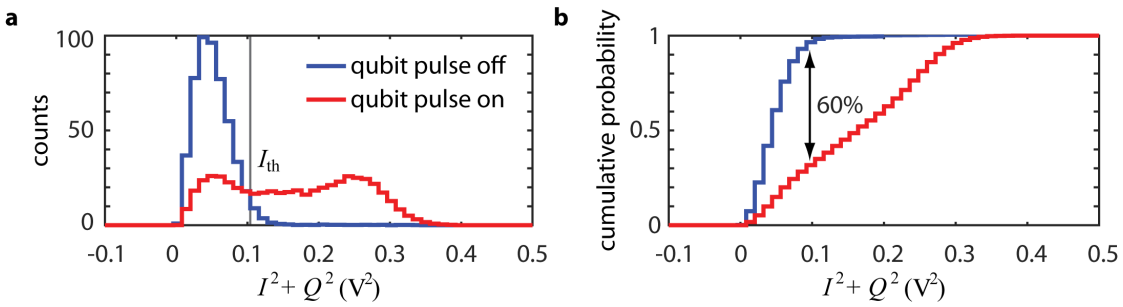

Figure 4.7: Single-shot measurements of the qubit state using the electromechanical device as an amplifier. Each single-shot measurement outcome is the magnitude squared I^2+Q^2 of the in-phase (I) and quadrature (Q) components of the transmitted probe signal through the cavity. **a,** The histogram shows the distribution of measurement outcomes when the qubit was either driven or not using a control pulse. The gray solid line indicates the threshold I_{th} used to discern the two qubit states. **b,** The plot of the cumulative probability indicates a readout contrast of 60% for discerning the qubit's two states.

enables single-shot high-fidelity qubit readout.

The ability to effectively discriminate between qubit states is quantified by collecting a repeated set of single-shot measurements. The outcome of each single-shot measurement is plotted in a histogram as shown in Fig. 4.6. Each outcome is the in-phase amplitude I of the transmitted probe through the cavity. If the probe is not transmitted, then $I = 0$. Thus, when the qubit state is $|g\rangle$, we expect a normal distribution of measurement outcomes centered at $I = 0$ as shown in Fig. 4.6a. However, when we drive approximately half the qubit population to the $|e\rangle$ state, an offset emerges because approximately half the measurement outcomes are from trials in which the probe was transmitted through the cavity. This case is shown in Fig. 4.6b. Because the two distributions are resolvable, we define a threshold I_{th} that separates the outcomes. If an outcome I is larger than I_{th}, we assign the outcome to the $|e\rangle$ state; conversely for $I < I_{\text{th}}$. This thresholding enables one to extract the probability that the qubit occupies its ground or excited states from a set of measurements.

Apart from using the JPA, low-power and single-shot measurements of the qubit state are enabled by harnessing the electromechanical device as an amplifier. The theory of operating it as an amplifier is discussed in Section 3.1.3. To readout the qubit state, we probe the response of the

cavity using pulsed signals as with the readout method using the JPA. However, in this case, we use the electromechanical device to amplify the readout pulse. We then collect a set of single-shot measurements and plot their outcomes in a histogram as shown in Fig. 4.7a. To quantify the ability to discern the qubit states, we calculate the maximum difference between the cumulative probability curves as shown in Fig. 4.7. This difference defines the readout contrast, which we calculate to be about 60%. This contrast level is comparable to what is obtained in the JPA-backed readout scheme using my cQED system.

4.2.3 Qubit characterization

The qubit readout methods discussed in the previous section enable characterization of the transmon qubit parameters summarized in Table 4.1. This section presents a characterization of the qubit's energy spectrum, control pulses used to alter its state, and its coherence times.

Energy spectrum

By employing either of the two qubit readout schemes presented in Section 4.2.2, we determine the anharmonicity K_q by measuring the qubit's spectrum. It is measured by driving the qubit with a control pulse, and then reading out the qubit state over a range of frequencies as shown in Fig. 4.8a. This qubit spectroscopy reveals two peaks centered at ω_{ge} and $\omega_{gf}/2$, which correspond to the $|g\rangle \rightarrow |e\rangle$ and $|g\rangle \rightarrow |f\rangle$ transitions. Because the anharmonicity is defined as $K_\mathrm{q} = \omega_{ge} - \omega_{ef}$ where ω_{ge}, it can be written as $K_\mathrm{q}/2 = \omega_{gf}/2 - \omega_{ge}$. The data in Fig. 4.8a shows that $K_\mathrm{q} = 380$ MHz. As discussed in Section 4.1.1.3, this amount of anharmonicity in the qubit spectrum is necessary in order to drive the qubit using fast (10 ns) control pulses.

Additionally, measuring the qubit spectrum provides information about the Josephson energy of the qubit. The Josephson energy E_J can be expressed in terms of transition frequencies by calculating the eigenenergies of the qubit spectrum using perturbation theory[171]. The result of this analysis yields

$$E_J \approx -\frac{1}{8}\frac{\omega_{ge}^2}{E_C} \tag{4.14}$$

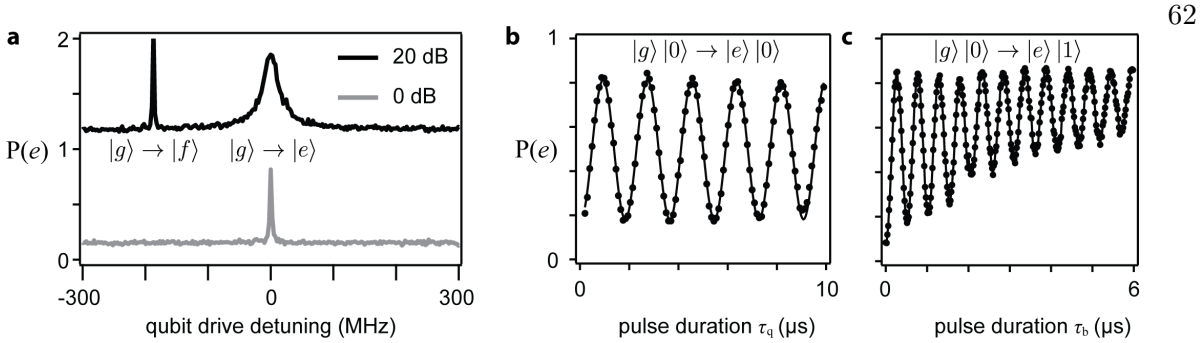

Figure 4.8: Calibration of the qubit control pulses. **a,** The plot shows the qubit excited state probability $P(e)$ as a function of the drive detuning. At low drive power, the qubit $|g\rangle \rightarrow |e\rangle$ transition is centered at ω_q. This power level is the reference (0 dB). At a higher drive power (20 dB), the qubit transition broadens and the $|g\rangle \rightarrow |f\rangle$ transition emerges centered at $\omega_{ef}/2$. These two frequencies are used to extract the anharmonicity K_q. **b,** When the qubit is driven at ω_q, the qubit population oscillates between the $|g\rangle$ and $|e\rangle$ states. **c,** Similarly, when the qubit is driven at $\omega_{bs}/2$, the qubit population oscillates as the cQED system oscillates between the $|g\rangle\,|0\rangle$ and $|e\rangle\,|1\rangle$ states.

where $E_C \approx -K_q$ is the charging energy. Using this result and the data presented in Fig. 4.8a, we calculate that $E_J \approx 14$ GHz. Thus, the spectrum reveals that the qubit is deep in the transmon regime with $E_J/E_C \sim 37 \gg 1$.

Calibrated control pulses

Having measured the qubit's spectrum, we calibrate the amplitude and duration of a pulsed tone used to control the qubit state. Specifically, these two parameters must be appropriately calibrated so that we can deterministically place the qubit in its excited state $|e\rangle$ or the superposition state $1/\sqrt{2}\left(|g\rangle + e^{i\varphi}\,|e\rangle\right)$ where φ is the phase of the qubit. To calibrate the control pulse, we first center the tone at ω_q. We then choose a fixed amplitude and vary its duration τ_q. As shown in Fig. 4.8b, the qubit population oscillates between its $|g\rangle$ and $|e\rangle$ states. These oscillations provide evidence that the qubit is indeed an addressable two-level system. By setting τ_q at half the first oscillation period, the qubit population can be driven from the $|g\rangle$ to $|e\rangle$ state. This calibration sequence realizes a 'π-pulse' because we can effectively rotate the qubit by an angle of $\theta = \pi$ on the Bloch sphere (see Section 2.2). Simply by adjusting the duration (or amplitude) of the pulse,

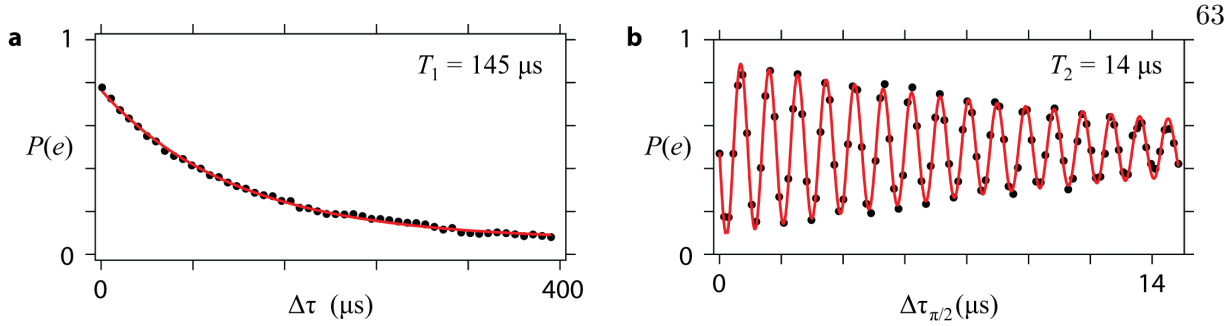

Figure 4.9: Time-domain measurements of the qubit coherence times. **a,** Measured probability $P(e)$ of the qubit excitated state $|e\rangle$ population as a function of delay time $\Delta\tau$ between a π pulse and a qubit measurement pulse. A fit to the data (solid line) yields $T_1 = 145 \pm 3$ μs. **b,** Similar to **a** but $P(e)$ is plotted as a function of the delay $\Delta\tau_{\pi/2}$ between two $\pi/2$ pulses. A fit to the data (solid line) yields $T_2 = 14 \pm 1$ μs.

we can rotate the qubit by $\theta = \pi/2$ thereby placing it in the superposition state where the pulse phase determines φ.

In order to generate single photons, we use a pulsed tone that can control the blue sideband transition $|g\rangle|0\rangle \rightarrow |e\rangle|1\rangle$ as introduced in Section 2.3.4. To deterministically place the qubit and cavity in the joint state $|e\rangle|1\rangle$, we must calibrate an appropriate control sequence. Because the blue sideband transition is driven via a two-photon process[118], we center the tone at half the frequency of the blue-sideband transition $\omega_{\rm bs}/2$. After the amplitude of the pulse is set, we vary its duration $\tau_{\rm b}$ and measure the qubit state as shown in Fig. 4.8c. The qubit population varies because the cQED system oscillates between the states $|g\rangle|0\rangle$ and $|e\rangle|1\rangle$. As $\tau_{\rm b}$ increases, photons decay out of the cavity at a rate of $\kappa_{\rm c}$ and so the oscillations saturate as the qubit settles to its $|e\rangle$ state as described in Ref. [118]. In order to create an effective π-pulse on this transition, we set $\tau_{\rm b}$ at half the first oscillation period. Using this calibrated pulse, the qubit can be put in the $|e\rangle|1\rangle$ thereby creating a single photon in the cavity.

To generate a superpostion of cavity photon states, we employ a two-step protocol[116, 121, 194]. In the first step, a $\pi/2$-pulse prepares the qubit and cavity in the superposition state $1/\sqrt{2}\left(|g\rangle|0\rangle + e^{i\varphi}|e\rangle|0\rangle\right)$. In the next step, a π-pulse on the blue-sideband transition swaps the population in the $|g\rangle|0\rangle$ and $|e\rangle|1\rangle$ states without affecting the population in the $|e\rangle|0\rangle$ state. The

qubit and cavity are now in the joint state $1/\sqrt{2}\left(|e\rangle|1\rangle + e^{i\varphi}|e\rangle|0\rangle\right)$. Because the $|e\rangle$ state can be factored out, the photon state is unentangled with the cavity. Thus, the cavity is prepared in the superposition state $1/\sqrt{2}\left(|0\rangle + e^{-i\varphi}|1\rangle\right)$ which decays out of the cavity into a propagating mode of the transmission line. In order to prepare this state, the protocol's duration must be substantially less than the qubit's coherence times.

Coherence times

We employ a two-step protocol to determine the qubit's relaxation time from the $|e\rangle$ to $|g\rangle$ states. This characteristic time is called T_1 and it describes energy loss of the qubit. In order to implement the photon generation protocol discussed in Section 4.3, the qubit's lifetime must satisfy $T_1 \gg \kappa_c^{-1}$. The protocol used to measure T_1 starts with preparing the qubit in its $|e\rangle$ state using a π-pulse. After a delay time of $\Delta\tau_\pi$, the qubit state is measured. By varying $\Delta\tau_\pi$, the qubit's excited state probability $P(e)$ decays as shown in Fig. 4.9a. A fit to the data[3] yields $T_1 = 145$ μs. Because of this relatively long decay time, care must be taken to ensure a wait time $> 5T_1$ between each execution of the protocol so that the qubit has time to relax to its $|g\rangle$ state with a probability that exceeds 99%.

In addition to determining the qubit's T_1 time, a three-step protocol is used to measure its dephasing time. This characteristic time is called $T_2^\star$ and it describes the random drift in the phase difference between the qubit states $|g\rangle$ and $|e\rangle$ in a superposition during an ensemble measurement. In order to generate coherent superposition states, the qubit's dephasing time must satisfy $T_2^\star \gg \tau_b$ where τ_b is the duration of the blue sideband pulse. The protocol used to measure $T_2^\star$ starts with preparing the qubit in the superposition state $1/\sqrt{2}\left(|g\rangle + e^{i\phi}|e\rangle\right)$ using a $\pi/2$-pulse. After a delay time of $\Delta\tau_{\pi/2}$, another $\pi/2$-pulse is applied to the qubit. By making repeated measurements of the qubit state as $\Delta\tau_{\pi/2}$ is varied, one finds that the qubit's excited state population oscillates

[3] For measurements on the same sample, the lowest relaxation time we measured was approximately 60 μs. Fluctuations in the T_1 time at the level of a factor of two have been well-documented[195], and may be explained by drifts in the quasiparticle density or occupation of two-level systems in the junction.

according to

$$P(e) \propto \cos\left(\Delta_{\mathrm{d}} \cdot \tau_{\pi/2}\right) \exp\left(-\tau_{\pi/2}/T_2^{\star}\right) \tag{4.15}$$

where $\Delta_{\mathrm{d}} = \omega_{\mathrm{q}} - \omega_{\mathrm{d}}$ is the detuning of the drive centered at ω_{d} from the qubit transition frequency.[4]

This method is commonly referred to as 'Ramsey interferometry' and is often the workhorse of precision spectroscopy experiments[196]. For the data presented in Fig. 4.9b, the fit to Eqn. 4.15 yields $T_2^{\star} = 14$ μs. This timescale is sufficient to prepare a superposition state using a $\pi/2$-pulse that is of order 100 ns in duration.

4.3 Generation of propagating single photons

In this section, we provide a rudimentary evaluation of the photon source. We demonstrate that the source efficiently generates single photons, and we show that their bandwidth is sufficiently narrow enough to be compatible with the electromechanical device.

4.3.1 Experimental apparatus

We create an experimental apparatus that enables the detection of propagating signals emitted from the cQED system. The main components of the apparatus are shown in Fig. 4.10. Qubit control and readout signals are injected into the weakly-coupled port of the cQED system. Its output port strongly couples to a transmission line that connects to a detector. The performance of the detector is characterized by two parameters: the efficiency η_{d} and gain G_{d}. The efficiency ranges from 0 (no measurement) to 1 (ideal measurement). The gain is a quantity that relates voltage fluctuations at the output of the detector to those at its input.

In order to efficiently measure single photons, the detector employs a Josephson parametric amplifier (JPA) as a sensitive preamplifier. We operate the JPA as homodyne detector in order to have the highest possible measurement efficiency, as pointed out in Section 2.5. Because we want to measure single photons emitted at the frequency $\omega_{\mathrm{c}}^{\mathrm{e}}$ when the qubit is in its excited state, we

[4] This expression assumes $T_2^{\star} \ll T_1$ as is the case in this thesis.

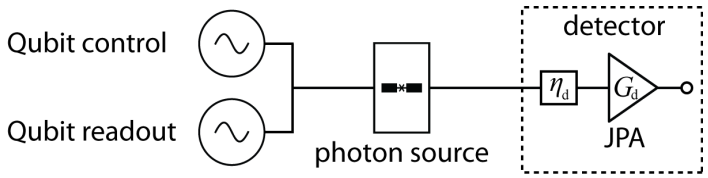

Figure 4.10: Diagram of the photon generation apparatus. Qubit control and measurement pulses are injected into the input of the photon source. The photon source consists of a cQED system. A Josephson parametric amplifier (JPA) serves as the sensitive preamplifier for the detector which has an efficiency η_d and gain G_d.

operate the JPA with its gain centered at ω_c^e. The output of the detector is demodulated and the voltage trace $V(t)$ is recorded.

The experimental apparatus presented in this section is similar to the one previously constructed in our lab[119]. However, we did not include a switch with a calibration noise source because of two reasons. First, we did not want to add any excess insertion loss between the cQED system and the detector, which would reduce the fidelity of the propagating single-photon state. Second, we want to avoid any stray infrared light that could enter in through the switch. Such light may degrade the coherence times of the qubit[197].

4.3.2 Generation and measurement protocol

We generate single photons by adapting a protocol developed previously in our lab[119]. This protocol creates a photon in the cavity by driving the blue-sideband transition $|g\rangle|0\rangle \rightarrow |e\rangle|1\rangle$ with a π-pulse as diagrammed in Fig. 4.11a. The cavity photon then evolves into a mode that propagates in the transmission line. For each repetition of the protocol, we measure a voltage trace $V(t)$ using the homodyne detector discussed in Section 4.3.1. For a control experiment, we execute the protocol but replace the π-pulse on the blue-sideband transition with a π-pulse on the qubit's transition. This sequence prepares the cQED system in the state $|e\rangle|0\rangle$ instead of $|e\rangle|1\rangle$. As such, the cQED system does not emit a photon.

To increase the photon generation fidelity, we measure and condition on the qubit's state[198]. Prior to generating a photon in the cavity, we measure the state of the qubit using a 'pre-select'

readout pulse. Because we want the cQED system to be initialized in the state $|g\rangle|0\rangle$, we select the measurements in which the qubit is in its $|g\rangle$ state. This selection removes approximately 10% of the measurement outcomes in which the qubit occupies its excited state. After generating a single photon in the cavity, the cQED system must be in the state $|e\rangle|1\rangle$ in order for the photon to be emitted at the excited state cavity frequency ω_c^e. Thus, we 'post-select' the data in which the qubit is in its $|g\rangle$ state. This selection removes approximately 60% of the measurement outcomes in which the qubit decays from its $|e\rangle$ to $|g\rangle$ state, or in instances when the blue-sideband transition is not driven because of infidelity in the π-pulse.

4.3.3 Quadrature amplitude extraction

In order to characterize propagating signals at the single-photon level, we express measured signals in terms of photons per second, or quanta, referred to the input of the detector. For each voltage trace $V(t)$ measured at the detector, we extract a single quadrature amplitude X. This quadrature amplitude describes one particular mode of the propagating signal measured at the detector. To define a particular mode, we use a mode-matching function $f(t)$ that weights each $V(t)$ in order to produce an optimum estimate of the quadrature amplitude[121]. We choose $f(t)$ so that it matches the temporal envelope of the photon signal measured at the detector. Specifically, the form of $f(t)$ depends on the bandwidth of the emitted single-photon signal (set by the cavity linewidth of the cQED system) and the bandwidth of the detector (set by the JPA). As such, we use a function defined by

$$f(t) = h(\omega_{\mathrm{LPF}}, t) \star \begin{cases} 0 & t \leq t_0 \\ 1 - e^{-\kappa(t-t_0)/2} & t_0 < t \leq T_{\mathrm{bs}} \\ e^{-\kappa(t-t_0)/2} & t > T_{\mathrm{bs}} \end{cases} \tag{4.16}$$

where $\star$ denotes a convolution operation, h is the finite impulse response function of a low-pass filter, ω_{LPF} is the cutoff frequency of the low-pass filter, t_0 is the start time of the blue-sideband pulse, T_{bs} is its duration, and κ is the power decay rate of the signal. For the bandwidth of the low-pass filter, we choose it to be $\omega_{\mathrm{LPF}} = \kappa_{\mathrm{JPA}}/2$, where κ_{JPA} is the bandwidth the JPA. A plot

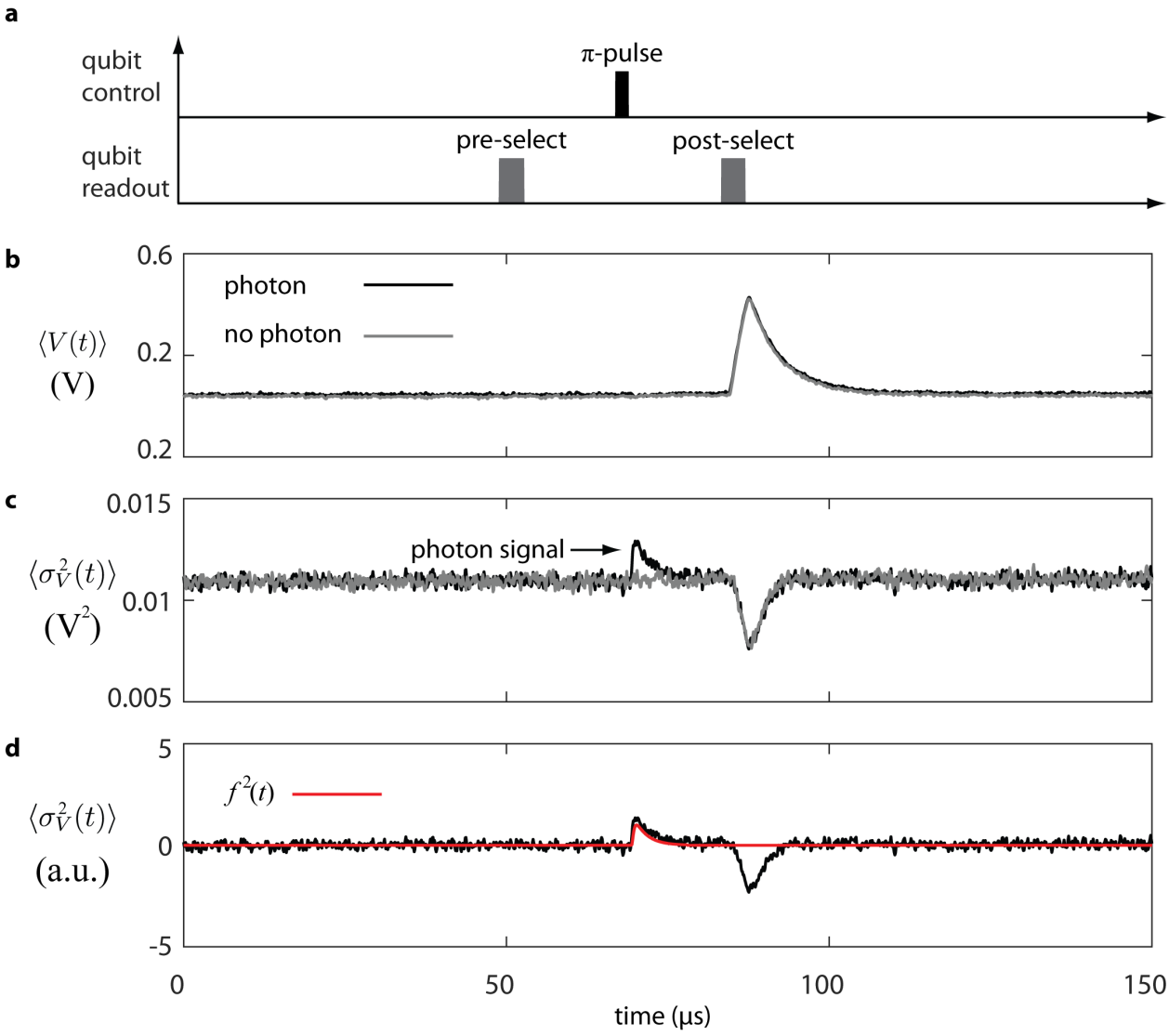

Figure 4.11: Photon generation and detection. **a,** A timing diagram depicts the protocol used to generate propagating photons. The π-pulse (black) at time $t \approx 70$ μs either generates a photon or excites the qubit for the reference vacuum measurement. Qubit readout pulses (pre-select and post-select) are used to condition the measurement on the qubit state. **b,** Measured voltage signals $\langle V(t) \rangle$ at the detector averaged over 4,798 individual time traces with the π-pulse frequency either at the blue sideband transition frequency (black) or the qubit's frequency (gray). **c,** The plot is similar to **b** but for the voltage variance of the time traces. **d,** The plot shows the filter function $f(t)$ used to extract the quadrature amplitude for each time trace. The filter function has a power decay rate of 83 kHz.

of the mode-matching function is shown in Fig. 4.11d in which we used $\kappa_{\mathrm{JPA}}/2\pi = 2$ MHz and $T_{\mathrm{bs}} = 250$ ns.

After determining $f(t)$, we calculate the quadrature amplitude for a given voltage trace using the method of least-squares parameter estimation[199], where the parameters to be estimated are the amplitude, V_{q}, of $f(t)$ and the amplitude, V_{dc}, of the background windowing function $b(t)$. We use a background function to account for the offset in each $V(t)$ that drifts during the acquisition of a complete data set. The function $b(t)$ is a piecewise-constant function that is non-zero during the photon generation protocol except when the qubit state is measured. To obtain these two parameters from each discretized voltage trace $\{V_k\}$ (containing N samples), we minimize the cost function

$$C = \sum_{k=1}^{N} \left[V_k - (V_{\mathrm{q}} f_k + b_k V_{\mathrm{dc}})\right]^2 \tag{4.17}$$

with respect to V_{q} and V_{dc}. The result of this minimization yeilds

$$V_{\mathrm{q}} = \sum_{k=1}^{N} V_k \cdot f_k - \left(\sum_{\ell=1}^{N} V_\ell \cdot b_\ell\right) \cdot \left(\sum_{m=1}^{N} b_m \cdot f_m\right) \tag{4.18}$$

where f_k and b_k are discretized versions of the mode-matching and background functions, respectively. Eqn. 4.18 yields an uncalibrated quadrature amplitude for each measured voltage trace.

To calibrate the set of quadrature amplitudes, we execute the control sequence in which no photons are generated. This calibration assumes the convention that one quadrature of a signal in the vacuum state has a variance of $\mathrm{Var}(X) = 1/4$ quanta as discussed in Section 2.1.3. The uncalibrated quadrature amplitudes are binned in a histogram, and this data is fit to a normal distribution with the gain G_{d} of the measurement apparatus as the only free parameter. The center of the distribution is zero, and its variance is set to be 1/4 for a vacuum state. We use the gain determined from the fit to scale the quadrature amplitudes obtained when photons were generated. The calibrated quadrature amplitudes are presented in Fig. 4.12.

4.3.4 Density matrix reconstruction

To characterize the quantum state emitted from the photon source, we reconstruct the state's density matrix ρ. The density matrix provides a complete description of the state by taking into account both quantum and statistical uncertainty in the measurement. In the number basis, the matrix element ρ_{nn} conveniently describes the probability of detecting n photons. For an ideal single-photon state, $\rho_{11} = 1$ with all other elements equal to zero. However, imperfections in the generation and measurement process yield $\rho_{11} < 1$.

We estimate ρ by performing a microwave version of homodyne tomography, as discussed in Section 2.5. This procedure relies on making an ensemble of repeated single-quadrature measurements on a set of identically-prepared quantum states emitted from the photon source. For each measurement, the outcome is plotted in a histogram. Because we measure in the quadrature basis, we expect the data to follow the marginal distribution

$$\Pr(X) = \langle X| \rho |X\rangle . \tag{4.19}$$

In the photon-number basis, the density matrix is given by

$$\rho = \sum_n P_n |n\rangle \langle n| \tag{4.20}$$

where $P_n = \rho_{nn}$ is the probability to be in the state $|n\rangle$ for an integer $n \geq 0$. This form of ρ enables Eqn. 4.19 to be written in the number basis:

$$\Pr(X) = \sum_n \rho_{nn} |\langle X|n\rangle|^2 . \tag{4.21}$$

By calculating the eigenstates of the quantum harmonic oscillator in the quadrature basis, one finds

$$\langle X|n\rangle = \frac{1}{\sqrt{2^n n!}} \left(\frac{2}{\pi}\right)^{1/4} e^{-X^2} H_n(\sqrt{2}X) \tag{4.22}$$

where H_n are the Hermite polynomials[101].

After we generate a histogram of the calibrated quadrature amplitudes, we perform a fit using Eqn. 4.21 in a three-photon number basis. Without conditioning on the qubit state, the fit

to the marginal distribution yields $\rho_{00} = 0.61 \pm 0.01$, $\rho_{11} = 0.36 \pm 0.02$, and $\rho_{22} = 0.02 \pm 0.02$ (the ρ_{33} element is indistinguishable from statistical noise). In order to increase the single photon generation efficiency, we condition on the state of the qubit. This conditioning purifies the state because we discard measurements in which we expect no photon to be generated. For this case, the results of the fit yield $\rho_{00} = 0.48 \pm 0.01$, $\rho_{11} = 0.49 \pm 0.01$, and $\rho_{22} = 0.03 \pm 0.02$. A histogram of the measured quadrature amplitudes is shown in Fig. 4.12.

We model the measured state by taking into account two sources of infidelity. First, because the cavity has internal loss, the probability of a photon decaying out of the port coupled to the transmission line is $\eta_c = \kappa_2/\kappa_c = 0.87 \pm 0.03$. Second, the detector has an efficiency that is not ideal. In a separate cooldown of the apparatus, we used a calibrated noise source and found that this detector has $\eta_d = 0.60 \pm 0.02$. Using these two parameters, we model the expected state as

$$\rho_m = (1 - \eta_c\eta_d) \left|0\right\rangle \left\langle 0\right| + \eta_c\eta_d \left|1\right\rangle \left\langle 1\right| \tag{4.23}$$

which is a statistical mixture of a pure vacuum and single-photon state[194]. This model predicts $\rho_{11} = 0.52 \pm 0.02$ which is in reasonable agreement with what is measured.

The results in this section show that the cQED system can generate propagating single photons efficiently and with a narrow bandwidth. As such, the next step is to interface the cQED system with the electromechanical device discussed in Chapter 3.

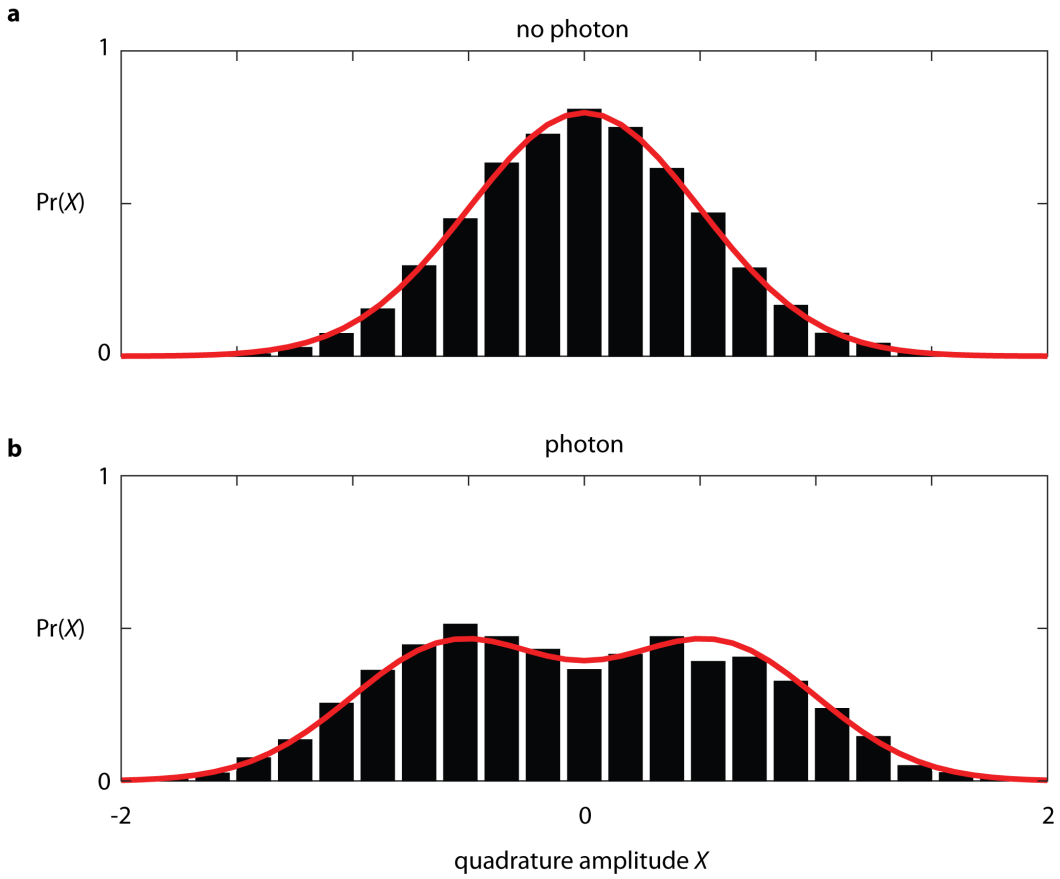

Figure 4.12: Histograms of measured quadrature amplitudes for single photons. The plots show the plotted probability distribution $\Pr(X)$ as a function of quadrature amplitude X scaled in units of $\sqrt{\text{quanta}}$. The solid line indicates a fit to expected distribution for a diagonal density matrix with a three-photon Fock basis. **a,** Control experiment ('no photon') in which no photons were generated. The solid line is a normal distribution with a variance of $\text{Var}(X) = 1/4$. **b,** Experiment ('photon') in which photons were generated. A fit to the measured distribution yields the diagonal density matrix elements $\rho_{00} = 0.48 \pm 0.01$, $\rho_{11} = 0.49 \pm 0.01$, and $\rho_{22} = 0.03 \pm 0.02$.

Chapter 5

Conversion of propagating single photons to mechanical motion

An electromechanical device converts the state of a propagating microwave field to mechanical motion, as pointed out in Chapter 3. By using the single-photon source presented in Chapter 4, the field can be prepared in a superposition of zero and one photons that encodes a quantum bit (qubit) of information. In this chapter, I combine these two capabilities and demonstrate that the electromechanical device can capture a state that encodes quantum information. Once captured, it can be mechanically stored for over a hundred microseconds and then retrieved on-demand. In order to measure the state of the input field or mechanical resonator, I exploit the electromechanical device as a nearly quantum-limited amplifier as described in Chapter 3. Using this capability, I characterize the capture process and find that it can preserve the information contained in an arbitrary qubit better than what is possible using only classical resources.

This chapter describes the experimental results of converting propagating single photons to mechanical motion. Section 5.1 describes the experimental apparatus. Section 5.2 demonstrates that the electromechanical device can function as a low-noise amplifier. Section 5.3 presents two protocols used to characterize the conversion process from propagating microwave fields to mechanical motion. Section 5.4 demonstrates the ability to capture, store, and amplify single photons. Section 5.5 presents the conversion of qubits and a characterization of the capture process.

5.1 Experimental apparatus

The electromechanical device interfaces with a single-photon source through a network of microwave-frequency components. The main components of the network are shown in Fig. 5.1a, and a picture of the experimental apparatus is shown in Fig. 5.2. Microwave pumps and test signals are injected into the network using a directional coupler (the microwave equivalent of a beamsplitter), and the photon source is pumped via a separate port. The photon source consists of the cQED system discussed in Chapter 4. This source emits a signal that is routed to the electromechaincal device using a circulator, which also provides a sufficient level of isolation to protect the cQED system from the strong pumps used to control the electromechanical device (see Section 3.1.1). After the signal interacts with the electromechanical device, it is routed to a detector. Once detected, the signal is downconverted in frequency with a demodulation mixer and then digitized. Data collected consist of digitized voltage waveforms $V(t)$. Detailed descriptions of the detector and remaining components of the measurement network are presented in Appendix A.

A simplified frequency-domain representation of the experiment is shown in Fig. 5.1c. The photon source emits a signal centered at $\omega_{\mathrm{c}}^{\mathrm{e}}$ when the qubit occupies its excited state. To capture the propagating signal at this fixed frequency, the electromechanical device is tuned into precise resonance with $\omega_{\mathrm{c}}^{\mathrm{e}}$ using a voltage bias V_{dc}. This bias is applied to a separate port of the electromechanical device as shown in Fig. 5.1b and as discussed in Section 3.1.4. To create either the beamsplitter or two-mode squeezer interactions discussed in Section 3.1.1, microwave pumps are applied below and above the center frequency ω_{LC} of the electromechanical device by the mechanical resonant frequency ω_{m}.

5.1.1 Sub-optimal capture of single photons

As an initial test of the beamsplitter interaction between a single photon and the mechanical resonator, we implement the two protocols diagrammed in Fig. 5.3. Both of these protocols employ the red-detuned pump to capture a propagating field. For the protocol diagrammed in Fig. 5.3a,

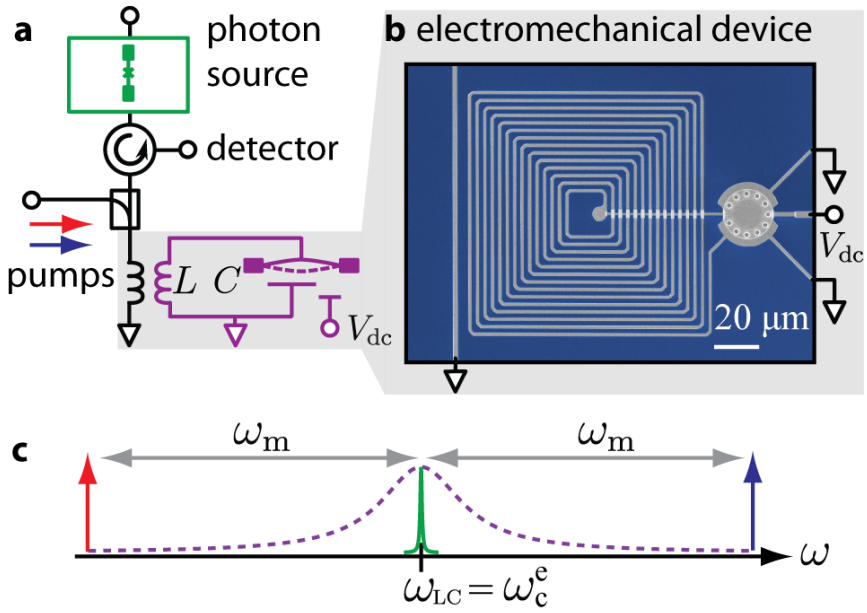

Figure 5.1: Diagram of the experiment. **a,** A simplified schematic shows the electromechanical device connected to a photon source consisting of a transmon qubit in a microwave cavity. Pumps (arrows) used to create the capture (red) and amplification (blue) interactions are injected into the transmission line. **b,** False-color micrograph of the electromechanical device where aluminium films (gray) are deposited on a sapphire substrate (blue). The spiral forms the inductor and the disc is the mechanically-compliant capacitor. Micrograph acquired with assistance from Paul Blanchard at NIST. **c,** Pumps are detuned below and above the LC circuit's resonant frequency ω_{LC} by the mechanical resonant frequency ω_m. Using a voltage bias V_{dc}, the LC circuit's resonant response (dashed magenta) is tuned to match the much narrower resonance of the microwave cavity (green solid) at the frequency ω_c^e.

the propagating field consists of a large-amplitude test signal generated by a microwave synthesizer (see Appendix A.4). Importantly, we tailor this test signal to have spectral and temporal content similar to that of a single-photon signal emitted from the cQED system. Such a signal has a center frequency given by ω_{LC} and a temporal envelope of the form

$$b_{in}(t) \propto \Theta(t) e^{-\kappa_c t/2} \tag{5.1}$$

where κ_c is the bandwidth of the cQED system and $\Theta(t)$ is the Heaviside step function. Because the red-detuned pump is not optimally shaped to capture a decaying signal (see Section 3.1.2.1), the efficiency of the capture process is sub-optimal. For the protocol diagrammed in Fig. 5.3b, no large-amplitude test signal is employed. Instead, a single photon is generated by driving the qubit's

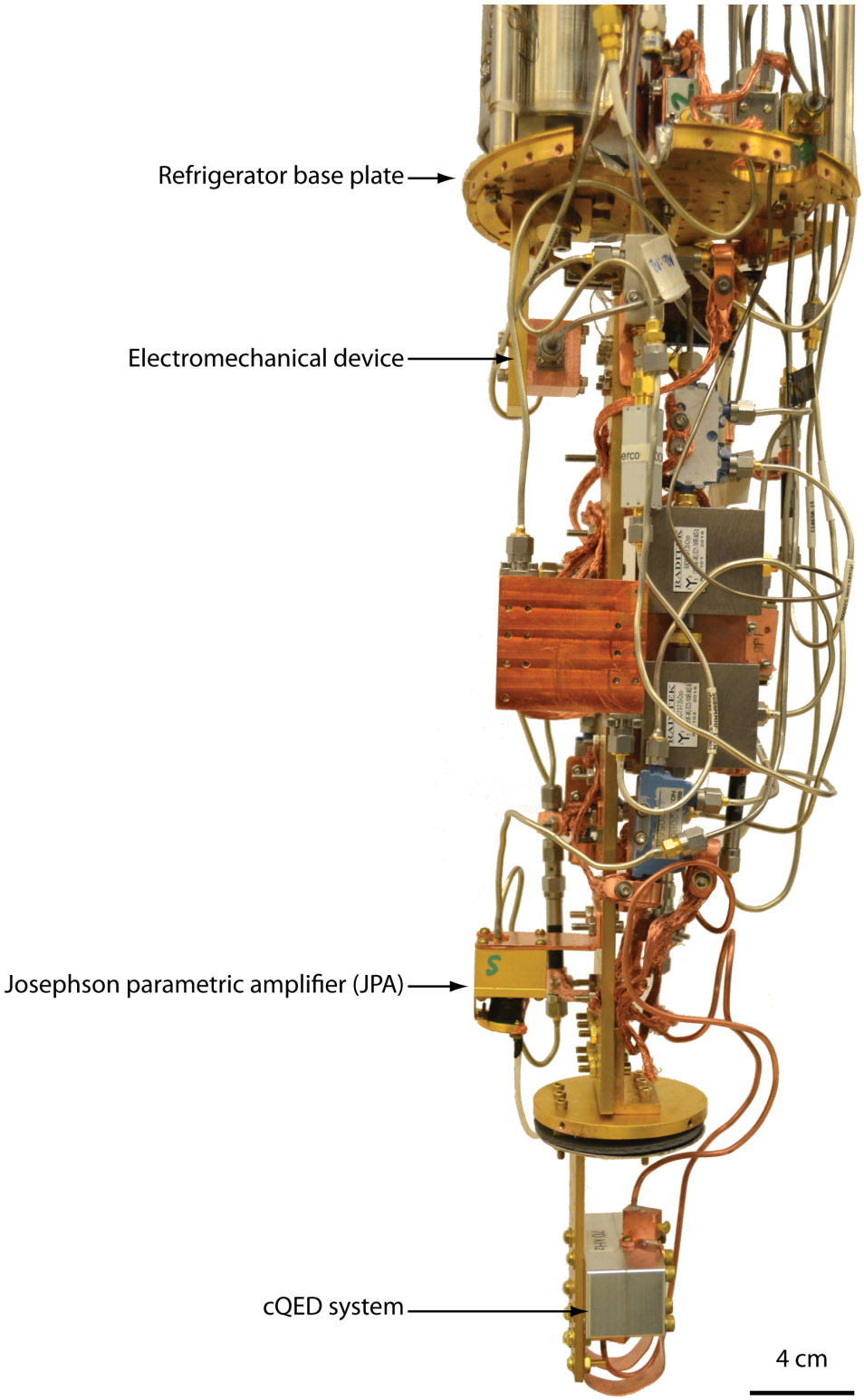

Figure 5.2: Picture of the experiment. It is mounted to the based stage of a dilution refrigerator that provides an environment temperature of $T_{\mathrm{env}} < 25$ mK. The magnetic shield for the cQED system is not shown.

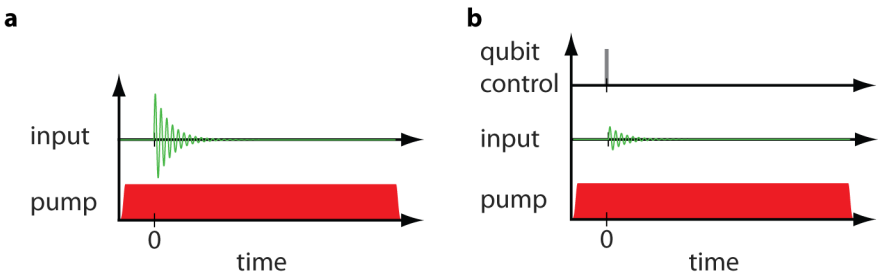

Figure 5.3: Initial capture protocol. **a,** The timing diagram depicts the protocol used to capture a large-amplitude coherent input test signal (green). A constant red-detuned pump is on during the entire duration of the protocol (bottom). **b,** The diagram depicts a protocol similar to the one in **a** but without employing the test signal. Instead, a qubit control pump drives the blue sideband transition in order to generate a single photon.

$|g\rangle\,|0\rangle \rightarrow |e\rangle\,|1\rangle$ transition using a π-pulse, as discussed in Section 2.3.4.

Conversion results for both a large-amplitude test signal and a single photon are presented in Fig. 5.4. For the experiment in which the test signal is employed, we measure an average voltage trace at the detector as shown in Fig. 5.4a. When the pump's detuning is $\Delta_{\rm r} = -0.1\omega_{\rm m}$ the propagating signal is not captured. Instead, it is captured when $\Delta_{\rm r} = -\omega_{\rm m}$ but with an efficiency of less than 50%. (This sub-optimal capture is remedied in Section 5.3.) To model the sub-optimal capture, we numerically integrate Eqns. 3.6. Using the parameters outlined in Table 3.1, we find good agreement with the model and data. For the experiment in which a single photon is employed, we measure the variance of voltage traces as shown in Fig. 5.4b. The response is similar to that of the test case with a large-amplitude signal, indicating partial capture of a single photon. Additionally, this initial capture experiment reveals that the strong, red-detuned pump adversely affects the detector (discussed in Appendix A.6). To circumvent this problem, we developed a way to operate the electromechanical device as an efficient pre-amplifier for the detector.

5.2 Electromechanical device as a low-noise amplifier

Signals at the single-photon level can be efficiently measured by operating the electromechanical device as a low-noise amplifier. A description of how it functions as an amplifier is discussed

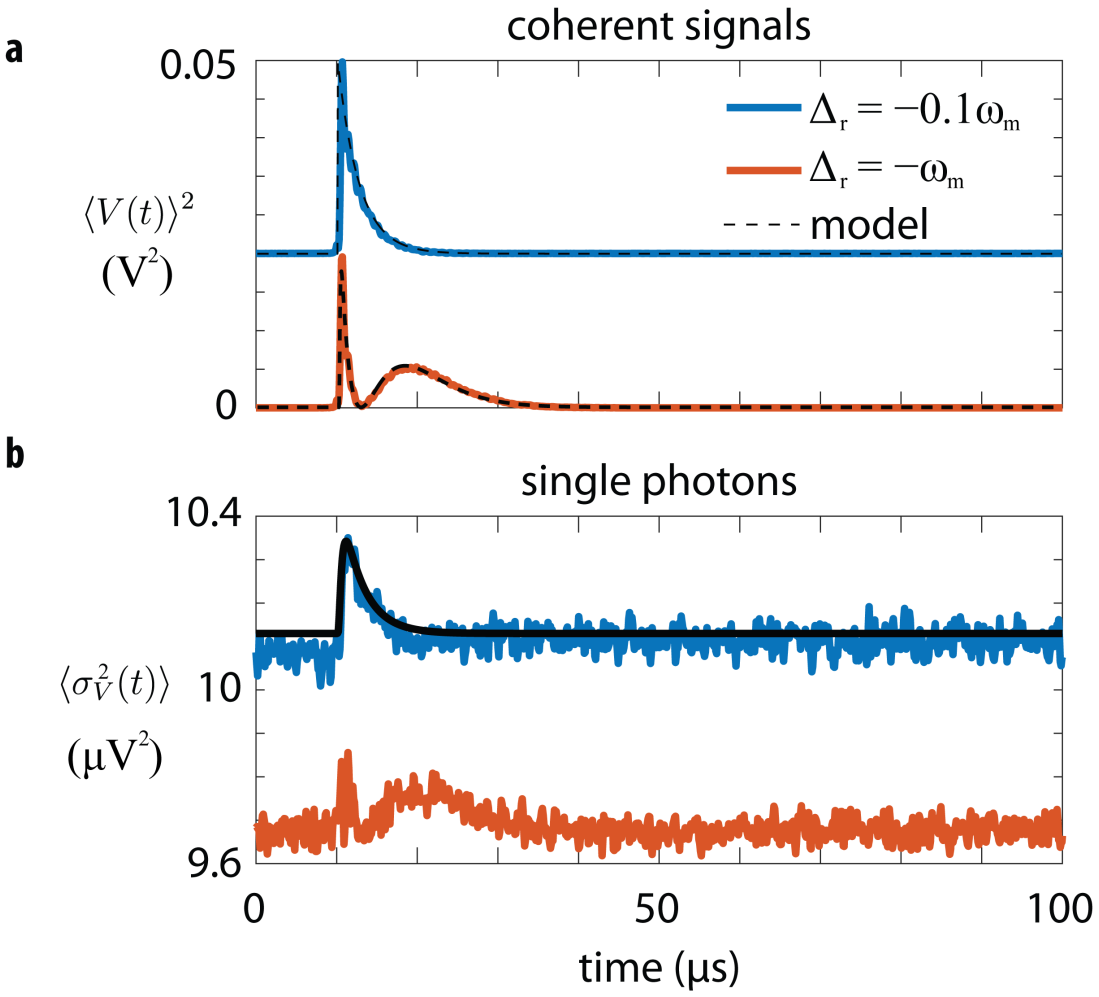

Figure 5.4: Sub-optimal capture of propagating coherent signals and single photons. **a,** The plot shows voltage signals $V(t)$ measured at the detector averaged over 102,400 repetitions of each protocol. Large amplitude ($> 10^6$ photons/sec) coherent signals with a power decay rate of 60 kHz are injected into the electromechanical device. A constant red-detuned pump is also injected into the electromechanical device. The strength of the pump is $\Gamma_r/2\pi \approx 60$ kHz. The top curve (blue) was acquired when the capture pump was at a detuning of $\Delta_r = -0.1\omega_m$ where ω_m is the mechanical resonant frequency. The bottom curve (orange) was acquired when the capture pump was red-detuned at $\Delta_r = -\omega_m$, the decaying signal is captured with a sub-optimal efficiency. The dotted line corresponds to the expected behavior using independently measured parameters for the electromechanical device. **b,** Propagating single photons were generated using the cQED system and routed to the device. The plot shows the measured voltage variance $\sigma_V^2(t)$ averaged over 819,200 repetitions of each protocol. Top and bottom curves were acquired under similar conditions to those in **a**. Note: an arbitrary offset is applied to the top curves (blue) in each plot in order to display them on the same plot as the bottom curves (orange).

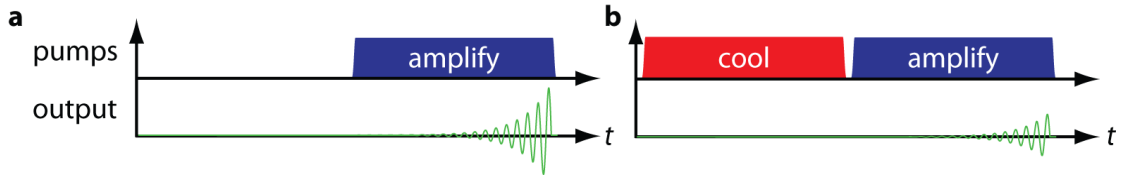

Figure 5.5: Protocols used to amplify thermal states of mechanical motion. **a,** The mechanical resonator is left in thermal equilibrium with its environment prior to pulsing on the blue-detuned amplification pump. A signal with a rising temporal envelope emerges from the electromechanical device. **b,** A red-detuned pump cools the motion of the mechanical resonator. When the blue-detuned pump pulses on, a signal with a rising temporal envelope emerges from the electromechanical device. The amplitude of the emitted signal is smaller than the amplitude in **a** because the resonator was cooled, and so it started with an occupation near its ground state.

in Section 3.1.3. In this section, we demonstrate that the electromechanical device can amplify thermal states, and that its noise performance approaches the quantum limit[126].

5.2.1 Amplification of thermal states

As a first test of the electromechanical device's performance as an amplifier, we use it to amplify thermal states of mechanical motion. By measuring thermal states of two different temperatures, we can determine the mechanical resonator's occupation n_{th} after it is cooled. This approach is analogous to a Y-factor measurement[151] used to determine the noise temperature of an amplifier by measuring Johnson noise emitted from a resistor held at two or more known temperatures. For the electromechanical amplifier, we can either cool the motion of the resonator or leave it in equilibrium with the environment.

In the first set of measurements, we execute the protocol shown in Fig. 5.5a. For this protocol, the mechanical resonator is left in thermal equilibrium with its environment for a duration of at least $30/\kappa_{\mathrm{m}}$ where κ_{m} is the mechanical resonator's linewidth. We then pulse on a blue-detuned pump to both amplify the state of the resonator and convert it into a propagating microwave field. The detector measures this output field, which we express in terms of its quadrature amplitudes X and Y (see Section 5.3.2). These amplitudes have a total variance described by $\mathrm{Var}(S_{\mathrm{h}})$ where the sub-script denotes 'hot' because the resonator was not cooled using the red-detuned pump.

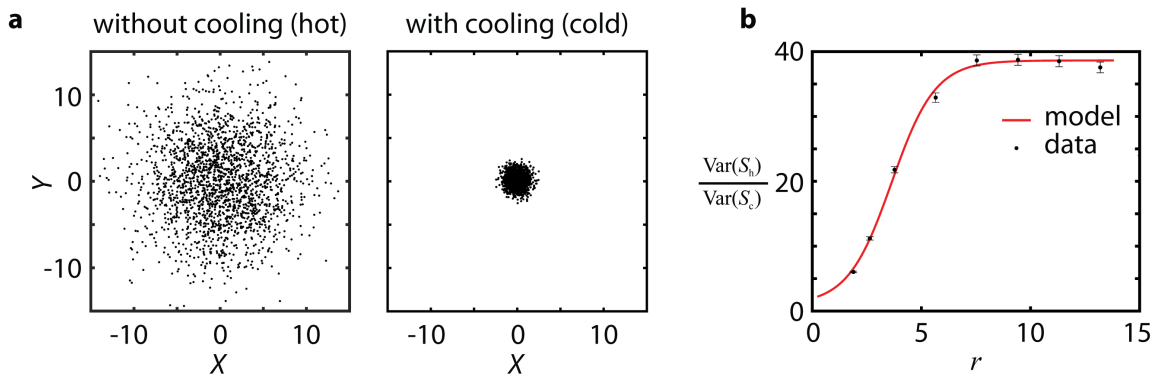

Figure 5.6: Amplified thermal states. **a,** The figure shows scatter plots of measured quadrature amplitudes $S = X + iY$ of signals at the detector where S is in units of $\sqrt{\text{quanta}}$. Without cooling the mechanical mode, the thermal motion of the mechanical resonator is amplified while the blue-detuned pump is pulsed on. The quadrature amplitudes (S_h, hot) are shown in the 'without cooling' plot. Cooling the mechanical mode results in a reduced scatter in the quadrature amplitudes (S_c, cold) as shown in the 'with cooling' plot. **b,** The plot shows the ratios of the total variance of the quadrature amplitudes without cooling, $\text{Var}(S_\text{h})$, and with cooling, $\text{Var}(S_\text{c})$, as $r = \Gamma_\text{b}\tau_\text{b}$ was varied. For these measurements, $\Gamma_\text{b}/2\pi = 60$ kHz while τ_b was varied from 5 μs to 55 μs. Once $r \gg 1$, the plotted ratio approaches the expression given by Eqn. 5.2. Error bars correspond to the statistical uncertainty in estimating the variance of 2,048 measurements.

In the second set of measurements, we execute the protocol shown in Fig. 5.5b. For this protocol, we cool the mechanical resonator to nearly its quantum ground state by using the red-detuned pump. We then turn on the amplification interaction and measured signals at the detector. For these measurements, we obtain a total variance $\text{Var}(S_\text{c})$ where the sub-script denotes 'cold' because the resonator was cooled using the red-detuned pump. Once $r \gg 1$, the ratio of the variances approaches

$$\frac{\text{Var}(S_\text{h})}{\text{Var}(S_\text{c})} = \frac{n_\text{m} + 1}{n_\text{th} + 1}. \tag{5.2}$$

If the mechanical mode is ideally in its ground state, then $n_\text{th} = 0$ and Eqn. 5.2 yields $n_\text{m} + 1$ where n_m is the mechanical resonator's equilibrium occupation that is discussed in Section 3.2.2. We observe that the ratio in Eqn. 5.2 is slightly reduced from $n_\text{m} + 1$ as shown in Fig. 5.6. We attribute this reduction to a small residual occupation in the mechanical mode that is $n_\text{th} = 0.09 \pm 0.01$ quanta. Such a low occupation enables the electromechanical device to function as a nearly quantum-limited amplifier.

5.3 Two protocols used to characterize the capture process

Exploiting the electromechanical device as an amplifier enables characterization of the capture *process*. Because the process maps states of fields at the input of the electromechanical device to the resonator, we must determine the input state and compare it to the captured state. To this end, we have developed 'calibration' and 'capture' protocols that are used to determine the input and captured states, respectively. Timing diagrams of the protocols is presented in Fig. 5.7a.

The two protocols are initially tested with coherent signals whose center frequency and bandwidth are chosen to match those created by the cQED system, as shown in Fig. 5.7b. To optimally capture the input field, the red-detuned pump is modulated as prescribed by Eqn. 3.15. For a field with a decaying temporal envelope of the form given by Eqn. 5.1, optimally capturing it requires

$$\Gamma_{\mathrm{r}}(t) = \frac{\gamma e^{-\gamma t}}{1 - e^{-\gamma t} + \gamma/\Gamma_{\mathrm{r}}(0)}\Theta(t) \tag{5.3}$$

where γ is the power decay rate of the signal to be captured and $\Gamma_{\mathrm{r}}(0)$ is the coupling rate at $t = 0$. For a high capture efficiency, $\Gamma_{\mathrm{r}}(0) \gg \gamma$. As discussed in Section 3.1.2.1, the maximum attainable coupling rate is limited by the circuit's bandwidth $\Gamma_{\mathrm{r}}(t) < \kappa_{\mathrm{LC}}$. For our system, the decaying signal has $\gamma/2\pi = 60$ kHz, and $\Gamma_{\mathrm{r}}(0)/2\pi \approx 1$ MHz. Using these parameters, we optimally capture signals with decaying temporal content. For the data presented in the lowest plot in Fig. 5.7, the fraction of the input signal's energy reflected off the LC circuit is 4.7%, which is in good agreement with the predicted value of 4.5% obtained by numerically integrating Eqns. 3.6.

5.3.1 Calibration and capture protocols

To determine the field at the input of electromechanical device, we use the calibration protocol. We implement it by applying the blue-detuned pump coincident with the input field. In this case, the electromechanical device functions as a linear phase-preserving amplifier whose input and output are the incident and reflected microwave fields, respectively. These pulsed fields have different envelopes; nevertheless, they are related by an energy gain of $\cosh^2(r/2)$ where $r = \Gamma_{\mathrm{b}}\tau_{\mathrm{b}}$ and τ_{b} is the pump's duration as discussed in Section 3.1.3. If we regard the input of the amplifier

as the incident microwave field, the fluctuations of the resonator's motion are the source of the amplifier's added noise, reaching the quantum limit[126] if the resonator is in its ground state[53].

After obtaining the input state, we use the capture protocol to determine the resonator state. We first apply the red-detuned pump coincident with the input field. Once it is captured, we then apply the blue-detuned pump to amplify the resonator's state. In contrast to the calibration protocol, the amplifier's input can now be regarded as the state of the resonator. The output is still the reflected field, but the added noise is due to the vacuum fluctuations of the incident field. When interpreted this way, the electromechanical device functions as a linear phase-conjugating amplifier with an energy gain of $\sinh^2(r/2)$.

The gain is inherently tunable by adjusting $r = \Gamma_\mathrm{b}\tau_\mathrm{b}$. For the data presented in Fig. 5.7b, We obtain the gain by calculating the total energy of the amplified signal, $E_\mathrm{out} = \int_{-\infty}^{\infty}\langle V(t)\rangle^2\,\mathrm{d}t$ when the pumps were on. We then normalize E_out to the energy of the input signal, $E_\mathrm{in} = \int_{-\infty}^{\infty}\langle V(t)\rangle^2\,\mathrm{d}t$ when the pumps were off. During these measurements, $V_\mathrm{dc} = 0$ and the LC circuit was tuned out of resonance with the input signal. In Fig. 5.8, we plot the energy gain as a function of Γ_b. The model prediction was generated by discretizing and numerically integrating Eqns. 3.6 for the total input and output energies as Γ_b was varied. For the model prediction, we used the parameters outlined in Table 3.1. We find that the behavior of the amplification process (for large amplitude coherent signals) agrees well with the model.

5.3.2 Quadrature amplitude extraction

In order to characterize signals at the single-photon level, we express them in terms of a pair of quadrature amplitudes X and Y. During the amplification portion of either the calibration or capture protocol, the electromechanical device emits a signal that is routed to the detector. This signal has a known temporal envelope given by $f(t) = \exp(\Gamma_\mathrm{b}t/2)$ as discussed in Section 3.1.2.2 and is mixed down to a frequency of $\omega_\mathrm{IF}/2\pi = 1$ MHz. We digitally sample the mixed down signal at a rate of $R_\mathrm{s} = 5$ MHz and form a discrete set of time-stamped voltages $\{t_k, V_k\}$ where $t_k = k\cdot T_\mathrm{s}$ and $T_\mathrm{s} = R_\mathrm{s}^{-1}$ is the sampling period. Because the signal's spectral and temporal content is known,

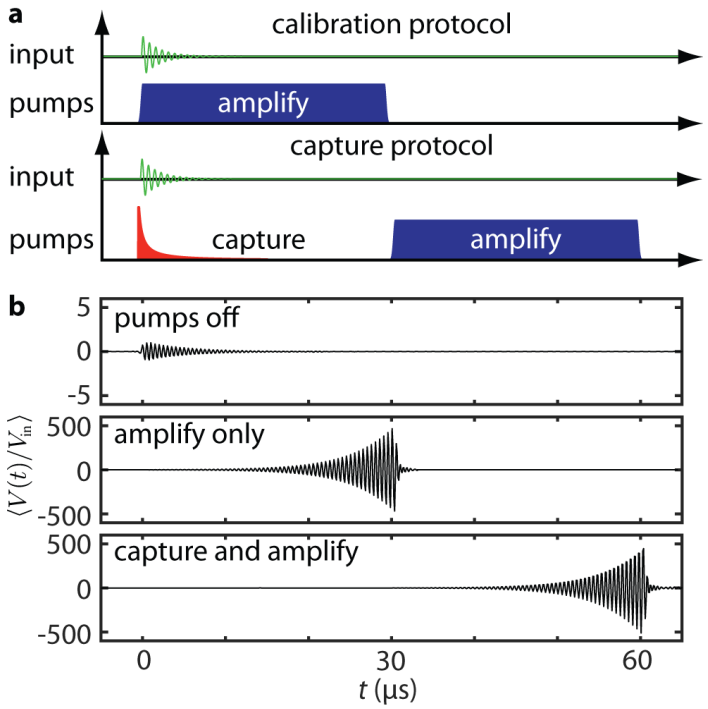

Figure 5.7: Calibration and capture protocols. **a,** Timing diagrams depicting the input coherent signal (green) of amplitude $V_{\rm in}$ and the pulse shapes of the pumps, $\Gamma_{\rm r}(t)$ and $\Gamma_{\rm b}(t)$, used to create the capture or amplification interaction. For the calibration protocol (top), the amplification pump is coincident with the signal pulse. The capture protocol (bottom) has a timing diagram similar to the calibration protocol, but the input signal is coincident with a capture pulse that is temporally shaped for optimal capture of the signal. At $t = 30$ μs, the mechanical state is amplified and converted back into a microwave field. **b,** The plots show the voltage signals, $V(t)$, measured at the detector and averaged over 500 repetitions of each protocol when the pumps were either off or on. During amplification, $\Gamma_{\rm b}/2\pi = 60$ kHz which results in a gain of 53 dB.

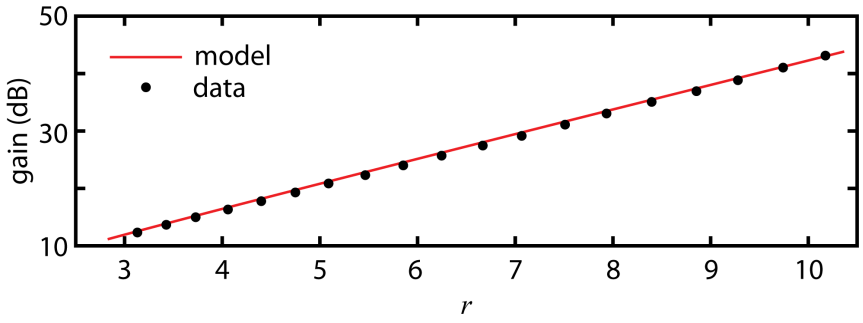

Figure 5.8: Adjustable gain of the mechanical amplifier. The plots shows the measured energy gain as $r = \Gamma_{\rm b}\tau_{\rm b}$ was varied. The measurements were acquired using the capture protocol. For these measurements, $\tau_{\rm b} = 30$ μs was held constant while $\Gamma_{\rm b}/2\pi$ was varied from 15 kHz to 55 kHz. The solid line indicates the expected performance obtained by numerically integrating Eqns. 3.6 with all parameters determined separately.

we can define a pair of quadrature amplitudes[65]

$$X = \sqrt{\frac{2T_s}{\mathcal{G}C}} \sum_{k=1}^{N} V_k f(t_k) \cos(\omega_{IF} t_k)$$
$$Y = \sqrt{\frac{2T_s}{\mathcal{G}C}} \sum_{k=1}^{N} V_k f(t_k) \sin(\omega_{IF} t_k) \tag{5.4}$$

where $C = \sum_{k=1}^{N} |f(t_k)|^2$, N is the total number of samples, and $\mathcal{G}$ is the gain that relates quantum fluctuations at the input of the electromechanical device to voltage fluctuations at its output.

5.3.3 Scaling the quadrature amplitudes

To scale the quadrature amplitudes, we determine $\mathcal{G}$ using reference measurements from a noise source of known variance. For each repetition of the calibration and capture protocols discussed in Section 5.3, we make a reference measurement in which vacuum fluctuations of the microwave field are injected into the electromechanical device. For this reference, the input to the electromechanical device is Johnson noise emitted from a 50 Ω load that is thermally anchored to the base stage of the dilution refrigerator held at a temperature T. For $T < 25$ mK and near the frequency ω_{LC}, the fluctuations in the microwave fields emitted from the load approach that of a vacuum state with an average occupation of approximately 0.06 quanta[131]. As such, this input microwave mode can be approximated as an ideal vacuum state described by the density operator $\rho_0 = |0\rangle\langle 0|$.

For the reference data set, we acquire a set of uncalibrated quadrature amplitudes that have a total voltage variance σ_V^2. If both the microwave and mechanical modes of the electromechanical device were in pure vacuum states, then the voltage fluctuations measured at the detector would have a total variance that corresponds to 1 quanta. For this case, one would calculate $\mathcal{G}$ so that $\mathcal{G}^{-1}\sigma_V^2 = 1$. However, even after cooling the mechanical resonator, we observe that it is in a weak thermal state with an average occupation n_{th}. We take into account this estimate by calculating $\mathcal{G}$ so that

$$\mathcal{G}^{-1}\sigma_V^2 = 1 + n_{th}.$$

We then use $\mathcal{G}$ to scale the quadrature amplitudes (defined by Eqns. 5.4) for both data sets to have units of $\sqrt{\text{quanta}}$. To minimize systematic errors in the estimate of $\mathcal{G}$ due to potential drifts during the measurement, we alternate between the vacuum reference and single photon measurements every 512 executions of each protocol.

5.4 Capture, storage, and amplification of single photons

The calibration and capture protocols enable the capture, storage, and amplification of a propagating microwave field as shown in Fig. 5.7. To verify that these two protocols can process a non-Gaussian quantum state, we prepare the propagating field in a mixed vacuum and single-photon state (see Section 4.3). Once the field is either directly amplified or captured, its state must be determined. This task requires the ability to perform quantum state tomography on both the input field and the mechanical resonator.

5.4.1 Tomographic procedure

By operating the electromechanical device as a low-noise amplifier as discussed in Section 5.2, we can perform full quantum state tomography on both the input microwave field and the mechanical resonator. For each repetition of the two protocols depicted in Fig. 5.10, we record a voltage signal, $V(t)$, at the detector during the amplification portion of each protocol. For each voltage record, we use Eqns. 5.4 and extract a pair of quadrature amplitudes, X and Y, for the state of either the resonator or input field. By making repeated measurements of $V(t)$, we obtain a set of quadrature amplitudes. We then use this information to extract a density matrix ρ via the method of maximum likelihood state tomography discussed in Section 2.5.3 and in Ref. [121]. We refer to the states of the input microwave field and of the mechanical resonator as ρ_{e} and ρ_m, respectively.

5.4.2 Tomographic results

After developing a tomographic procedure for determining the states of the input field and mechanical resonator, we test the calibration and capture protocols (see Section 5.3) using single

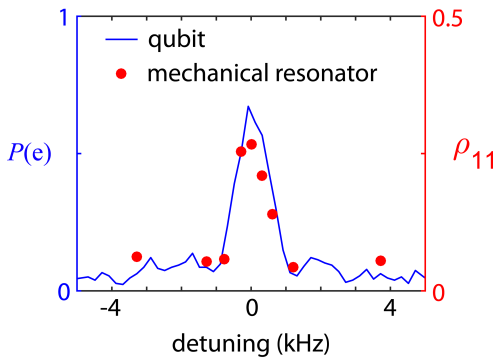

Figure 5.9: Correlated transmon qubit and mechanical states. The plot shows the probability of the qubit occupying the excited state $P(e)$ and the ρ_{11} component of the mechanical state's density matrix as a function of the qubit's blue sideband drive detuning $\Delta_{\mathrm{bs}} = \omega - \omega_{\mathrm{bs}}$.

photons generated by the cQED system. To avoid obscuring the single-photon signals with thermal fluctuations of the mechanical resonator, we employ sideband cooling to prepare the mechanical resonator near its quantum ground state of motion[53]. We execute this cooling step prior to the start of each protocol, thereby cooling the resonator's motion to a remaining occupancy of approximately 0.1 quanta (see Section 5.2.1). In addition to cooling, we perform a reference measurement in which no single photons are generated. This reference measurement enables proper scaling of X and Y in units of $\sqrt{\text{quanta}}$ as discussed in Section 5.3.3. Additionally, it serves as a control to verify the scatter in X and Y increases in the case that single photons are employed. Such an increase is expected for single-photon signals (see Section 2.1.3).

As a first test of the capture protocol with single photons, we verify that the qubit state and reconstructed mechanical state ρ_{m} are correlated. Because we drive the transition $|g\rangle|0\rangle \rightarrow |e\rangle|1\rangle$ to produce a single photon, the qubit excited state probability $P(e)$ and the single-photon component of ρ_{m} should depend on the sideband drive detuning $\Delta_{\mathrm{bs}} = \omega - \omega_{\mathrm{bs}}$. Specifically, we expect that a detuning of $\Delta_{\mathrm{bs}} = 0$ will maximize the single-photon component of ρ_{m}. As shown in Fig. 5.9, these two quantities are indeed correlated.

Next, we execute the calibration and capture protocols together with the tomographic procedure discussed in Section 5.4.1. For both protocols, the tomography yields density matrix estimates

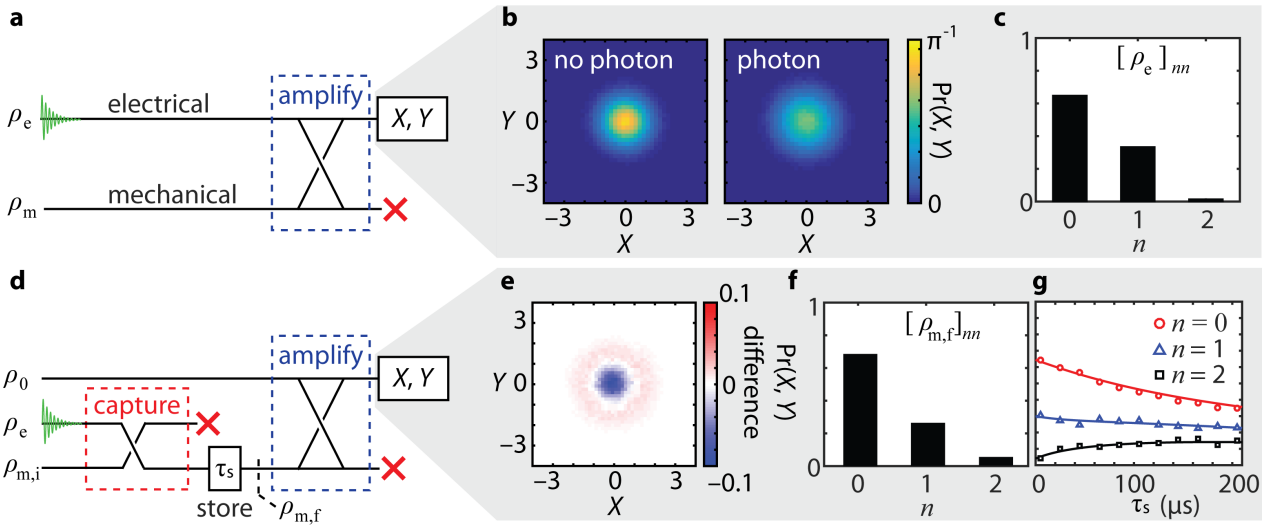

Figure 5.10: Capture, storage, and amplification of single propagating photons. **a,** The diagram shows the calibration protocol where the green decaying sinusoid represents an input microwave field in the state ρ_e. Prior to injecting an input state, the mechanical mode described by ρ_m is cooled close to its quantum ground state. A red cross indicates a mode was not measured. **b,** Histograms of 512,000 measured quadrature amplitudes X and Y for the input state are plotted such that the histograms form a discretized and normalized joint probability distribution $\Pr(X, Y)$. The labels 'no photon' and 'photon' indicate whether single photons were generated or not. **c,** The diagonal elements of ρ_e are obtained using a maximum likelihood state tomography (Supplemental Information). **d,** The diagram shows the capture protocol where $\rho_{m,i}$ is the initial mechanical state and τ_s is an adjustable storage time. After storage, the mechanical mode is in the final state $\rho_{m,f}$. During amplification, the electrical mode is in a vacuum state ρ_0. **e,** The figure shows the difference of the 'photon' and 'no photon' histograms acquired using the capture protocol, highlighting the phase symmetric character of a single *phonon* state. **f,** Diagonal elements of ρ_m obtained at $\tau_s < 3\ \mu$s. **g,** The diagonal elements of ρ_m decay toward their thermal equilibrium values as a function of τ_s. A model (solid lines) of ρ_m yields a characteristic storage time of $\tau_m = 137 \pm 6\ \mu$s as discussed in Section 5.4.4.

containing significant elements only on the diagonals as shown in Fig. 5.10c. In particular, we find that the probability of detecting a single photon is $[\rho_{\mathrm{e}}]_{11} = 0.33^{+0.02}_{-0.01}$, where the limits are the 90% confidence interval as discussed in Appendix B. After capture, the probability of a single *phonon* occupying the mechanical mode is $[\rho_{\mathrm{m}}]_{11} = 0.26^{+0.01}_{-0.02}$. In addition to performing tomography on the mechanical mode, we confirm that the captured state is nonclassical and that it can be mechanically-stored for an adjustable time.

5.4.3 Characterizing nonclassicality

To distinguish the captured state from a thermal or coherent state, we calculate the degree of second-order coherence $g^{(2)}_{\mathrm{m}}$ for the mechanical state. This quantity is often used to characterize the statistical properties of photons emitted from a source[98]. For example, an ideal single photon source has $\rho_{11} = 1$ with all other elements equal to zero. This state yields $g^{(2)}(0) = 0$. In general,

$$g^{(2)}(0) = \frac{\langle \hat{n}^2 \rangle - \langle \hat{n} \rangle}{\langle \hat{n} \rangle^2} \tag{5.5}$$

where $\hat{n}$ is the number operator. In terms of the density matrix elements, Eqn. 5.5 becomes

$$g^{(2)}(0) = \frac{\sum_n n(n-1)\rho_{nn}}{\left(\sum_n n\rho_{nn}\right)^2} \tag{5.6}$$

where $\rho_{nn} = \langle n|\rho|n\rangle$. Here, we use Eqn. 5.6 and the density matrix elements presented in Fig. 5.10f to calculate $g^{(2)}_{\mathrm{m}} = 0.89^{+0.05}_{-0.17}$ where the limits are the 90% confidence interval as discussed in Appendix B. For comparison, a thermal or coherent state of motion yields $g^{(2)}_{\mathrm{m}} \geq 1$.

5.4.4 Characterizing the storage time

After capturing single photons, we vary the storage time τ_{s} and test the ability to mechanically store a non-Gaussian state. The results of this test are shown in Fig. 5.10f. To quantify the storage time, we use a master equation formalism to model the evolution of ρ_{m} with the characteristic storage time τ_{m} as the only free parameter. The master equation is discussed in Section 2.1.4 and

in Ref. [108]. In the number basis, it becomes a set of coupled ordinary differential equations given by

$$\frac{dP_n}{dt} = -\kappa\left[(N+1)nP_n(t) + N(n+1)P_n(t) - (N+1)(n+1)P_{n+1}(t) - NnP_{n-1}(t)\right], \tag{5.7}$$

where $P_n = \langle n|\rho_m|n\rangle$ describes the probability of observing n excitations in the mechanical mode and $N = n_{\mathrm{m}}$ is the average occupation of the mechanical resonator's environment. Because $N \gg 1$ as discussed in Section 5.2.1, we make the approximation $N + 1 \approx N$. This approximation allows one to parametrize Eqn. 5.7 using the decoherence rate, $\gamma_{\mathrm{m}} = \kappa N$, as a single parameter. By discretizing and numerically integrating Eqn. 5.7, we obtain $P_n(t)$. In this model, the mechanical decoherence rate γ_{m} is a free parameter and the estimated density matrix elements of the initial state are used to fix $P_n(0)$. Simultaneous fits to the inferred diagonal elements presented in Fig. 5.10g yields a characteristic storage time for a mixed photon state of $\tau_{\mathrm{m}} = \gamma_{\mathrm{m}}^{-1} = 137 \pm 6$ μs, which is about ten times longer than the time used to capture the input photon state.

As a control experiment, we do not capture and store single photons. For this experiment, we execute the protocol depicted in Fig. 5.10 of the main text but without producing single photons using the cQED system. The results of this experiment and fits to the model are shown in Fig. 5.11. To model the data, we assume the mechanical resonator is initially in a thermal state and remains thermal but with increasing average occupation

$$\langle n\rangle = \sum_n nP_n$$

as it equilibrates with the thermal bath. In this case, Eqn. 5.7 can be simplified by using

$$\frac{d}{dt}\langle n(t)\rangle = \sum_n n(t)\frac{dP_n(t)}{dt} \tag{5.8}$$

and Eqn. 5.7 to obtain

$$\frac{d}{dt}\langle n(t)\rangle = -\kappa\left(\langle n(t)\rangle - N\right). \tag{5.9}$$

Using the solutions to this rate equation, and the thermal distribution

$$P_n = \frac{\langle n\rangle^n}{(\langle n\rangle + 1)^{n+1}}, \tag{5.10}$$

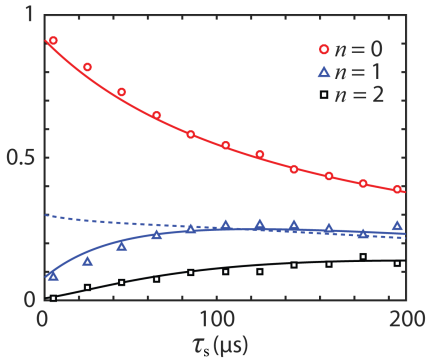

Figure 5.11: Evolution of a mechanical thermal state. The plot shows the first three diagonal density matrix elements of the extracted mechanical state ρ_m as a function of the storage time τ_s. The plot is similar to the one in Fig. 5.10g, but for the control experiment in which no single photons were generated and captured. The solid lines indicate a model of a thermal state that uses τ_m as a free parameter. The fit yields $\tau_m = 137 \pm 8$ μs. For comparison, the dashed line indicates the evolution of P_1 for the initial mixed phonon state presented in Fig. 5.10g. In this case, a single photon was captured and stored in the mechanical resonator.

We simultaneously fit the estimated density matrix elements shown in Supplementary Fig. 5.11 and extract $\tau_m = 137 \pm 8$ μs, which agrees with the storage time obtained using single photons.

5.5 Characterization of the capture process

Having demonstrated the ability to capture single photons, we now characterize how the capture process affects an arbitrary qubit state. In general, the process of converting a quantum state from a propagating photon to motion of the mechanical resonator can be thought of as a 'black box' with an input and output[70], as depicted in Fig. 5.12. This black box takes an input electrical state ρ_e and converts it to an output mechanical state ρ_m. These two states are related by the quantum operation $\mathcal{E}$ where $\rho_m = \mathcal{E}(\rho_e)$. Ideally, the black box does not corrupt the converted quantum state. In this case, $\mathcal{E}$ is the identity matrix and so $\rho_m = \rho_e$. However, in any real experiment, there is loss and noise that corrupt the conversion process and so $\mathcal{E}$ will not simply be the identity matrix. To characterize the quality of the map $\mathcal{E}$, we use the average fidelity.

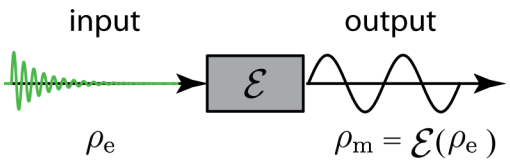

Figure 5.12: Black box model of the conversion process. The input (green) is described by the state ρ_e. A process $\mathcal{E}$ converts ρ_e to mechanical motion described by the output state ρ_m.

5.5.1 Average fidelity characterizes process

In general, a quantum process is described mathematically by a completely-positive trace preserving (CPTP) map

$$\mathcal{E} : \rho \to \mathcal{E}(\rho).$$

The *average fidelity* of a process is a measure of how well that process preserves quantum information. It is defined as

$$F_{\text{avg}} = \int d\Psi \, \langle\Psi| \, \mathcal{E}(|\Psi\rangle \langle\Psi|) \, |\Psi\rangle \tag{5.11}$$

where $\int d\Psi = 1$. That is, the average fidelity gives the average overlap of the output of the process with the initial state, averaged over all pure states. A related quantity is the *entanglement fidelity*, which is defined as follows: let $|\phi\rangle = \frac{1}{d^2} \sum_i |i\rangle \, |i\rangle$ denote a maximally entangled state. Here, $\{|i\rangle\}$ is an orthonormal basis and d is the dimension of the Hilbert space on which the process $\mathcal{E}$ acts. Then the *entanglement fidelity* is

$$F_e = \langle\phi| \, (\mathcal{E} \otimes \mathbb{I})(|\phi\rangle \langle\phi|) \, |\phi\rangle \, . \tag{5.12}$$

The entanglement fidelity measures how well a system's entanglement with another system is preserved when the quantum process acts only on the first system. The entanglement fidelity can be calculated by expanding Eqn. 5.12 in terms of its basis states:

$$F_e = \frac{1}{d^2} \sum_{ij} \langle i| \, \langle i| \, (\mathcal{E}(|i\rangle \langle j|) \otimes |i\rangle \langle j|) \, |j\rangle \, |j\rangle \, . \tag{5.13}$$

Because $\langle i|j\rangle = \delta_{ij}$, the above expression simplifies to

$$F_e = \frac{1}{d^2} \sum_{ij} \langle i| \, \mathcal{E}(|i\rangle \langle j|) \, |j\rangle \, . \tag{5.14}$$

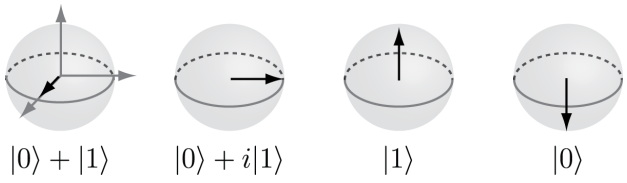

Figure 5.13: A set of linearly independent states. Converting this set of states is sufficient to determine the average fidelity of the conversion process that acts on states of dimension $d = 2$.

The utility of the entanglement fidelity is that it is easy to calculate, and there is a simple formula relating the average fidelity to the entanglement fidelity [87]:

$$F_{\text{avg}} = \frac{d \times F_{\text{e}} + 1}{d + 1} \tag{5.15}$$

Because quantum processes act as linear operators on the space of operators, the fidelity can be determined if the outputs $\mathcal{E}(\rho_i)$ are known for each of a set of input states ρ_i that span the space of operators on Hilbert space. For a Hilbert space of dimension d, d^2 linearly independent density matrices are required[128]. A set of four linearly independent states for $d = 2$ are shown Fig. 5.13.

5.5.2 Classical bound on the average fidelity

There is a bound of $F_{\text{avg}} = 2/3$ for converting a single qubit state using only classical resources. This bound is achieved as follows. Suppose we have two people, Alice and Bob, who want to share quantum information with each other. Imagine Alice has a qubit prepared in state ρ_A, which she wishes to send to Bob through a classical communication channel (e.g., a telephone). If Alice and Bob share a maximally entangled Bell state, then this transmission of quantum information can be achieved via a teleportation protocol[200]. However, the use of such an entangled state would constitute a quantum resource and is thus not allowed in this consideration. The best Alice can do then is measure the qubit in some basis, and report the outcome to Bob, who then prepares his qubit in the eigenstate corresponding to Alice's measurement outcome. The quantum operation describing this process is

$$\mathcal{E}(\rho) = P_0 \left|0\right\rangle \left\langle 0\right| + P_1 \left|1\right\rangle \left\langle 1\right| \tag{5.16}$$

where $P_0 = \langle 0| \rho_A |0\rangle$ is the probability that Alice measures $|0\rangle$, and simlarly for P_1. To calculate the average fidelity, I insert this process into Eqn. 5.14:

$$\begin{aligned} F_{\mathrm{e}} &= \frac{1}{4}\sum_{ij} \langle i| \mathcal{E}(|i\rangle \langle j|)\, |j\rangle \\ &= \frac{1}{4}\sum_{ij} \langle i| \langle 0|i\rangle \langle j|0\rangle |0\rangle \langle 0| + \langle 1|i\rangle \langle j|1\rangle |1\rangle \langle 1|)\, |j\rangle \\ &= \frac{1}{2}. \end{aligned}$$

Using Eqn. 5.15 and the above result, we find that $F_{\mathrm{avg}} = 2/3$. This bound can be generalized by considering the problem of guessing the state of a qubit given an optimal measurement on an ensemble of N identical copies of that qubit[201]. In this case, maximum possible fidelity is $(N+1)/(N+2)$, which equals 2/3 for an ensemble consisting of a single qubit, $N = 1$.

5.5.3 Conversion of qubits

Qubits are encoded as superpositions of zero and one photons that propagate in a transmission line connected to the electromechanical device. As discussed in Section 5.5.1, the process of capturing a propagating state is described by a map $\mathcal{E}$ between incident and captured states whose quality is characterized by the average fidelity F_{avg}. To determine F_{avg}, it is sufficient to capture a set of states that includes a single photon state and superpositions of zero and one photons as pointed out in Section 5.5.1. we can create superposition states by first preparing the transmon qubit in the superposition $\frac{1}{\sqrt{2}}\left(|g\rangle + e^{i\varphi}|e\rangle\right)$, with varying phase φ, as shown in Fig. 5.14a.

To perform tomography on the qubit as shown in Fig. 5.14b, we measure the qubit's excited state population $P(e)$ using the electromechanical device as a low-noise amplifier (see Section 4.2.2.2). Achieving full state tomography can be achieved by first preparing the qubit in a superposition state and then measuring its Pauli components[202]. To determine the qubit's $-\sigma_z$ component, we simply measure $P(e)$. Next, to determine the $-\sigma_y$ component, we apply a $\pi/2$ rotation about the x-axis and then measure $P(e)$. Lastly, we obtain the $+\sigma_x$ component by applying a $\pi/2$ rotation about the y-axis and then measuring $P(e)$.

By driving the transition $|g\rangle|0\rangle \rightarrow |e\rangle|1\rangle$, we can transfer the superposition state from the transmon to the cavity and then let the cavity state evolve into the propagating field. Operating the capture protocol on this set of states shows that the phase of the qubit state is converted to the motion of the mechanical resonator as shown in Fig. 5.14c.

To perform tomography on the input and captured states, we follow the procedure illustrated in Fig. 5.10 and determine both ρ_{e} and ρ_{m}. To calculate the fidelity of the capture process in this experiment, the estimated input and output density matrices are truncated to a Hilbert space dimension of $d = 2$. The input states are obtained by estimating the density matrix of the input microwave field after executing the calibration protocol. Similarly, the output states are obtained by estimating the density matrix of the mechanical resonator state after executing the capture protocol. A set of basis states is formed by using the following input states: a vacuum state, a mixed vacuum and single-photon state, and mixed superposition states with phases chosen from the set $\{0, \pi/2\}$. We expand operators $|i\rangle\langle j|$ in this basis. The average fidelity F_{avg} is then calculated using the known input and output states presented in Table B.2 together with Eqns. 5.14 and 5.15. The input and captured density matrices provide enough information to calculate $F_{\mathrm{avg}} = 0.83^{+0.03}_{-0.06}$ for arbitrary qubit states. Crucially, the average fidelity exceeds 2/3, the highest possible fidelity for transferring qubits using only classical resources as pointed out in Section 5.5.1.

5.5.4 Model of the capture process

The capture process maps the state of a propagating microwave field to the motion of the mechanical resonator. This process can be viewed as implementing a beamsplitter interaction between the microwave and the mechanical modes of the electromechanical device[64]. A rudimentary model of the capture process therefore involves sending the state of the microwave field through one port of a beamsplitter and the state of the mechanical mode through the other input port. The transmissivity of the beamsplitter models imperfect capture of the propagating mode. For an ideal capture of the propagating microwave mode, there would be no reflected microwave power off of the electromechanical device. After tracing over the output microwave mode, the mechanical

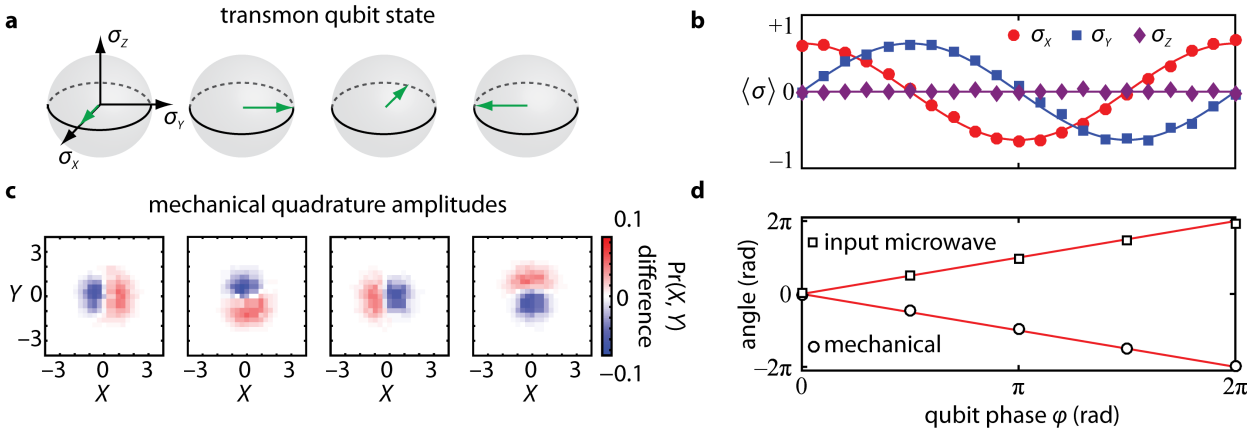

Figure 5.14: Conversion of propagating qubits. **a,** The transmon qubit was prepared in the superposition state $\frac{1}{\sqrt{2}}\left(|g\rangle + e^{i\varphi}|e\rangle\right)$ with a phase φ chosen from the set $\{0, \pi/2, \pi, 3\pi/2\}$, as denoted by the green arrow plotted on a Bloch sphere. **b,** The plot shows measured Pauli component amplitudes, $\langle\sigma_k\rangle$, of the qubit state as a function of its phase where $k = \{x, y, z\}$. Single-shot readout of the qubit state was achieved by using the electromechanical device as a nearly quantum-limited amplifier. The solid lines are fits with the readout contrast of 60% as the only free parameter. **c,** Difference between the 'photon' and 'no photon' histograms (similar to Fig. 5.10e) show the mechanical quadrature amplitudes, X and Y, as the transmon qubit's phase was varied. **d,** The plot shows the argument of the off-diagonal density matrix element, ρ_{01}, for both the input microwave, ρ_{e}, and captured mechanical, ρ_{m}, states as a function of φ. The mechanical state changes linearly in φ, indicating that the conversion process is coherent. The apparent opposite dependence of φ of the input and captured states is a result of the phase conjugate amplification of the mechanical state compared to the direct amplification of the input microwave state (solid lines indicate the expected behavior).

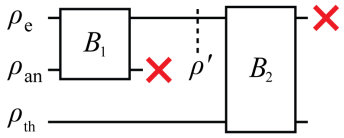

Figure 5.15: Model of the capture process. The diagram depicts the three modes and the two beamsplitter interactions used to model the capture process. The input state of the electrical mode is ρ_e and the ancilla state ρ_{an} describes the state of the additional electrical mode. The mechanical mode is in the thermal state ρ_{th}. The electrical modes couple via a beamsplitter interaction B_1 and the states ρ' and ρ_{th} couple via another beamsplitter interaction B_2. A red cross denotes a partial trace.

resonator would contain the state of the input propagating microwave mode.

A limitation of this model is that it does not take into account the non-zero occupancy of the mechanical mode that is observed in this experiment. Ideally, an input vacuum state of the microwave field to a beamsplitter with perfect efficiency would result in a vacuum state of the mechanical mode. This model would describe the ideal cooling of the mechanical mode to its quantum ground state. However, we observe a small residual occupation in the mechanical mode n_{th}. A possible source of this residual occupation is the internal loss of the LC circuit due to a surface layer of two-level system fluctuators[203]. This internal loss couples the microwave mode to a thermal bath with a non-zero occupation.

We incorporate imperfect capture efficiency and internal loss of the LC circuit into a heuristic model, as shown in Fig. 5.15. This model contains two beamsplitters, B_1 and B_2, which model the internal loss of the LC circuit and the capture efficiency, respectively. The input electrical state ρ_e and an ancillary electrical thermal state ρ_{an} are sent through a beamsplitter B_1, and the reduced state of the output electrical mode is then mixed with a thermal state of the mechanical mode ρ_{th} on beamsplitter B_2. Explicitly, this complete process is

$$\rho_{out} = \mathrm{tr}_e(B_2\,\rho' \otimes \rho_{th}\,B_2^\dagger) \tag{5.17}$$

where $\rho' = \mathrm{tr}_{an}(B_1\,\rho_{an} \otimes \rho_e\,B_1^\dagger)$. The ancilla state ρ_{an} is taken to be a thermal state whose thermal occupancy is determined implicitly by the requirement that a vacuum input state $\rho_e = |0\rangle\langle 0|$ yields a thermal intermediate state $\rho' = \rho_{th}$ with mean occupancy $n_{th} = 0.1$ quanta, as discussed

in Section 5.2.1. In the Heisenberg picture[102, 98], a beamsplitter transforms the annihilation operators for its two input modes a_1 and a_2 as $B^\dagger a_{1,2} B = a'_{1,2}$, where

$$\begin{pmatrix} a'_1 \\ a'_2 \end{pmatrix} = \begin{pmatrix} \cos\theta & -\sin\theta \\ \sin\theta & \cos\theta \end{pmatrix} \begin{pmatrix} a_1 \\ a_2 \end{pmatrix}. \tag{5.18}$$

Under this convention, $\theta = 0$ gives the identity whereas $\theta = \pi/2$ corresponds to perfect capture. The beamsplitters in the model are thus each parametrized by an angle θ_i where $i = \{1, 2\}$, which in turn is related to the *reflection coefficient* $R_i = \sin^2\theta_i$.

For the data presented in Fig. 5.7, the fraction of energy reflected from the electromechanical device is approximately 5%. As such, we use $R_2 = 0.95$ for B_2. Note that a low amount of reflected energy corresponds to a large value of the beamsplitter reflection coefficient, because the reflection coefficient models the efficiency of mode swapping. As discussed in Chapter 3, the fractional resonator energy loss is measured to be approximately 0.14 and so we use $R_1 = 0.14$ for B_1.

This cascaded beamsplitter model provides a way to predict the captured mechanical states from the known input states obtained using the calibration protocol. For example, using the mixed single photon input state described in the main text, the model predicts $[\rho_\mathrm{m}]_{00} = 0.67$, $[\rho_\mathrm{m}]_{11} = 0.27$, and $[\rho_\mathrm{m}]_{22} = 0.05$, whereas the 90% confidence intervals for these quantities obtained from tomography and bootstrapping are [0.68, 0.69], [0.24, 0.27], and [0.05, 0.06], respectively. The model developed in this section is also used to estimate the bias in the average fidelity calculation. This bias is due to truncating the input and output density matrices to dimension $d = 2$, as discussed in Appendix B

The mathematical description of the capture process should be viewed as a heuristic model. This model relies on two free parameters, the measured circuit loss and capture efficiency, which were measured independently and may vary for each experimental run. Nevertheless, to the degree that this model accurately describes the process, it provides prospects for improving the capture process fidelity. For example, it is conceivable that reducing the circuit loss, increasing the capture efficiency, and minimizing the occupation of the mechanical mode should yield a capture process that approaches unit fidelity.

Chapter 6

Conclusion

In this thesis, I describe the conversion of signals that encode quantum information to the motion of a micrometer-sized mechanical resonator. Such macroscopic resonators are appealing for use in quantum science and technology because they can interface diverse physical systems that include signals at optical and microwave frequencies[27], superconducting qubits[37], and even single electronic spins[38]. Yet it has been an outstanding challenge to interface mechanical motion with a propagating signal comprised of a single photon, which is essential in emerging quantum communication and modular quantum computation architectures. To address this challenge, I use the mechanical system discussed in Chapter 3 to capture single photons emitted from the cQED system described in Chapter 4. Importantly, the cQED system generates superpositions of zero and one photons that can encode a single quantum bit of information – that is, a qubit.

Converting propagating qubits to mechanical motion is a crucial step towards storing more complex states for use in protocols that require the feedforward of information, such as certain quantum teleportation[204] and quantum error correction schemes[205, 206]. For example, teleporting a quantum state utilizes shared entanglement[200]. To generate entanglement, one can use the cQED system to produce the Bell state

$$|\psi\rangle = (|g\rangle\,|1\rangle + |e\rangle\,|0\rangle)/\sqrt{2}$$

where the first (second) ket represents the transmon qubit (propagating photon) state[207]. By converting the Bell state to the motion of the mechanical resonator, its motional state can be entangled with the transmon qubit. To verify entanglement, one must use quantum state tomography

to determine the density matrix of the joint qubit and mechanical resonator system[208]. As part of this tomographic procedure, one must determine not only the $\langle\sigma_z\rangle$ component of the qubit, but also its $\langle\sigma_x\rangle$ and $\langle\sigma_y\rangle$ components. Determining these components requires a protocol that includes a $\pi/2$ pulse to rotate the qubit[202] followed by a measurement pulse to probe the qubit state-dependent shift of the cavity[164, 209]. A standard approach to efficiently probing the cavity state is through the use of a cQED system that employs a separate qubit-readout resonator[180, 86]. To efficiently measure the mechanical resonator's state, it must be reconstructed using quantum state tomography as pointed out in Section 2.5.

Efficient tomography of the mechanical state underscores the need for harnessing the mechanical resonator itself as part of a low-noise amplifier. In this thesis, I use the mechanical resonator to realize a phase-insensitive amplifier. As pointed out in Section 2.5.2, this type of amplifier inevitably adds 1/2 quanta of noise while simultaneously detecting both quadratures of a signal. In contrast, achieving ideally noiseless detection requires the use of a phase-sensitive amplifier[131]. A route towards this goal is to use the actuation electrode (see Section 3.1.4) to parametrically drive the mechanical resonator at twice its resonant frequency. Such an approach has been used to amplify thermal states of a mechanical resonator[210], but has not yet been used to amplify non-Gaussian quantum states. By pulsing the parametric drive, it may be possible to achieve phase-sensitive gain that exceeds 30 dB. To add nearly no noise during this amplification process, it must be performed on a timescale that avoids unwanted mechanical decoherence. Furthermore, voltage fluctuations from the actuation line must be minimized so that they do not incoherently drive the mechanical resonator.

Apart from demonstrating phase-sensitive mechanical amplification of a quantum state, an outstanding challenge is to faithfully convert it to telecommunications light. Such light can efficiently distribute quantum information over distances that can easily exceed a few kilometers. In contrast, microwave systems can only distribute quantum signals over tens of meters[211]. To achieve conversion between microwave and optical light, emerging devices couple a mechanical resonator to both microwave circuitry and an optical cavity[212, 213, 214, 215]. Yet the device

currently under development in our lab is restricted to a narrow bandwidth of ~ 10 kHz. To interface the narrow-bandwidth photon source presented in Chapter 4 with this device, its bandwidth must be boosted by at least two orders of magnitude. Furthermore, achieving high-fidelity transduction requires that the added noise during the conversion process must be much less than 1/2 quanta[216]. Progress is already underway to combat this undesired added noise[217]. To this end, microfabrication advances provide prospects for boosting mechanical lifetimes to the minute time scale[218, 219].

Beyond advancing quantum information processing, this thesis takes a step towards probing quantum phenomena in a fundamentally new regime[220]. In particular, recent proposals contend that macroscopic mechanical resonators may serve as a testbed for quantum theory in massive objects[221, 82, 222, 223, 224, 225, 226, 227, 228]. Yet many of these proposals face the extraordinary challenge of accessing superpositions of macroscopically distinguishable mechanical states. By converting superposition of zero and one photons to the motion of a macroscopic mechanical resonator, its center-of-mass motion can be delocalized over a distance of order the mode's zero-point motion x_{zp}. To create more delocalized states of motion, the next step is to convert superpositions with larger average photon numbers such as Schrödinger cat states[85]. Such an experiment is daunting because the mechanical cat state can be easily thwarted by decoherence. But if carried out successfully, it may provide an empirical way to falsify speculative conjectures that quantum theory somehow breaks down for sufficiently massive objects.

Bibliography

[1] H. Cavendish, "Experiments to determine the density of earth," Philosophical Transactions of the Royal Society of London, vol. 88, pp. 469–526, 1798.

[2] J. Kepler, Tychonis Brahei Dani Hyperaspistes. Frankfurt: Apud G. Tampachium, 1625. [Online]. Available: https://archive.org/details/tychonisbraheida00kepl

[3] M. Köhler, T. Minato, H. Kimura, and I. Mann, "Radiation pressure force acting on cometary aggregates," Advances in Space Research, vol. 40, no. 2, pp. 266 – 271, 2007. [Online]. Available: www.sciencedirect.com/science/article/pii/S0273117707005376

[4] J. C. Maxwell, "A treatise on electricity and magnetism," vol. 1, 1873.

[5] P. Lebedew, "Untersuchungen uber die druckkrafte des lichtes," vol. 311, no. 11, pp. 433–458, 1901. [Online]. Available: http://dx.doi.org/10.1002/andp.19013111102

[6] E. F. Nichols and G. F. Hull, "A preliminary communication on the pressure of heat and light radiation," Phys. Rev. (Series I), vol. 13, no. 11, pp. 307–320, Nov. 1901. [Online]. Available: http://link.aps.org/doi/10.1103/PhysRevSeriesI.13.307

[7] A. Ashkin, "Acceleration and trapping of particles by radiation pressure," Phys. Rev. Lett., vol. 24, pp. 156–159, Jan 1970. [Online]. Available: http://link.aps.org/doi/10.1103/PhysRevLett.24.156

[8] T. Hänsch and A. Schawlow, "Cooling of gases by laser radiation," Optics Communications, vol. 13, no. 1, pp. 68 – 69, 1975. [Online]. Available: //www.sciencedirect.com/science/article/pii/0030401875901595

[9] D. J. Wineland and H. Dehmelt, "Proposed 10^{14} $\delta\nu < \nu$ laser fluorescence spectroscopy on Tl+ mono-ion oscillator," Bull. Am. Phys. Soc., vol. 20, p. 637, 1975.

[10] A. Ashkin, "Trapping of atoms by resonance radiation pressure," Phys. Rev. Lett., vol. 40, pp. 729–732, Mar 1978. [Online]. Available: http://link.aps.org/doi/10.1103/PhysRevLett.40.729

[11] D. J. Wineland, R. E. Drullinger, and F. L. Walls, "Radiation-pressure cooling of bound resonant absorbers," Phys. Rev. Lett., vol. 40, pp. 1639–1642, Jun 1978. [Online]. Available: http://link.aps.org/doi/10.1103/PhysRevLett.40.1639

[12] W. Neuhauser, M. Hohenstatt, P. Toschek, and H. Dehmelt, "Optical-sideband cooling of visible atom cloud confined in parabolic well," Phys. Rev. Lett., vol. 41, pp. 233–236, Jul 1978. [Online]. Available: http://link.aps.org/doi/10.1103/PhysRevLett.41.233

[13] F. Diedrich, J. C. Bergquist, W. M. Itano, and D. J. Wineland, "Laser cooling to the zero-point energy of motion," Phys. Rev. Lett., vol. 62, pp. 403–406, Jan 1989. [Online]. Available: http://link.aps.org/doi/10.1103/PhysRevLett.62.403

[14] J. Weber, "Observation of the thermal fluctuations of a gravitational-wave detector," Phys. Rev. Lett., vol. 17, pp. 1228–1230, Dec 1966. [Online]. Available: http://link.aps.org/doi/10.1103/PhysRevLett.17.1228

[15] ——, "Gravitational radiation," Phys. Rev. Lett., vol. 18, pp. 498–501, Mar 1967. [Online]. Available: http://link.aps.org/doi/10.1103/PhysRevLett.18.498

[16] ——, "Gravitational-wave-detector events," Phys. Rev. Lett., vol. 20, pp. 1307–1308, Jun 1968. [Online]. Available: http://link.aps.org/doi/10.1103/PhysRevLett.20.1307

[17] M. E. Gertsenshtein and V. I. Pustovoit, "On the detection of low frequency gravitational waves," JETP, vol. 43, August 1962.

[18] R. Weiss, "Electromagnetically coupled broadband gravitational antenna," Quarterly Progress Report, Research Laboratory of Electronics, no. 105, pp. 54 – 76, 1972. [Online]. Available: https://dspace.mit.edu/bitstream/handle/1721.1/56271/RLE_QPR_105_V.pdf?sequence=1#page=38

[19] B. P. Abbott et al., "Observation of gravitational waves from a binary black hole merger," Phys. Rev. Lett., vol. 116, p. 061102, Feb 2016. [Online]. Available: http://link.aps.org/doi/10.1103/PhysRevLett.116.061102

[20] ——, "Localization and broadband follow-up of the gravitational-wave transient GW150914," The Astrophysical Journal Letters, vol. 826, p. L13, Jul. 2016. [Online]. Available: http://link.aps.org/doi/10.1103/PhysRevLett.20.1307

[21] V. Braginsky, A. B. Manukin, and M. Y. Tikhonov, "Investigation of dissipative ponderomotive effects of electromagnetic radiation," Journal of Experimental and Theoretical Physics, vol. 31, no. 5, p. 829, 1970.

[22] V. Braginsky and Y. I. Vorontsov, "Quantum-mechanical limitations in macroscopic experiments and modern experimental technique," Soviet Physics Uspekhi, vol. 17, no. 5, p. 644, 1975. [Online]. Available: http://stacks.iop.org/0038-5670/17/i=5/a=R02

[23] V. Braginsky and V. D. Popel'nyuk, "Small-vibration detector for a gravitation antenna," Pis'ma Zh. Eksp. Teor. Fiz., vol. 33, pp. 423–425, 1981.

[24] C. M. Caves, "Quantum-mechanical radiation-pressure fluctuations in an interferometer," Phys. Rev. Lett., vol. 45, pp. 75–79, Jul 1980. [Online]. Available: http://link.aps.org/doi/10.1103/PhysRevLett.45.75

[25] M. Poot and H. S. van der Zant, "Mechanical systems in the quantum regime," Physics Reports, vol. 511, no. 5, pp. 273 – 335, 2012, mechanical systems in the quantum regime. [Online]. Available: http://doi.org/10.1016/j.physrep.2011.12.004

[26] Y. Greenberg, Y. A. Pashkin, and E. Il'ichev, "Nanomechanical resonators," Physics-Uspekhi, vol. 55, no. 4, p. 382, 2012. [Online]. Available: http://stacks.iop.org/1063-7869/55/i=4/a=A03

[27] M. Aspelmeyer, T. J. Kippenberg, and F. Marquardt, "Cavity optomechanics," Rev. Mod. Phys., vol. 86, pp. 1391–1452, Dec 2014. [Online]. Available: http://link.aps.org/doi/10.1103/RevModPhys.86.1391

[28] K. Schwab, "Spring constant and damping constant tuning of nanomechanical resonators using a single-electron transistor," Applied Physics Letters, vol. 80, no. 7, pp. 1276–1278, 2002. [Online]. Available: http://dx.doi.org/10.1063/1.1449533

[29] M. D. LaHaye, O. Buu, B. Camarota, and K. C. Schwab, "Approaching the quantum limit of a nanomechanical resonator," Science, vol. 304, no. 5667, pp. 74–77, 2004. [Online]. Available: http://science.sciencemag.org/content/304/5667/74

[30] A. Naik, O. Buu, M. D. LaHaye, A. D. Armour, A. A. Clerk, M. P. Blencowe, and K. C. Schwab, "Cooling a nanomechanical resonator with quantum back-action," Nature, vol. 443, no. 7108, pp. 193–196, Sep. 2006. [Online]. Available: http://dx.doi.org/10.1038/nature05027

[31] A. N. Cleland, J. S. Aldridge, D. C. Driscoll, and A. C. Gossard, "Nanomechanical displacement sensing using a quantum point contact," Applied Physics Letters, vol. 81, no. 9, pp. 1699–1701, 2002. [Online]. Available: http://dx.doi.org/10.1063/1.1497436

[32] N. E. Flowers-Jacobs, D. R. Schmidt, and K. W. Lehnert, "Intrinsic noise properties of atomic point contact displacement detectors," Phys. Rev. Lett., vol. 98, p. 096804, Mar 2007. [Online]. Available: http://link.aps.org/doi/10.1103/PhysRevLett.98.096804

[33] J. D. Teufel, C. A. Regal, and K. W. Lehnert, "Prospects for cooling nanomechanical motion by coupling to a superconducting microwave resonator," New Journal of Physics, vol. 10, no. 9, p. 095002, 2008. [Online]. Available: http://stacks.iop.org/1367-2630/10/i=9/a=095002

[34] J. D. Teufel, J. W. Harlow, C. A. Regal, and K. W. Lehnert, "Dynamical backaction of microwave fields on a nanomechanical oscillator," Phys. Rev. Lett., vol. 101, p. 197203, Nov 2008. [Online]. Available: http://link.aps.org/doi/10.1103/PhysRevLett.101.197203

[35] C. A. Regal, J. D. Teufel, and K. W. Lehnert, "Measuring nanomechanical motion with a microwave cavity interferometer," Nature Physics, vol. 4, pp. 555 – 560, 7/2008 2008. [Online]. Available: http://www.nature.com/nphys/journal/v4/n7/full/nphys974.html

[36] C. R. Locke, M. E. Tobar, E. N. Ivanov, and D. G. Blair, "Parametric interaction of the electric and acoustic fields in a sapphire monocrystal transducer with a microwave readout," Journal of Applied Physics, vol. 84, no. 12, pp. 6523–6527, 1998. [Online]. Available: http://dx.doi.org/10.1063/1.369023

[37] A. D. O'Connell, M. Hofheinz, M. Ansmann, R. C. Bialczak, M. Lenander, E. Lucero, M. Neeley, D. Sank, H. Wang, M. Weides, J. Wenner, J. M. Martinis, and A. N. Cleland, "Quantum ground state and single-phonon control of a mechanical resonator," Nature, vol. 464, no. 7289, pp. 697–703, Apr. 2010. [Online]. Available: http://dx.doi.org/10.1038/nature08967

[38] D. Rugar, R. Budakian, H. J. Mamin, and B. W. Chui, "Single spin detection by magnetic resonance force microscopy," Nature, vol. 430, pp. 329–332, 2004. [Online]. Available: http://www.nature.com/nature/journal/v430/n6997/full/nature02658.html

[39] A. D. Armour, M. P. Blencowe, and K. C. Schwab, "Entanglement and decoherence of a micromechanical resonator via coupling to a cooper-pair box," Phys. Rev. Lett., vol. 88, p. 148301, Mar 2002. [Online]. Available: http://link.aps.org/doi/10.1103/PhysRevLett.88.148301

[40] I. Martin, A. Shnirman, L. Tian, and P. Zoller, "Ground-state cooling of mechanical resonators," Phys. Rev. B, vol. 69, p. 125339, Mar 2004. [Online]. Available: http://link.aps.org/doi/10.1103/PhysRevB.69.125339

[41] L. Tian, "Entanglement from a nanomechanical resonator weakly coupled to a single cooper-pair box," Phys. Rev. B, vol. 72, p. 195411, Nov 2005. [Online]. Available: http://link.aps.org/doi/10.1103/PhysRevB.72.195411

[42] E. Buks and M. P. Blencowe, "Decoherence and recoherence in a vibrating rf squid," Phys. Rev. B, vol. 74, p. 174504, Nov 2006. [Online]. Available: http://link.aps.org/doi/10.1103/PhysRevB.74.174504

[43] L. F. Wei, Y.-x. Liu, C. P. Sun, and F. Nori, "Probing tiny motions of nanomechanical resonators: Classical or quantum mechanical?" Phys. Rev. Lett., vol. 97, p. 237201, Dec 2006. [Online]. Available: http://link.aps.org/doi/10.1103/PhysRevLett.97.237201

[44] A. A. Clerk and D. W. Utami, "Using a qubit to measure photon-number statistics of a driven thermal oscillator," Phys. Rev. A, vol. 75, p. 042302, Apr 2007. [Online]. Available: http://link.aps.org/doi/10.1103/PhysRevA.75.042302

[45] J. Hauss, A. Fedorov, C. Hutter, A. Shnirman, and G. Schön, "Single-qubit lasing and cooling at the rabi frequency," Phys. Rev. Lett., vol. 100, p. 037003, Jan 2008. [Online]. Available: http://link.aps.org/doi/10.1103/PhysRevLett.100.037003

[46] D. Wahyu Utami and A. A. Clerk, "Entanglement dynamics in a dispersively coupled qubit-oscillator system," Phys. Rev. A, vol. 78, p. 042323, Oct 2008. [Online]. Available: http://link.aps.org/doi/10.1103/PhysRevA.78.042323

[47] I. Wilson-Rae, N. Nooshi, W. Zwerger, and T. J. Kippenberg, "Theory of ground state cooling of a mechanical oscillator using dynamical backaction," Phys. Rev. Lett., vol. 99, p. 093901, Aug 2007. [Online]. Available: http://link.aps.org/doi/10.1103/PhysRevLett.99.093901

[48] F. Marquardt, J. P. Chen, A. A. Clerk, and S. M. Girvin, "Quantum theory of cavity-assisted sideband cooling of mechanical motion," Phys. Rev. Lett., vol. 99, p. 093902, Aug 2007. [Online]. Available: http://link.aps.org/doi/10.1103/PhysRevLett.99.093902

[49] A. Schliesser, P. Del'Haye, N. Nooshi, K. J. Vahala, and T. J. Kippenberg, "Radiation pressure cooling of a micromechanical oscillator using dynamical backaction," Phys. Rev. Lett., vol. 97, p. 243905, Dec 2006. [Online]. Available: http://link.aps.org/doi/10.1103/PhysRevLett.97.243905

[50] S. Gigan, H. R. Böhm, M. Paternostro, F. Blaser, G. Langer, B. Hertzberg, K. Schwab, D. Bäuerle, M. Aspelmeyer, and A. Zeilinger, "Self-cooling of a micromirror by radiation pressure," Nature, 2006. [Online]. Available: http://www.nature.com/nature/journal/v444/n7115/abs/nature05273.html

[51] O. Arcizet, P. F. Cohadon, T. Briant, M. Pinard, and A. Heidmann, "Radiation-pressure cooling and optomechanical instability of a micromirror," Nature, vol. 444, no. 7115, pp. 71–74, Nov. 2006. [Online]. Available: http://dx.doi.org/10.1038/nature05244

[52] T. Rocheleau, T. Ndukum, C. Macklin, J. B. Hertzberg, A. A. Clerk, and K. C. Schwab, "Preparation and detection of a mechanical resonator near the ground state of motion," Nature, vol. 463, no. 7277, pp. 72–75, Jan. 2010. [Online]. Available: http://dx.doi.org/10.1038/nature08681

[53] J. D. Teufel, T. Donner, D. Li, J. W. Harlow, M. S. Allman, K. Cicak, A. J. Sirois, J. D. Whittaker, K. W. Lehnert, and R. W. Simmonds, "Sideband cooling of micromechanical motion to the quantum ground state," Nature, vol. 475, p. 359–363, 7/2011 2011. [Online]. Available: http://www.nature.com/nature/journal/v475/n7356/full/nature10261.html

[54] J. Chan, T. P. M. Alegre, A. H. Safavi-Naeini, J. T. Hill, A. Krause, S. Gröblacher, M. Aspelmeyer, and O. Painter, "Laser cooling of a nanomechanical oscillator into its quantum ground state," Nature, vol. 478, no. 7367, pp. 89–92, Oct. 2011. [Online]. Available: http://dx.doi.org/10.1038/nature10461

[55] A. H. Safavi-Naeini, J. Chan, J. T. Hill, T. P. M. Alegre, A. Krause, and O. Painter, "Observation of quantum motion of a nanomechanical resonator," Phys. Rev. Lett., vol. 108, p. 033602, Jan 2012. [Online]. Available: http://link.aps.org/doi/10.1103/PhysRevLett.108.033602

[56] A. J. Weinstein, C. U. Lei, E. E. Wollman, J. Suh, A. Metelmann, A. A. Clerk, and K. C. Schwab, "Observation and interpretation of motional sideband asymmetry in a quantum electromechanical device," Phys. Rev. X, vol. 4, p. 041003, Oct 2014. [Online]. Available: http://link.aps.org/doi/10.1103/PhysRevX.4.041003

[57] F. Lecocq, J. B. Clark, R. W. Simmonds, J. Aumentado, and J. D. Teufel, "Quantum nondemolition measurement of a nonclassical state of a massive object," Physical Review X, vol. 5, no. 4, p. 041037, 2015. [Online]. Available: http://link.aps.org/doi/10.1103/PhysRevX.5.041037

[58] E. E. Wollman, C. U. Lei, A. J. Weinstein, J. Suh, A. Kronwald, F. Marquardt, A. A. Clerk, and K. C. Schwab, "Quantum squeezing of motion in a mechanical resonator," Science, vol. 349, pp. 952–955, October 2015. [Online]. Available: http://www.sciencemag.org/cgi/doi/10.1126/science.aac5138

[59] J. M. Pirkkalainen, E. Damskägg, M. Brandt, F. Massel, and M. A. Sillanpää, "Squeezing of quantum noise of motion in a micromechanical resonator," Physical Review Letters, vol. 115, no. 24, p. 243601, 2015. [Online]. Available: http://link.aps.org/doi/10.1103/PhysRevLett.115.243601

[60] T. A. Palomaki, J. D. Teufel, R. W. Simmonds, and K. W. Lehnert, "Entangling mechanical motion with microwave fields," Science, vol. 342, pp. 710–713, October 2013. [Online]. Available: http://science.sciencemag.org/content/342/6159/710

[61] A. Reiserer and G. Rempe, "Cavity-based quantum networks with single atoms and optical photons," Rev. Mod. Phys., vol. 87, pp. 1379–1418, Dec 2015. [Online]. Available: http://link.aps.org/doi/10.1103/RevModPhys.87.1379

[62] A. Narla, S. Shankar, M. Hatridge, Z. Leghtas, K. M. Sliwa, E. Zalys-Geller, S. O. Mundhada, W. Pfaff, L. Frunzio, R. J. Schoelkopf, and M. H. Devoret, "Robust concurrent remote entanglement between two superconducting qubits," Phys. Rev. X, vol. 6, p. 031036, Sep 2016. [Online]. Available: http://link.aps.org/doi/10.1103/PhysRevX.6.031036

[63] C. Monroe, R. Raussendorf, A. Ruthven, K. R. Brown, P. Maunz, L.-M. Duan, and J. Kim, "Large-scale modular quantum-computer architecture with atomic memory and photonic interconnects," Phys. Rev. A, vol. 89, p. 022317, Feb 2014. [Online]. Available: http://link.aps.org/doi/10.1103/PhysRevA.89.022317

[64] T. A. Palomaki, J. W. Harlow, J. D. Teufel, R. W. Simmonds, and K. W. Lehnert, "Coherent state transfer between itinerant microwave fields and a mechanical oscillator." Nature, vol. 495, pp. 210–214, March 2013. [Online]. Available: http://www.nature.com/nature/journal/v495/n7440/full/nature11915.html

[65] R. W. Andrews, A. P. Reed, K. Cicak, J. D. Teufel, and K. W. Lehnert, "Quantum-enabled temporal and spectral mode conversion of microwave signals." Nature Communications, vol. 6, p. 10021, May 2015. [Online]. Available: http://dx.doi.org/10.1038/ncomms10021

[66] F. Lecocq, J. D. Teufel, J. Aumentado, and R. W. Simmonds, "Resolving the vacuum fluctuations of an optomechanical system using an artificial atom," Nature Physics, vol. 11, pp. 635–639, June 2015. [Online]. Available: http://dx.doi.org/10.1038/nphys3365

[67] F. Lecocq, J. B. Clark, R. W. Simmonds, J. Aumentado, and J. D. Teufel, "Mechanically mediated microwave frequency conversion in the quantum regime," Physical Review Letters, vol. 116, no. 4, p. 043601, 2016. [Online]. Available: http://link.aps.org/doi/10.1103/PhysRevLett.116.043601

[68] C. F. Ockeloen-Korppi, E. Damskägg, J. M. Pirkkalainen, T. T. Heikkilä, F. Massel, and M. A. Sillanpää, "Low-noise amplification and frequency conversion with a multiport microwave optomechanical device," Physical Review X, vol. 6, p. 041024, 2016. [Online]. Available: https://journals.aps.org/prx/abstract/10.1103/PhysRevX.6.041024

[69] U. Andersen, J. Neergaard-Nielsen, P. van Loock, and A. Furusawa, "Hybrid discrete- and continuous-variable quantum information," Nature Physics, vol. 11, no. 9, pp. 713–719, 2015. [Online]. Available: http://www.nature.com/nphys/journal/v11/n9/full/nphys3410.html

[70] I. L. Chuang and M. A. Nielsen, "Prescription for experimental determination of the dynamics of a quantum black box," Journal of Modern Optics, vol. 44, pp. 2455–2467, Nov. 1997. [Online]. Available: http://www.tandfonline.com/doi/abs/10.1080/09500349708231894

[71] C. Weedbrook, S. Pirandola, R. García-Patrón, N. J. Cerf, T. C. Ralph, J. H. Shapiro, and S. Lloyd, "Gaussian quantum information," Rev. Mod. Phys., vol. 84, pp. 621–669, May 2012. [Online]. Available: http://link.aps.org/doi/10.1103/RevModPhys.84.621

[72] S. D. Bartlett, B. C. Sanders, S. L. Braunstein, and K. Nemoto, "Efficient classical simulation of continuous variable quantum information processes." Physical Review Letters, vol. 88, no. 9, p. 097904, 2002. [Online]. Available: https://journals.aps.org/prl/abstract/10.1103/PhysRevLett.88.097904

[73] A. I. Lvovsky, H. Hansen, T. Aichele, O. Benson, J. Mlynek, and S. Schiller, "Quantum state reconstruction of the single-photon fock state," Phys. Rev. Lett., vol. 87, p. 050402, Jul 2001. [Online]. Available: http://link.aps.org/doi/10.1103/PhysRevLett.87.050402

[74] C. Galland, N. Sangouard, N. Piro, N. Gisin, and T. J. Kippenberg, "Heralded single-phonon preparation, storage, and readout in cavity optomechanics," Phys. Rev. Lett., vol. 112, p. 143602, Apr 2014. [Online]. Available: http://link.aps.org/doi/10.1103/PhysRevLett.112.143602

[75] J.-M. Pirkkalainen, S. U. Cho, J. Li, G. S. Paraoanu, P. J. Hakonen, and M. A. Sillanpää, "Hybrid circuit cavity quantum electrodynamics with a micromechanical resonator," Nature, vol. 494, pp. 211–215, Feb. 2013. [Online]. Available: http://www.nature.com/nature/journal/v494/n7436/full/nature11821.html

[76] J. D. Cohen, S. M. Meenehan, G. S. Maccabe, S. Gröblacher, A. H. Safavi-Naeini, F. Marsili, M. D. Shaw, and O. Painter, "Phonon counting and intensity interferometry of a nanomechanical resonator," Nature, vol. 520, pp. 522–525, Apr. 2015. [Online]. Available: http://www.nature.com/nature/journal/v520/n7548/full/nature14349.html

[77] R. Riedinger, S. Hong, R. A. Norte, J. A. Slater, J. Shang, A. G. Krause, V. Anant, M. Aspelmeyer, and S. Gröblacher, "Non-classical correlations between single photons and phonons from a mechanical oscillator," Nature, vol. 530, pp. 313 – 316, 2016. [Online]. Available: http://www.nature.com/nature/journal/v530/n7590/full/nature16536.html

[78] A. P. Reed, K. H. Mayer, J. D. Teufel, L. D. Burkhart, W. Pfaff, M. Reagor, L. Sletten, X. Ma, R. J. Schoelkopf, E. Knill, and K. W. Lehnert, "Faithful conversion of propagating quantum information to mechanical motion," ArXiv e-prints, Mar. 2017. [Online]. Available: https://arxiv.org/abs/1703.02548

[79] H. Paik, D. I. Schuster, L. S. Bishop, G. Kirchmair, G. Catelani, A. P. Sears, B. R. Johnson, M. J. Reagor, L. Frunzio, L. I. Glazman, S. M. Girvin, M. H. Devoret, and R. J. Schoelkopf, "Observation of high coherence in Josephson junction qubits measured in a three-dimensional circuit QED architecture," Physical Review Letters, vol. 107, no. 24, p. 240501, 2011. [Online]. Available: https://journals.aps.org/prl/abstract/10.1103/PhysRevLett.107.240501

[80] U. Akram, N. Kiesel, M. Aspelmeyer, and G. J. Milburn, "Single-photon opto-mechanics in the strong coupling regime," New Journal of Physics, vol. 12, 2010. [Online]. Available: http://iopscience.iop.org/article/10.1088/1367-2630/12/8/083030

[81] F. Khalili, S. Danilishin, H. Miao, H. Müller-Ebhardt, H. Yang, and Y. Chen, "Preparing a mechanical oscillator in non-gaussian quantum states," Phys. Rev. Lett., vol. 105, p. 070403, Aug 2010. [Online]. Available: http://link.aps.org/doi/10.1103/PhysRevLett.105.070403

[82] O. Romero-Isart, M. L. Juan, R. Quidant, and J. I. Cirac, "Toward quantum superposition of living organisms," New Journal of Physics, vol. 12, no. 3, p. 033015, 2010. [Online]. Available: http://stacks.iop.org/1367-2630/12/i=3/a=033015

[83] M. Hofheinz, E. M. Weig, M. Ansmann, R. C. Bialczak, E. Lucero, M. Neeley, A. D. O'Connell, H. Wang, J. M. Martinis, and A. N. Cleland, "Generation of Fock states in a superconducting quantum circuit," Nature, vol. 454, pp. 310–314, 2008. [Online]. Available: http://www.nature.com/nature/journal/v454/n7202/abs/nature07136.html

[84] M. Hofheinz, H. Wang, M. Ansmann, R. C. Bialczak, E. Lucero, M. Neeley, A. D. O'Connell, D. Sank, J. Wenner, J. M. Martinis, and A. N. Cleland, "Synthesizing arbitrary quantum states in a superconducting resonator," Nature, vol. 459, no. 7246, pp. 546–549, 2009. [Online]. Available: http://dx.doi.org/10.1038/nature08005

[85] B. Vlastakis, G. Kirchmair, Z. Leghtas, S. E. Nigg, L. Frunzio, S. M. Girvin, M. Mirrahimi, M. H. Devoret, and R. J. Schoelkopf, "Deterministically Encoding Quantum Information Using 100-Photon Schrödinger Cat States," Science, vol. 342, no. 6158, pp. 607–610, 2013. [Online]. Available: http://science.sciencemag.org/content/342/6158/607

[86] W. Pfaff, C. J. Axline, L. D. Burkhart, U. Vool, P. Reinhold, L. Frunzio, L. Jiang, M. H. Devoret, and R. J. Schoelkopf, "Schrödinger's catapult: Launching multiphoton quantum states from a microwave cavity memory," ArXiv e-prints, Dec. 2016. [Online]. Available: https://arxiv.org/abs/1612.05238

[87] M. A. Nielsen, "A simple formula for the average gate fidelity of a quantum dynamical operation," Physics Letters A, vol. 303, pp. 249–252, 2002. [Online]. Available: https://arxiv.org/abs/quant-ph/0205035

[88] V. Scarani, H. Bechmann-Pasquinucci, N. J. Cerf, M. Dušek, N. Lütkenhaus, and M. Peev, "The security of practical quantum key distribution," Rev. Mod. Phys., vol. 81, pp. 1301–1350, Sep 2009. [Online]. Available: http://link.aps.org/doi/10.1103/RevModPhys.81.1301

[89] T. D. Ladd, F. Jelezko, R. Laflamme, Y. Nakamura, C. Monroe, and J. L. O'Brien, "Quantum computers." Nature, vol. 464, no. 7285, pp. 45–53, 2010. [Online]. Available: http://dx.doi.org/10.1038/nature08812

[90] E. Knill, G. Milburn, and R. Laflamme, "A scheme for efficient quantum computation with linear optics," Nature, vol. 409, no. January, pp. 46–52, 2001. [Online]. Available: http://www.nature.com/nature/journal/v409/n6816/full/409046a0.html

[91] H. Häffner, C. F. Roos, and R. Blatt, "Quantum computing with trapped ions," Phys. Rep., vol. 469, pp. 155–203, Dec. 2008. [Online]. Available: https://arxiv.org/abs/0809.4368

[92] L. M. K. Vandersypen and I. L. Chuang, "Nmr techniques for quantum control and computation," Rev. Mod. Phys., vol. 76, pp. 1037–1069, Jan 2005. [Online]. Available: http://link.aps.org/doi/10.1103/RevModPhys.76.1037

[93] R. Hanson, L. P. Kouwenhoven, J. R. Petta, S. Tarucha, and L. M. K. Vandersypen, "Spins in few-electron quantum dots," Rev. Mod. Phys., vol. 79, pp. 1217–1265, Oct 2007. [Online]. Available: http://link.aps.org/doi/10.1103/RevModPhys.79.1217

[94] F. A. Zwanenburg, A. S. Dzurak, A. Morello, M. Y. Simmons, L. C. L. Hollenberg, G. Klimeck, S. Rogge, S. N. Coppersmith, and M. A. Eriksson, "Silicon quantum electronics," Rev. Mod. Phys., vol. 85, pp. 961–1019, Jul 2013. [Online]. Available: http://link.aps.org/doi/10.1103/RevModPhys.85.961

[95] I. Bloch, "Quantum coherence and entanglement with ultracold atoms in optical lattices," Nature, vol. 453, no. 7198, pp. 1016–1022, Jun. 2008. [Online]. Available: http://dx.doi.org/10.1038/nature07126

[96] M. H. Devoret and R. S. Schoelkopf, "Superconducting Circuits for Quantum Information: An Outlook," Science, vol. 339, no. 6124, pp. 1169 – 1173, 2013. [Online]. Available: http://science.sciencemag.org/content/339/6124/1169

[97] H. Baher, Analog and Digital Signal Processing. Wiley, 1990.

[98] C. Gerry and P. Knight, Introductory Quantum Optics. Cambridge University Press, 2004.

[99] D. Morin, Classical Mechanics. New York, USA: Cambridge University Press, 2008.

[100] W. H. Louisell, Coupled Mode and Parametric Electronics. Wiley, 1960.

[101] R. Shankar, Principles of quantum mechanics. New York, NY: Plenum, 1980.

[102] J. J. Sakurai, Modern quantum mechanics; rev. ed. Reading, MA: Addison-Wesley, 1994.

[103] J. Weber, "Fluctuation dissipation theorem," Phys. Rev., vol. 101, pp. 1620–1626, Mar 1956. [Online]. Available: http://link.aps.org/doi/10.1103/PhysRev.101.1620

[104] Y. Fukui and T. Morita, "Derivation of the stationary generalized Langevin equation," Journal of Physics A Mathematical General, vol. 4, pp. 477–490, Jul. 1971. [Online]. Available: http://iopscience.iop.org/article/10.1088/0305-4470/4/4/011

[105] D. S. Lemons and A. Gythiel, "Paul Langevin's 1908 paper 'On the Theory of Brownian Motion' ['Sur la théorie du mouvement brownien,' C. R. Acad. Sci. (Paris) 146, 530–533 (1908)]," American Journal of Physics, vol. 65, no. 11, pp. 1079–1081, 1997. [Online]. Available: http://dx.doi.org/10.1119/1.18725

[106] M. J. Collett and C. W. Gardiner, "Squeezing of intracavity and traveling-wave light fields produced in parametric amplification," Phys. Rev. A, vol. 30, pp. 1386–1391, Sep 1984. [Online]. Available: http://link.aps.org/doi/10.1103/PhysRevA.30.1386

[107] G. Lindblad, "On the generators of quantum dynamical semigroups," Comm. Math. Phys., vol. 48, no. 2, pp. 119–130, 1976. [Online]. Available: http://projecteuclid.org/euclid.cmp/1103899849

[108] C. Gardiner and P. Zoller, Quantum Noise, 3rd ed. 6020 Innsbruck, Austria: Springer, 2004.

[109] D. Morin, Quantum Optics. Berlin, Germany: Springer, 2008.

[110] S. Haroche and J. M. Raimond, Exploring the Quantum: Atoms, Cavities, and Photons. Oxford: Oxford Univ. Press, 2006.

[111] J. P. Reithmaier, G. Sek, A. Löffler, C. Hofmann, S. Kuhn, S. Reitzenstein, L. V. Keldysh, V. D. Kulakovskii, T. L. Reinecke, and A. Forchel, "Strong coupling in a single quantum dot-semiconductor microcavity system," Nature, vol. 432, no. 7014, pp. 197–200, Nov. 2004. [Online]. Available: http://dx.doi.org/10.1038/nature02969

[112] T. Yoshie, A. Scherer, J. Hendrickson, G. Khitrova, C. Ell, O. B. Shchekin, and D. G. Deppe, "Vacuum Rabi splitting with a single quantum dot in a photonic crystal nanocavity," Nature, vol. 432, pp. 200–203, Nov. 2004. [Online]. Available: http://www.nature.com/nature/journal/v432/n7014/abs/nature03119.html

[113] E. K. Irish and K. Schwab, "Quantum measurement of a coupled nanomechanical resonatorcooper-pair box system," Phys. Rev. B, vol. 68, p. 155311, Oct 2003. [Online]. Available: http://link.aps.org/doi/10.1103/PhysRevB.68.155311

[114] A. Wallraff, D. Schuster, A. Blais, L. Frunzio, R. Huang, J. Majer, S. Kumar, S. Girvin, and R. Schoelkopf, "Strong coupling of a single photon to a superconducting qubit using circuit quantum electrodynamics," Nature, vol. 431, no. 7005, pp. 162–167, 2004. [Online]. Available: http://www.nature.com/nature/journal/v431/n7005/abs/nature02851.html

[115] A. Blais, R.-S. Huang, A. Wallraff, S. M. Girvin, and R. J. Schoelkopf, "Cavity quantum electrodynamics for superconducting electrical circuits: An architecture for quantum computation," Physical Review A, vol. 69, no. 6, p. 062320, June 2004. [Online]. Available: https://journals.aps.org/pra/abstract/10.1103/PhysRevA.75.032329

[116] D. I. Schuster, A. A. Houck, J. A. Schreier, A. Wallraff, J. M. Gambetta, A. Blais, L. Frunzio, J. Majer, B. Johnson, M. H. Devoret, S. M. Girvin, and R. J. Schoelkopf, "Resolving photon number states in a superconducting circuit." Nature, vol. 445, no. 7127, pp. 515–8, feb 2007. [Online]. Available: http://www.nature.com/nature/journal/v445/n7127/abs/nature05461.html

[117] A. Wallraff, D. I. Schuster, A. Blais, J. M. Gambetta, J. Schreier, L. Frunzio, M. H. Devoret, S. M. Girvin, and R. J. Schoelkopf, "Sideband transitions and two-tone spectroscopy of a superconducting qubit strongly coupled to an on-chip cavity," Phys. Rev. Lett., vol. 99, p. 050501, Jul 2007. [Online]. Available: http://link.aps.org/doi/10.1103/PhysRevLett.99.050501

[118] P. J. Leek, S. Filipp, P. Maurer, M. Baur, R. Bianchetti, J. M. Fink, M. Göppl, L. Steffen, and A. Wallraff, "Using sideband transitions for two-qubit operations in superconducting circuits," Phys. Rev. B, vol. 79, p. 180511, May 2009. [Online]. Available: http://link.aps.org/doi/10.1103/PhysRevB.79.180511

[119] W. F. Kindel, M. D. Schroer, and K. W. Lehnert, "Generation and efficient measurement of single photons from fixed-frequency superconducting qubits," Physical Review A, vol. 93, p. 033817, 2016. [Online]. Available: https://journals.aps.org/pra/abstract/10.1103/PhysRevA.93.033817

[120] M. J. Reagor, "Superconducting cavities for circuit quantum electrodynamics," Ph.D. dissertation, Yale University, 2015.

[121] C. Eichler, D. Bozyigit, C. Lang, L. Steffen, J. Fink, and A. Wallraff, "Experimental state tomography of itinerant single microwave photons," Phys. Rev. Lett., vol. 106, p. 220503, Jun 2011. [Online]. Available: http://link.aps.org/doi/10.1103/PhysRevLett.106.220503

[122] A. I. Lvovsky and M. G. Raymer, "Continuous-variable optical quantum-state tomography," Rev. Mod. Phys., vol. 81, pp. 299–332, Mar 2009. [Online]. Available: http://link.aps.org/doi/10.1103/RevModPhys.81.299

[123] U. Leonhardt, Measuring the Quantum State of Light. Cambridge: Cambridge University Press, 1997.

[124] C. Eichler, D. Bozyigit, and A. Wallraff, "Characterizing quantum microwave radiation and its entanglement with superconducting qubits using linear detectors," Phys. Rev. A, vol. 86, p. 032106, Sep 2012. [Online]. Available: http://link.aps.org/doi/10.1103/PhysRevA.86.032106

[125] M. A. Castellanos-Beltran, K. D. Irwin, G. C. Hilton, L. R. Vale, and K. W. Lehnert, "Amplification and squeezing of quantum noise with a tunable josephson metamaterial," Nature Physics, vol. 4, pp. 929 – 931, 12/2008 2008. [Online]. Available: http://www.nature.com/nphys/journal/v4/n12/full/nphys1090.html

[126] C. M. Caves, J. Combes, Z. Jiang, and S. Pandey, "Quantum limits on phase-preserving linear amplifiers," Physical Review A, vol. 86, no. 6, p. 063802, 2012. [Online]. Available: https://journals.aps.org/pra/abstract/10.1103/PhysRevA.86.063802

[127] U. Leonhardt and H. Paul, "Phase measurement and Q function," Phys. Rev. A, vol. 47, pp. R2460–R2463, Apr 1993. [Online]. Available: http://link.aps.org/doi/10.1103/PhysRevA.47.R2460

[128] M. A. Nielsen and I. L. Chuang, Quantum Computation and Quantum Information, 10th ed. New York, NY, USA: Cambridge University Press, 2011.

[129] Z. Hradil, "Quantum-state estimation," Phys. Rev. A, vol. 55, pp. R1561–R1564, Mar 1997. [Online]. Available: http://link.aps.org/doi/10.1103/PhysRevA.55.R1561

[130] J. Řeháček, Z. c. v. Hradil, E. Knill, and A. I. Lvovsky, "Diluted maximum-likelihood algorithm for quantum tomography," Phys. Rev. A, vol. 75, p. 042108, Apr 2007. [Online]. Available: http://link.aps.org/doi/10.1103/PhysRevA.75.042108

[131] A. A. Clerk, M. H. Devoret, S. M. Girvin, F. Marquardt, and R. J. Schoelkopf, "Introduction to quantum noise, measurement, and amplification," Rev. Mod. Phys., vol. 82, pp. 1155–1208, Apr 2010. [Online]. Available: https://journals.aps.org/rmp/abstract/10.1103/RevModPhys.82.1155

[132] A. Roy and M. Devoret, "Introduction to parametric amplification of quantum signals with Josephson circuits," Comptes Rendus Physique, vol. 17, pp. 740–755, Aug. 2016. [Online]. Available: http://www.sciencedirect.com/science/article/pii/S1631070516300640

[133] M. Devoret, B. Huard, R. Schoelkopf, and L. F. Cugliandolo, Quantum Machines: Measurement and Control of Engineered Quantum Systems. Oxford, 2014.

[134] C. W. Gardiner and M. J. Collett, "Input and output in damped quantum systems: Quantum stochastic differential equations and the master equation," Phys. Rev. A, vol. 31, pp. 3761–3774, Jun 1985. [Online]. Available: http://link.aps.org/doi/10.1103/PhysRevA.31.3761

[135] H. A. Haus and J. A. Mullen, "Quantum noise in linear amplifiers," Phys. Rev., vol. 128, pp. 2407–2413, Dec 1962. [Online]. Available: https://link.aps.org/doi/10.1103/PhysRev.128.2407

[136] J. D. Teufel, D. Li, M. S. Allman, K. Cicak, A. J. Sirois, J. D. Whittaker, and R. W. Simmonds, "Circuit cavity electromechanics in the strong-coupling regime," Nature, vol. 471, pp. 204–208, Mar. 2011. [Online]. Available: http://www.nature.com/nature/journal/v471/n7337/full/nature09898.html

[137] A. Dorsel, J. D. McCullen, P. Meystre, E. Vignes, and H. Walther, "Optical bistability and mirror confinement induced by radiation pressure," Phys. Rev. Lett., vol. 51, pp. 1550–1553, Oct 1983. [Online]. Available: http://link.aps.org/doi/10.1103/PhysRevLett.51.1550

[138] A. Gozzini, F. Maccarrone, F. Mango, I. Longo, and S. Barbarino, "Light-pressure bistability at microwave frequencies," J. Opt. Soc. Am. B, vol. 2, no. 11, pp. 1841–1845, Nov 1985. [Online]. Available: http://josab.osa.org/abstract.cfm?URI=josab-2-11-1841

[139] P. Meystre, E. M. Wright, J. D. McCullen, and E. Vignes, "Theory of radiation-pressure-driven interferometers," J. Opt. Soc. Am. B, vol. 2, no. 11, pp. 1830–1840, Nov 1985. [Online]. Available: http://josab.osa.org/abstract.cfm?URI=josab-2-11-1830

[140] C. Fabre, M. Pinard, S. Bourzeix, A. Heidmann, E. Giacobino, and S. Reynaud, "Quantum-noise reduction using a cavity with a movable mirror," Phys. Rev. A, vol. 49, pp. 1337–1343, Feb 1994. [Online]. Available: http://link.aps.org/doi/10.1103/PhysRevA.49.1337

[141] C. K. Law, "Interaction between a moving mirror and radiation pressure: A hamiltonian formulation," Phys. Rev. A, vol. 51, pp. 2537–2541, Mar 1995. [Online]. Available: http://link.aps.org/doi/10.1103/PhysRevA.51.2537

[142] A. Schliesser, R. Rivière, G. Anetsberger, O. Arcizet, and T. J. Kippenberg, "Resolved-sideband cooling of a micro-mechanical oscillator," Nature Physics, pp. 415–419, 2008. [Online]. Available: http://www.nature.com/nphys/journal/v4/n5/full/nphys939.html

[143] J. Zhang, K. Peng, and S. L. Braunstein, "Quantum-state transfer from light to macroscopic oscillators," Phys. Rev. A, vol. 68, p. 013808, Jul 2003. [Online]. Available: http://link.aps.org/doi/10.1103/PhysRevA.68.013808

[144] J. W. Harlow, "Microwave electromechanics: Measuring and manipulating the quantum state of a macroscopic mechanical oscillator," Ph.D. dissertation, University of Colorado, Boulder, 2013.

[145] M. M. Nieto and D. R. Truax, "Holstein-Primakoff/Bogoliubov Transformations and the Multiboson System," Fortschritte der Physik, vol. 45, pp. 145–156, 1997. [Online]. Available: https://arxiv.org/abs/quant-ph/9506025

[146] C. M. Caves and B. L. Schumaker, "New formalism for two-photon quantum optics. i. quadrature phases and squeezed states," Phys. Rev. A, vol. 31, pp. 3068–3092, May 1985. [Online]. Available: http://link.aps.org/doi/10.1103/PhysRevA.31.3068

[147] B. L. Schumaker and C. M. Caves, "New formalism for two-photon quantum optics. ii. mathematical foundation and compact notation," Phys. Rev. A, vol. 31, pp. 3093–3111, May 1985. [Online]. Available: http://link.aps.org/doi/10.1103/PhysRevA.31.3093

[148] B. L. Schumaker, "Quantum mechanical pure states with gaussian wave functions," Physics Reports, vol. 135, no. 6, pp. 317 – 408, 1986. [Online]. Available: http://www.sciencedirect.com/science/article/pii/0370157386901791

[149] R. W. Andrews, "Quantum signal processing with mechanical oscillators," Ph.D. dissertation, University of Colorado, Boulder, 2015.

[150] K. Cicak, D. Li, J. A. Strong, M. S. Allman, F. Altomare, A. J. Sirois, J. D. Whittaker, J. D. Teufel, and R. W. Simmonds, "Low-loss superconducting resonant circuits using vacuum-gap-based microwave components," Applied Physics Letters, vol. 96, no. 9, p. 093502, 2010. [Online]. Available: http://dx.doi.org/10.1063/1.3304168

[151] D. M. Pozar, Microwave engineering; 3rd ed. Hoboken, NJ: Wiley, 2005.

[152] J. L. O'Brien, A. Furusawa, and J. Vučković, "Photonic quantum technologies," Nature Photonics, vol. 3, no. 12, pp. 687–695, 2010. [Online]. Available: http://www.nature.com/nphoton/journal/v3/n12/abs/nphoton.2009.229.html

[153] T. E. Northup and R. Blatt, "Quantum information transfer using photons," Nat Photon, vol. 8, no. 5, pp. 356–363, 2014. [Online]. Available: http://dx.doi.org/10.1038/nphoton.2014.53

[154] A. A. Houck, D. I. Schuster, J. M. Gambetta, J. A. Schreier, B. R. Johnson, J. M. Chow, L. Frunzio, J. Majer, M. H. Devoret, S. M. Girvin, and R. J. Schoelkopf, "Generating single microwave photons in a circuit," Nature, vol. 449, no. 7160, pp. 328–331, Sep. 2007. [Online]. Available: http://dx.doi.org/10.1038/nature06126

[155] D. Bozyigit, C. Lang, L. Steffen, J. M. Fink, C. Eichler, M. Baur, R. Bianchetti, P. J. Leek, S. Filipp, M. P. da Silva, A. Blais, and A. Wallraff, "Antibunching of microwave-frequency photons observed in correlation measurements using linear detectors," Nature Physics, vol. 7, no. 2, pp. 154–158, 2011. [Online]. Available: http://dx.doi.org/10.1038/nphys1845

[156] Y.-F. Chen, D. Hover, S. Sendelbach, L. Maurer, S. T. Merkel, E. J. Pritchett, F. K. Wilhelm, and R. McDermott, "Microwave photon counter based on josephson junctions," Phys. Rev. Lett., vol. 107, p. 217401, Nov 2011. [Online]. Available: https://link.aps.org/doi/10.1103/PhysRevLett.107.217401

[157] C. Lang, C. Eichler, L. Steffen, J. M. Fink, M. J. Woolley, A. Blais, and A. Wallraff, "Correlations, indistinguishability and entanglement in Hong-Ou-Mandel experiments at microwave frequencies," Nature Physics, vol. 9, no. 5, pp. 1–4, 2013. [Online]. Available: http://dx.doi.org/10.1038/nphys2612

[158] Y. Yin, Y. Chen, D. Sank, P. J. J. O'Malley, T. C. White, R. Barends, J. Kelly, E. Lucero, M. Mariantoni, A. Megrant, C. Neill, A. Vainsencher, J. Wenner, A. N. Korotkov, A. N. Cleland, and J. M. Martinis, "Catch and release of microwave photon states," Phys. Rev. Lett., vol. 110, p. 107001, Mar 2013. [Online]. Available: http://link.aps.org/doi/10.1103/PhysRevLett.110.107001

[159] M. Pechal, L. Huthmacher, C. Eichler, S. Zeytinoğlu, A. A. Abdumalikov, S. Berger, A. Wallraff, and S. Filipp, "Microwave-controlled generation of shaped single photons in circuit quantum electrodynamics," Phys. Rev. X, vol. 4, p. 041010, Oct 2014. [Online]. Available: http://link.aps.org/doi/10.1103/PhysRevX.4.041010

[160] Z. H. Peng, S. E. de Graaf, J. S. Tsai, and O. V. Astafiev, "Tuneable on-demand single-photon source in the microwave range," Nature Communications, vol. 7, p. 12588, Aug. 2016. [Online]. Available: http://www.nature.com/doifinder/10.1038/ncomms12588

[161] K. M. Gheri, K. Ellinger, T. Pellizzari, and P. Zoller, "Photon-Wavepackets as Flying Quantum Bits," Fortschritte der Physik, vol. 46, p. 401, 1998.

[162] J. Clarke and F. K. Wilhelm, "Superconducting quantum bits," Nature, vol. 453, no. 7198, pp. 1031–42, jun 2008. [Online]. Available: http://www.nature.com/nature/journal/v453/n7198/abs/nature07128.html

[163] J. Q. You and F. Nori, "Atomic physics and quantum optics using superconducting circuits," Nature, vol. 474, pp. 589–597, Jun. 2011. [Online]. Available: http://www.nature.com/nature/journal/v474/n7353/full/nature10122.html

[164] G. Kirchmair, B. Vlastakis, Z. Leghtas, S. E. Nigg, H. Paik, E. Ginossar, M. Mirrahimi, L. Frunzio, S. M. Girvin, and R. J. Schoelkopf, "Observation of quantum state collapse and revival due to the single-photon Kerr effect." Nature, vol. 495, no. 7440, pp. 205–9, mar 2013. [Online]. Available: http://www.nature.com/nature/journal/v495/n7440/full/nature11902.html

[165] B. E. A. Saleh and M. Carl Teich, Fundamentals of Photonics. New York, USA: Wiley, 2007.

[166] K. K. Likharev, Dynamics of Josephson Junctions and Circuits. Gordon and Breach Publications, 1986.

[167] T. V. Duzer and C. W. Turner, Principles of Superconductive Devices and Circuits. Prentice Hall, 1999.

[168] B. D. Josephson, "Possible new effects in superconductive tunnelling," Physics Letters, vol. 1, pp. 251–253, Jul. 1962. [Online]. Available: http://www.sciencedirect.com/science/article/pii/0031916362913690

[169] R. P. Feynman, R. B. Leighton, and M. Sands, The Feynman lectures on physics. Vol. 3: Quantum mechanics. Addison-Wesley Publishing Co., Inc., Reading, Mass.-London, 1965. [Online]. Available: http://www.feynmanlectures.caltech.edu/III_21.html

[170] J. D. Jackson, Classical electrodynamics, 3rd ed. New York, NY: Wiley, 1999.

[171] J. Koch, T. M. Yu, J. Gambetta, A. A. Houck, D. I. Schuster, J. Majer, A. Blais, M. H. Devoret, S. M. Girvin, and R. J. Schoelkopf, "Charge-insensitive qubit design derived from the cooper pair box," Phys. Rev. A, vol. 76, p. 042319, Oct 2007. [Online]. Available: http://link.aps.org/doi/10.1103/PhysRevA.76.042319

[172] J. A. Schreier, A. A. Houck, J. Koch, D. I. Schuster, B. R. Johnson, J. M. Chow, J. M. Gambetta, J. Majer, L. Frunzio, M. H. Devoret, S. M. Girvin, and R. J. Schoelkopf, "Suppressing charge noise decoherence in superconducting charge qubits," Phys. Rev. B, vol. 77, p. 180502, May 2008. [Online]. Available: http://link.aps.org/doi/10.1103/PhysRevB.77.180502

[173] A. A. Houck, J. Koch, M. H. Devoret, S. M. Girvin, and R. J. Schoelkopf, "Life after charge noise: recent results with transmon qubits," Quantum Information Processing, vol. 8, no. 2, pp. 105–115, 2009. [Online]. Available: http://dx.doi.org/10.1007/s11128-009-0100-6

[174] V. Bouchiat, D. Vion, P. Joyez, D. Esteve, and M. H. Devoret, "Quantum Coherence with a Single Cooper Pair," Physica Scripta Volume T, vol. 76, pp. 165–170, 1998. [Online]. Available: http://dx.doi.org/10.1238/physica.topical.076a00165

[175] Y. Nakamura, Y. A. Pashkin, and J. S. Tsai, "Coherent control of macroscopic quantum states in a single-Cooper-pair box," Nature, vol. 398, no. April, p. 786, 1999. [Online]. Available: https://www.nature.com/nature/journal/v398/n6730/full/398786a0.html

[176] K. W. Lehnert, K. Bladh, L. F. Spietz, D. Gunnarsson, D. I. Schuster, P. Delsing, and R. J. Schoelkopf, "Measurement of the excited-state lifetime of a microelectronic circuit," Phys. Rev. Lett., vol. 90, p. 027002, Jan 2003. [Online]. Available: http://link.aps.org/doi/10.1103/PhysRevLett.90.027002

[177] R. Barends, J. Kelly, A. Megrant, D. Sank, E. Jeffrey, Y. Chen, Y. Yin, B. Chiaro, J. Mutus, C. Neill, P. O'Malley, P. Roushan, J. Wenner, T. C. White, A. N. Cleland, and J. M. Martinis, "Coherent josephson qubit suitable for scalable quantum integrated circuits," Phys. Rev. Lett., vol. 111, p. 080502, Aug 2013. [Online]. Available: http://link.aps.org/doi/10.1103/PhysRevLett.111.080502

[178] A. Wallraff, D. I. Schuster, A. Blais, L. Frunzio, J. Majer, M. H. Devoret, S. M. Girvin, and R. J. Schoelkopf, "Approaching unit visibility for control of a superconducting qubit with dispersive readout," Phys. Rev. Lett., vol. 95, p. 060501, Aug 2005. [Online]. Available: http://link.aps.org/doi/10.1103/PhysRevLett.95.060501

[179] C. Rigetti, J. M. Gambetta, S. Poletto, B. L. T. Plourde, J. M. Chow, A. D. Córcoles, J. A. Smolin, S. T. Merkel, J. R. Rozen, G. A. Keefe, M. B. Rothwell, M. B. Ketchen, and M. Steffen, "Superconducting qubit in a waveguide cavity with a coherence time approaching 0.1 ms," Phys. Rev. B, vol. 86, p. 100506, Sep 2012. [Online]. Available: http://link.aps.org/doi/10.1103/PhysRevB.86.100506

[180] M. Reagor, W. Pfaff, C. Axline, R. W. Heeres, N. Ofek, K. Sliwa, E. Holland, C. Wang, J. Blumoff, K. Chou, M. J. Hatridge, L. Frunzio, M. H. Devoret, L. Jiang, and R. J. Schoelkopf, "Quantum memory with millisecond coherence in circuit QED," Phys. Rev. B, vol. 94, p. 014506, Jul 2016. [Online]. Available: http://link.aps.org/doi/10.1103/PhysRevB.94.014506

[181] S. E. Nigg, H. Paik, B. Vlastakis, G. Kirchmair, S. Shankar, L. Frunzio, M. H. Devoret, R. J. Schoelkopf, and S. M. Girvin, "Black-box superconducting circuit quantization," Phys. Rev. Lett., vol. 108, p. 240502, Jun 2012. [Online]. Available: http://link.aps.org/doi/10.1103/PhysRevLett.108.240502

[182] M. D. Reed, L. DiCarlo, B. R. Johnson, L. Sun, D. I. Schuster, L. Frunzio, and R. J. Schoelkopf, "High-Fidelity Readout in Circuit Quantum Electrodynamics Using the Jaynes-Cummings Nonlinearity," Phys. Rev. Lett., vol. 105, p. 173601, Oct 2010. [Online]. Available: http://link.aps.org/doi/10.1103/PhysRevLett.105.173601

[183] L. S. Bishop, E. Ginossar, and S. M. Girvin, "Response of the Strongly Driven Jaynes-Cummings Oscillator," Phys. Rev. Lett., vol. 105, p. 100505, Sep 2010. [Online]. Available: http://link.aps.org/doi/10.1103/PhysRevLett.105.100505

[184] A. Palacios-Laloy, F. Mallet, F. Nguyen, P. Bertet, D. Vion, D. Esteve, and A. N. Korotkov, "Experimental violation of a Bell's inequality in time with weak measurement," Nature Physics, vol. 6, no. 6, pp. 442–447, Apr. 2010. [Online]. Available: http://dx.doi.org/10.1038/nphys1641

[185] R. Vijay, D. H. Slichter, and I. Siddiqi, "Observation of quantum jumps in a superconducting artificial atom," Phys. Rev. Lett., vol. 106, p. 110502, Mar 2011. [Online]. Available: http://link.aps.org/doi/10.1103/PhysRevLett.106.110502

[186] M. Hatridge, S. Shankar, M. Mirrahimi, F. Schackert, K. Geerlings, T. Brecht, K. M. Sliwa, B. Abdo, L. Frunzio, S. M. Girvin, R. J. Schoelkopf, and M. H. Devoret, "Quantum Back-Action of an Individual Variable-Strength Measurement," Science (New York, N.Y.), vol. 339, no. 6116, pp. 178–181, 2013. [Online]. Available: http://www.sciencemag.org/cgi/doi/10.1126/science.1226897

[187] D. Ristè, J. G. van Leeuwen, H.-S. Ku, K. W. Lehnert, and L. DiCarlo, "Initialization by measurement of a superconducting quantum bit circuit," Phys. Rev. Lett., vol. 109, p. 050507, Aug 2012. [Online]. Available: http://link.aps.org/doi/10.1103/PhysRevLett.109.050507

[188] D. Ristè, C. C. Bultink, K. W. Lehnert, and L. DiCarlo, "Feedback control of a solid-state qubit using high-fidelity projective measurement," Phys. Rev. Lett., vol. 109, p. 240502, Dec 2012. [Online]. Available: http://link.aps.org/doi/10.1103/PhysRevLett.109.240502

[189] M. D. Schroer, M. H. Kolodrubetz, W. F. Kindel, M. Sandberg, J. Gao, M. R. Vissers, D. P. Pappas, A. Polkovnikov, and K. W. Lehnert, "Measuring a topological transition in an artificial spin-1/2 system," Phys. Rev. Lett., vol. 113, p. 050402, Jul 2014. [Online]. Available: http://link.aps.org/doi/10.1103/PhysRevLett.113.050402

[190] V. B. Braginsky, Y. I. Vorontsov, and K. S. Thorne, "Quantum Nondemolition Measurement," Science, vol. 209, p. 547, 1980.

[191] N. Boulant, G. Ithier, P. Meeson, F. Nguyen, D. Vion, D. Esteve, I. Siddiqi, R. Vijay, C. Rigetti, F. Pierre, and M. Devoret, "Quantum nondemolition readout using a josephson bifurcation amplifier," Phys. Rev. B, vol. 76, p. 014525, Jul 2007. [Online]. Available: http://link.aps.org/doi/10.1103/PhysRevB.76.014525

[192] R. Bianchetti, S. Filipp, M. Baur, J. M. Fink, M. Göppl, P. J. Leek, L. Steffen, A. Blais, and A. Wallraff, "Dynamics of dispersive single-qubit readout in circuit quantum electrodynamics," Phys. Rev. A, vol. 80, p. 043840, Oct 2009. [Online]. Available: http://link.aps.org/doi/10.1103/PhysRevA.80.043840

[193] J. Gambetta, A. Blais, M. Boissonneault, A. A. Houck, D. I. Schuster, and S. M. Girvin, "Quantum trajectory approach to circuit QED: Quantum jumps and the Zeno effect," Phys. Rev. A, vol. 77, p. 012112, Jan 2008. [Online]. Available: http://link.aps.org/doi/10.1103/PhysRevA.77.012112

[194] W. F. Kindel, "Generation and efficient measurement of single photons using superconducting circuits," Ph.D. dissertation, University of Colorado, Boulder, 2015.

[195] K. L. Geerlings, "Improving coherence of superconducting qubits and resonators," Ph.D. dissertation, Yale University, 2013.

[196] C. J. Foot, Atomic Physics, 1st ed. Oxford University Press, USA, Feb. 2005.

[197] A. D. Córcoles, J. M. Chow, J. M. Gambetta, C. Rigetti, J. R. Rozen, G. A. Keefe, M. B. Rothwell, M. B. Ketchen, and M. Steffen, "Protecting superconducting qubits from radiation," Applied Physics Letters, vol. 99, no. 18, p. 181906, 2011. [Online]. Available: http://dx.doi.org/10.1063/1.3658630

[198] J. E. Johnson, C. Macklin, D. H. Slichter, R. Vijay, E. B. Weingarten, J. Clarke, and I. Siddiqi, "Heralded state preparation in a superconducting qubit," Phys. Rev. Lett., vol. 109, p. 050506, Aug 2012. [Online]. Available: http://link.aps.org/doi/10.1103/PhysRevLett.109.050506

[199] G. B. P., Advanced Kalman Filtering, Least-Squares and Modeling: A Practical Handbook. New York: John Wiley and Sons, 2011.

[200] C. H. Bennett, G. Brassard, C. Crépeau, R. Jozsa, A. Peres, and W. K. Wootters, "Teleporting an unknown quantum state via dual classical and Einstein-Podolsky-Rosen channels," Physical Review Letters, vol. 70, no. 13, p. 1895, 1993. [Online]. Available: https://journals.aps.org/prl/abstract/10.1103/PhysRevLett.70.1895

[201] S. Massar and S. Popescu, "Optimal extraction of information from finite quantum ensembles," Physical Review Letters, vol. 74, p. 1259, 1995. [Online]. Available: https://journals.aps.org/prl/abstract/10.1103/PhysRevLett.74.1259

[202] M. Steffen, M. Ansmann, R. McDermott, N. Katz, R. C. Bialczak, E. Lucero, M. Neeley, E. M. Weig, A. N. Cleland, and J. M. Martinis, "State tomography of capacitively shunted phase qubits with high fidelity," Phys. Rev. Lett., vol. 97, p. 050502, Aug 2006. [Online]. Available: http://link.aps.org/doi/10.1103/PhysRevLett.97.050502

[203] J. Gao, J. Zmuidzinas, B. A. Mazin, H. G. LeDuc, and P. K. Day, "Noise properties of superconducting coplanar waveguide microwave resonators," Applied Physics Letters, vol. 90, no. 10, p. 102507, 2007. [Online]. Available: http://aip.scitation.org/doi/full/10.1063/1.2711770

[204] L. Steffen, Y. Salathe, M. Opplinger, P. Kurpiers, M. Baur, C. Lang, C. Eichler, G. Puebla-Hellmann, A. Fedorov, and A. Wallraff, "Deterministic quantum teleportation with feed-forward in a solid state system," Nature, vol. 500, p. 319322, Aug 2013. [Online]. Available: http://www.nature.com/nature/journal/v500/n7462/full/nature12422.html

[205] J. Kelly, R. Barends, A. G. Fowler, A. Megrant, E. Jeffrey, T. C. White, D. Sank, J. Y. Mutus, B. Campbell, Y. Chen, Z. Chen, B. Chiaro, A. Dunsworth, I.-C. Hoi, C. Neill, P. J. J. O'Malley, C. Quintana, P. Roushan, A. Vainsencher, J. Wenner, A. N. Cleland, and J. M. Martinis, "State preservation by repetitive error detection in a superconducting quantum circuit," Nature, vol. 519, pp. 66–69, Mar. 2015. [Online]. Available: http://www.nature.com/nature/journal/v519/n7541/abs/nature14270.html

[206] N. Ofek, A. Petrenko, R. Heeres, P. Reinhold, Z. Leghtas, B. Vlastakis, Y. Liu, L. Frunzio, S. M. Girvin, L. Jiang, M. Mirrahimi, M. H. Devoret, and R. J. Schoelkopf, "Extending the lifetime of a quantum bit with error correction in superconducting circuits," Nature, vol. 536, p. 441, 2016. [Online]. Available: http://www.nature.com/nature/journal/v536/n7617/abs/nature18949.html

[207] C. Eichler, C. Lang, J. M. Fink, J. Govenius, S. Filipp, and A. Wallraff, "Observation of entanglement between itinerant microwave photons and a superconducting qubit," Phys. Rev. Lett., vol. 109, p. 240501, Dec 2012. [Online]. Available: http://link.aps.org/doi/10.1103/PhysRevLett.109.240501

[208] A. Peres, "Separability criterion for density matrices," Phys. Rev. Lett., vol. 77, pp. 1413–1415, Aug 1996. [Online]. Available: http://link.aps.org/doi/10.1103/PhysRevLett.77.1413

[209] R. W. Heeres, P. Reinhold, N. Ofek, L. Frunzio, L. Jiang, M. H. Devoret, and R. J. Schoelkopf, "Implementing a Universal Gate Set on a Logical Qubit Encoded in an Oscillator," ArXiv e-prints, Aug. 2016. [Online]. Available: https://arxiv.org/abs/1608.02430

[210] D. Rugar and P. Grütter, "Mechanical parametric amplification and thermomechanical noise squeezing," Phys. Rev. Lett., vol. 67, pp. 699–702, Aug 1991. [Online]. Available: http://link.aps.org/doi/10.1103/PhysRevLett.67.699

[211] P. Kurpiers, T. Walter, P. Magnard, Y. Salathe, and A. Wallraff, "Characterizing the attenuation of coaxial and rectangular microwave-frequency waveguides at cryogenic temperatures," ArXiv e-prints, Dec. 2016. [Online]. Available: https://arxiv.org/abs/1612.07977

[212] J. Bochmann, A. Vainsencher, D. D. Awschalom, and A. N. Cleland, "Nanomechanical coupling between microwave and optical photons," Nature Physics, vol. 9, no. 11, pp. 712–716, September 2013. [Online]. Available: http://www.nature.com/nphys/journal/v9/n11/full/nphys2748.html

[213] T. Bagci, A. Simonsen, S. Schmid, L. G. Villanueva, E. Zeuthen, J. Appel, J. M. Taylor, A. Sørensen, K. Usami, A. Schliesser, and E. S. Polzik, "Optical detection of radio waves through a nanomechanical transducer," Nature, vol. 507, pp. 81–85, Mar. 2014. [Online]. Available: http://www.nature.com/nature/journal/v507/n7490/full/nature13029.html

[214] R. W. Andrews, R. W. Peterson, T. P. Purdy, K. Cicak, R. W. Simmonds, C. A. Regal, and K. W. Lehnert, "Bidirectional and efficient conversion between microwave and optical light," Nature Physics, vol. 10, no. April, pp. 321–326, 2014. [Online]. Available: http://www.nature.com/nphys/journal/v10/n4/full/nphys2911.html

[215] K. Fang, M. H. Matheny, X. Luan, and O. Painter, "Optical transduction and routing of microwave phonons in cavity-optomechanical circuits," Nature Photonics, vol. 10, no. June, pp. 489–496, 2016. [Online]. Available: http://www.nature.com/nphoton/journal/v10/n7/full/nphoton.2016.107.html

[216] S. A. McGee, D. Meiser, C. A. Regal, K. W. Lehnert, and M. J. Holland, "Mechanical resonators for storage and transfer of electrical and optical quantum states," Phys. Rev. A, vol. 87, p. 053818, May 2013. [Online]. Available: http://link.aps.org/doi/10.1103/PhysRevA.87.053818

[217] P.-L. Yu, K. Cicak, N. S. Kampel, Y. Tsaturyan, T. P. Purdy, R. W. Simmonds, and C. A. Regal, "A phononic bandgap shield for high-Q membrane microresonators," Applied Physics Letters, vol. 104, no. 2, p. 023510, 2014. [Online]. Available: http://dx.doi.org/10.1063/1.4862031

[218] C. Reinhardt, T. Müller, A. Bourassa, and J. C. Sankey, "Ultralow-noise SiN trampoline resonators for sensing and optomechanics," Physical Review X, vol. 6, p. 021001, 2016. [Online]. Available: https://journals.aps.org/prx/abstract/10.1103/PhysRevX.6.021001

[219] R. A. Norte, J. P. Moura, and S. Gröblacher, "Mechanical resonators for quantum optomechanics experiments at room temperature," Physical Review Letters, vol. 116, no. 14, p. 147202, 2016. [Online]. Available: https://journals.aps.org/prl/abstract/10.1103/PhysRevLett.116.147202

[220] M. Arndt, M. Aspelmeyer, and A. Zeilinger, "How to extend quantum experiments," Fortschr. Phys., vol. 57, 2003. [Online]. Available: http://dx.doi.org/10.1002/prop.200900104

[221] W. Marshall, C. Simon, R. Penrose, and D. Bouwmeester, "Towards quantum superpositions of a mirror," Phys. Rev. Lett., vol. 91, p. 130401, Sep 2003. [Online]. Available: http://link.aps.org/doi/10.1103/PhysRevLett.91.130401

[222] I. Pikovski, M. R. Vanner, M. Aspelmeyer, M. S. Kim, and Č. Brukner, "Probing Planck-scale physics with quantum optics," Nature Physics, vol. 8, pp. 393–397, May 2012. [Online]. Available: http://www.nature.com/nphys/journal/v8/n5/full/nphys2262.html

[223] T. Hong, H. Yang, H. Miao, and Y. Chen, "Open quantum dynamics of single-photon optomechanical devices," Phys. Rev. A, vol. 88, p. 023812, Aug 2013. [Online]. Available: http://link.aps.org/doi/10.1103/PhysRevA.88.023812

[224] H. Yang, H. Miao, D.-S. Lee, B. Helou, and Y. Chen, "Macroscopic Quantum Mechanics in a Classical Spacetime," Physical Review Letters, vol. 110, no. 17, p. 170401, Apr. 2013. [Online]. Available: https://journals.aps.org/prl/pdf/10.1103/PhysRevLett.110.170401

[225] Y. Chen, "Macroscopic quantum mechanics: theory and experimental concepts of optomechanics," Journal of Physics B Atomic Molecular Physics, vol. 46, no. 10, May 2013. [Online]. Available: http://iopscience.iop.org/article/10.1088/0953-4075/46/10/104001/meta

[226] A. Bassi, K. Lochan, S. Satin, T. P. Singh, and H. Ulbricht, "Models of wave-function collapse, underlying theories, and experimental tests," Rev. Mod. Phys., vol. 85, pp. 471–527, Apr 2013. [Online]. Available: http://link.aps.org/doi/10.1103/RevModPhys.85.471

[227] A. Großardt, J. Bateman, H. Ulbricht, and A. Bassi, "Optomechanical test of the Schrödinger-Newton equation," Phys. Rev. D, vol. 93, p. 096003, May 2016. [Online]. Available: http://link.aps.org/doi/10.1103/PhysRevD.93.096003

[228] S. G. Hofer, K. W. Lehnert, and K. Hammerer, "Proposal to Test Bell's Inequality in Electromechanics," Phys. Rev. Lett., vol. 116, p. 070406, Feb 2016. [Online]. Available: http://link.aps.org/doi/10.1103/PhysRevLett.116.070406

[229] R. G. Rogers, Low Phase Noise Microwave Oscillator Design. Boston: Artech House, 1991.

[230] B. Efron and R. J. Tibshirani, An introduction to the bootstrap, ser. Mono. Stat. Appl. Probab. London: Chapman and Hall, 1993.

Appendix A

Measurement network

A diagram of the measurement network is shown in Fig. A.1. The network consists of five main parts: A transmon qubit is embedded in a microwave cavity (cQED system) with two ports (Fig. A.1a). The cQED system is connected to an electromechanical device, which is mounted to the base stage of a dilution refrigerator (Fig. A.1b). The center frequency of the electromechanical device is controlled by a voltage bias provided by an actuation line (Fig. A.1c). Microwave pumps and signals are synthesized and used to control and probe both the cQED system and the electromechanical device (Fig. A.1d). Microwave signals are measured using a detector (Fig. A.1e).

A.1 Electromechanical device

The electromechanical device is mounted to the mixing chamber of a dilution refrigerator and cooled to < 25 mK. The construction and operation of the electromechanical device is described in Ref. [65].

A.2 Transmon qubit and microwave cavity

The transmon qubit consists of an Al/AlO_x/Al Josephson junction shunted by a superconducting aluminum coplanar capacitor. This circuit is lithographically fabricated on a single-crystal sapphire substrate and the coplanar capacitor acts as a dipole antenna. The Josephson inductance is approximately 11 nH and the total capacitance is approximately 69 fF.

We embed the transmon qubit in a three-dimensional microwave cavity, as described in

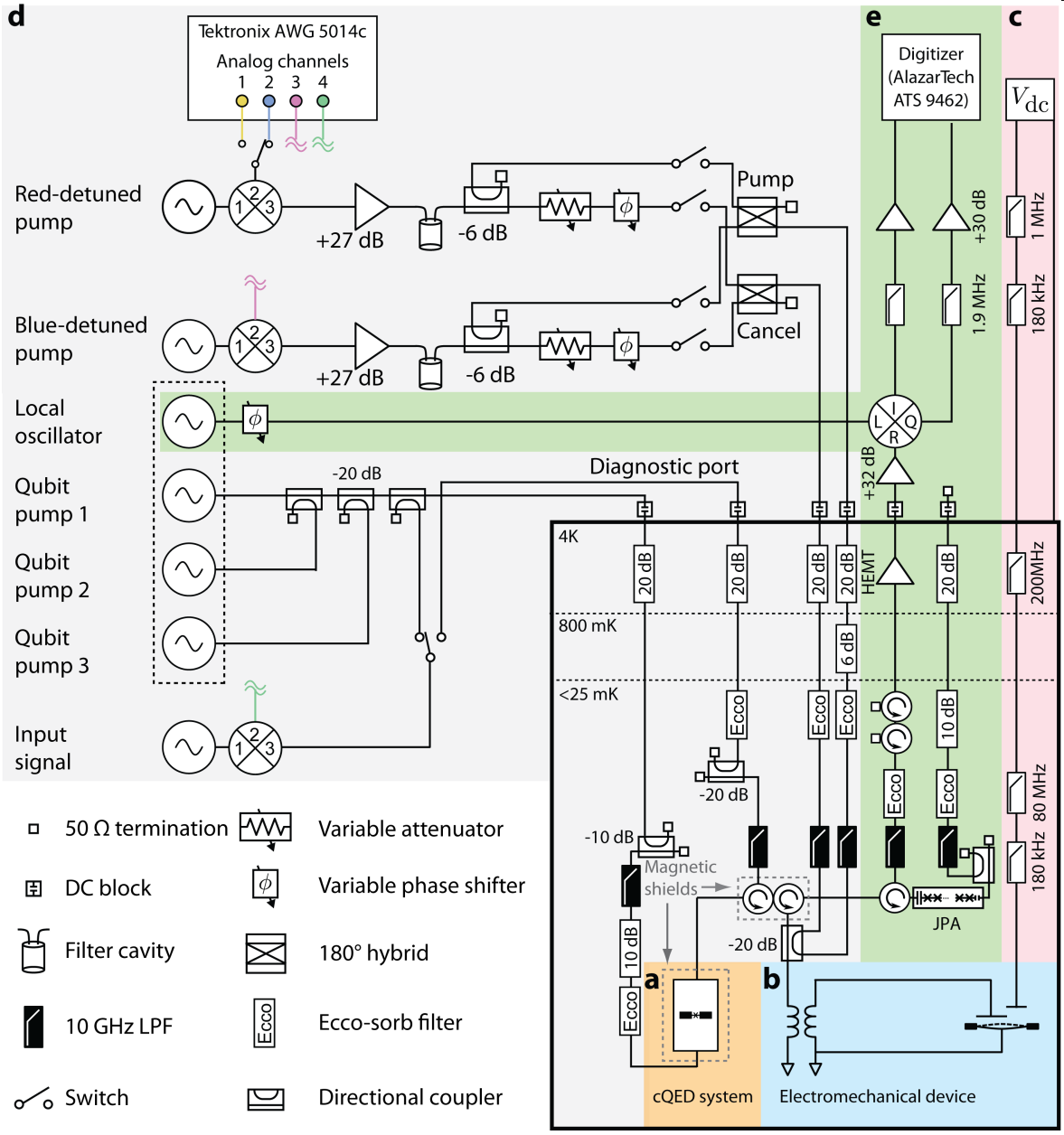

Figure A.1: Detailed schematic of the measurement network. **a,** Circuit quantum electrodynamics (cQED) system. **b,** Electromechanical device. **c,** Actuation line. **d,** Microwave pumps and signal synthesis. **e,** Detector.

Ref. [79]. The cavity is milled from a two pieces of extruded T6061 aluminium and the inner surfaces of the cavity walls are mechanically polished. Two holes that serve as microwave coupling ports are drilled into the cavity. One of the ports is weakly coupled to a pump line, which we use to excite either the qubit or cavity. The other cavity port is strongly coupled to a transmission line

which is routed to components connected to the electromechanical device.

To reduce stray magnetic fields that can affect the qubit's coherence times, we use non-magnetic materials such as copper and brass to construct components that are in close proximity to the qubit and cavity. For additional magnetic shielding, we enclose the cavity in a Cryoperm magnetic shield (Amuneal Manufacturing). At room temperature and inside the magnetic shield, we measure an ambient magnetic field of $\sim$ 20 mG near the cavity. During operation of the experiment, the magnetic shield is wrapped in absorptive microwave material (Eccosorb) and a thin layer (< 100 μm) of aluminium.

Signals emitted from the cavity are routed using copper cables to the input of two low insertion loss circulators and a directional coupler. These custom cryogentic and magnetically shielded circulators (Raditek, Inc.) are used to route signals emitted from the cavity to the electromechanical device, while also providing isolation from the high power (< 1 nW) red- and blue-detuned pumps. At 300 K and near 7.283 GHz, the isolation of the two circulators connected in series was measured to be -43 dB. A similar level of isolation was measured at 4 K. Each circulator is specified by the manufacturer to have an insertion loss of 0.2 dB (at 100 mK). Following the circulators, the output of the directional coupler is connected to the electromechanical device using a superconducting niobium-titanium (NbTi) cable.

A.3 Actuation line

The voltage on the actuation line controls the center frequency of the electromechanical device. A stable and low noise voltage source (Yokogawa 7651) provides a constant $V_{\rm dc}$ during the operation of the experiment. Filtering on the actuation line is nearly identical to the configuration described in Ref. [65].

A.4 Arbitrary microwave pump and signal generation

The red- and blue-detuned pumps at $\omega_{\rm LC}-\omega_{\rm m}$ and $\omega_{\rm LC}+\omega_{\rm m}$, respectively, are generated using two separate microwave synthesizers (Agilent PSG). However, these synthesizers by themselves can-

not produce microwave pulses with programmable temporal envelopes as required by the protocols depicted in Fig. A.2. To generate such pulses, we shape the temporal envelopes of microwave tones emitted by the synthesizers. To this end, we use a double-balanced mixer (Marki MM1-0625HS) driven by waveforms with a programmable amplitude provided by an arbitrary waveform generator (Tektronix AWG 5014c). Waveforms generated by the AWG are shown in Fig. A.2. The shaped microwave pulses have a dynamic range of approximately 50 dB, set by the LO-RF isolation of the double-balanced mixer. Additional isolation (80 dB) is achieved by pulsing off the microwave synthesizers when the pumps are not needed. The shaped pulses are then amplified (Mini-Circuits ZVA-183V) and filtered[229]. Additionally, the pumps have Gaussian-smoothed edges given by a characteristic time of $\sigma_t > 200$ ns. Such smoothed edges reduce spectral content at $\omega_{\mathrm{LC}} \pm \omega_{\mathrm{m}}$ that could drive the mechanical resonator.

The red- and blue-detuned pumps carry enough power that could adversely affect the qubit's state. To reduce the pump power incident on the cQED system, we use variable attenuators and phase shifters to create cancellation signals that reduce the pump power incident on the cQED system by 30 to 40 dB. We monitor and adjust the relative cancellation of the pumps at the detector.

To test the calibration and capture protocols, we inject a large amplitude coherent signal into the electromechanical device (shown in Fig. 5.7). This test signal is generated using a microwave synthesizer, and then shaped using a double-balanced mixer. Its temporal envelope is shown in Fig. A.2. While executing the protocols for the experiments depicted in Fig. 5.7, the test signal was not injected into the network.

Qubit pumps and the experiment's local oscillator (LO) are generated using a set of phase coherent microwave synthesizers (Holzworth HS9002A) that are modulated on and off using the AWG. Two channels of the microwave synthesizers are dedicated to producing the experiment's LO and a pulse at half the qubit's blue sideband transition frequency $\omega_{\mathrm{sb}}/2$. The remaining two channels are dedicated to producing microwave pulses (300 ns in duration) at the qubit's ground to excited state transition frequency ω_{ge}. The phase coherent microwave synthesizers are necessary for

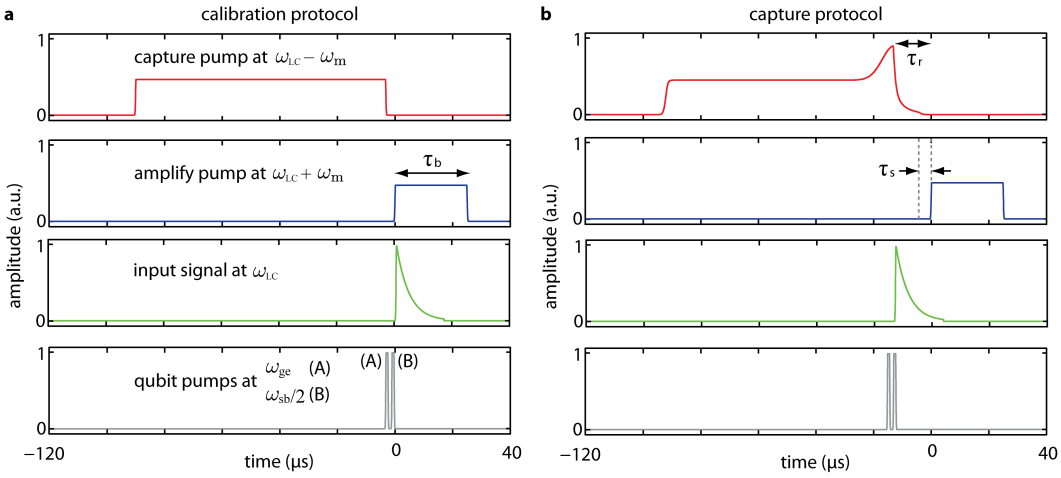

Figure A.2: Temporal envelopes of the microwave pumps and signals. **a,** The timing diagram depicts the calibration protocol. Initially, a red-detuned 'capture' pump at $\omega_{LC} - \omega_m$ cools the motion of the mechanical resonator. After the capture pump turns off, a blue-detuned 'amplify' pump at $\omega_{LC} + \omega_m$ is pulsed on for a duration τ_b. Input signals are coincident with the start of the amplify pump. **b,** The timing diagram for the capture protocol. For this protocol, the red-detuned pump is modulated for optimal capture of a signal with a decaying temporal envelope. The input signals (either generated by the microwave synthesizers or the cQED system) are coincident with the start of the modulation. The programmable storage time τ_s is set by the delay between the end of the capture and the start of the amplification pump.

generating coherent propagating microwave fields (emitted from the cQED system) that encode the state of the qubit. However, these microwave synthesizers have frequency accuracy errors (at the 1 mHz level) that lead to phase drifts relative to the Agilent PSG synthesizers. Additionally, timing errors between the synthesizers and the AWG lead to additional phase errors. To reduce timing errors, all synthesizers are set to frequencies that are integer multiples of the protocol repetition rate (500 Hz). For constant phase drifts due to frequency accuracy errors, we separately measure and correct for such phase drifts after acquiring a set of measurements.

A.5 Detector

Microwave signals incident or reflected off the electromechanical device are measured using a sensitive microwave detector. The detector consists of a Josephson parametric amplifier (JPA), high electron mobility transistor (HEMT) amplifier, a low noise room temperature amplifier (Miteq with

+30 dB gain), a downconverting mixer, and a digitizer. For the protocols presented in Fig. A.2, we use the electromechanical device as the low-noise preamplifier instead of the JPA. The downconverting mixer is driven by a local oscillator detuned by 1 MHz from ω_{LC}, and the inphase and quadrature channels of this mixer are sampled using a high speed digitizer (AlazarTech ATS 9462).

A.6 Strong pumps saturate the JPA

Strong control pumps for the electromechanical device can saturate the JPA. In order to efficiently capture a signal with a power decay rate of $\gamma < 100$ kHz, we use $\Gamma_{\mathrm{r}} > 1$ MHz. For a pump detuning of $\Delta_{\mathrm{r}} = -\omega_{\mathrm{m}}$ and the parameters presented in Table 3.1, achieving such Δ_{r} requires a pump power of ~ 10 nW at the input of the electromechanical device. This power can be reduced by at least 30 dB using cancellation, which results in a power level of ~ 10 pW at the input of the JPA. When operating the JPA near ω_{LC}, its 1 dB compression point is ~ 30 fW in the presence of the red-detuned pump. Thus, we expect the strong pump to saturate the JPA.

In contrast, we do not expect the red-detuned pump to adversely affect the transmon qubit because it is sufficiently isolated from the strong pump. This isolation is at least 40 dB and is primarily provided by the circulators placed between the electromechanical device and the cQED system, as discussed in Appendix A.2. After cancelling the pump, we expect the total reduction in its power to be > 70 dB. Thus, for a ~ 10 nW pump, we expect the power at the input of the cQED system to be ~ 1 fW. For a pump detuning of $\Delta_{\mathrm{r}} = -\omega_{\mathrm{m}}$ and the parameters presented in Table 4.1, we expect the circulating power in the cQED system to be < 0.02 photons. For comparison, non-destructive qubit readout powers are typically at the level of tens of photons. As such, we do not expect the red-detuned pump to significantly affect the cQED system.

Appendix B

Error analysis

B.1 Density matrix estimation

We use a parametric bootstrap method to analyze the statistical error in the density matrix elements estimated by the maximum likelihood (ML) tomography. The estimated density matrix ρ_{est} is used to generate synthetic data sets, and ML tomography is performed on each of the synthetic data sets, building a histogram of values for each density matrix element. Example histograms showing the bootstrapped diagonal density matrix elements for the mixed states obtained using the calibration and capture protocols are shown in Fig. B.1. These histograms reveal an asymmetry in the bootstrapped distributions, as well as bias in some of the density matrix element estimates. It is therefore more appropriate to analyze the statistical error in terms of confidence intervals rather than the standard error. The reported error bars indicate 90% *basic bootstrap* confidence intervals obtained from these histograms [230]. The basic bootstrap confidence interval is obtained as follows: let θ be the estimated parameter and let θ_{lo} and θ_{up} be the lower and upper percentile values obtained from the bootstrapped histogram. That is, θ_{lo} (θ_{up}) is the value for which 5% of bootstrapped values are less than (greater than) θ_{lo} (θ_{up}). The differences $\alpha = \theta - \theta_{\text{lo}}$ and $\beta = \theta_{\text{up}} - \theta$ between the estimated parameter value and the lower and upper percentile values are then inverted around the estimated parameter θ to obtain the confidence interval $[\theta - \beta,\, \theta + \alpha]$.

For each inferred density matrix we create 1,000 synthetic data sets, with each data set containing 102,400 simulated measurement outcomes. The ML tomography algorithm is applied to each synthetic data set with the same number of iterations and Hilbert space truncation as was

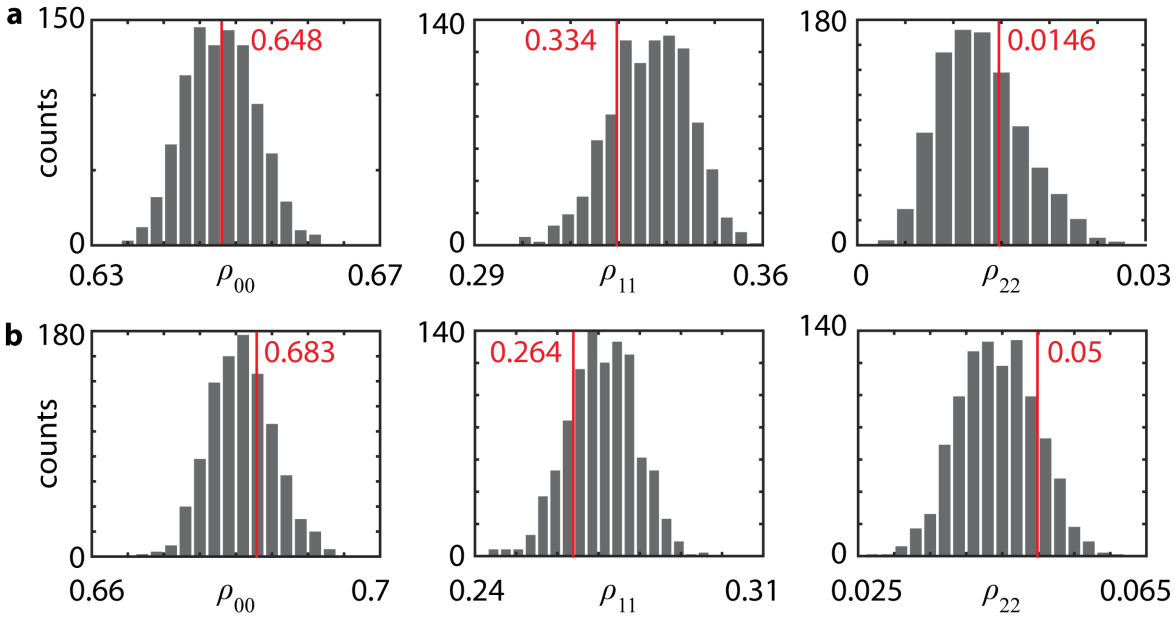

Figure B.1: Bootstrapped histograms. **a,** This figure shows the histograms of the ρ_{00}, ρ_{11}, and ρ_{22} density matrix elements obtained via bootstrapping on the estimated state of the input microwave field in the single photon data set. The red bars indicate the values obtained by ML from the experimental data. Each histogram is obtained by performing ML on 1,000 synthetic data sets with 102,400 measurements each. **b,** This figure shows similar histograms, but for the mechanical resonator state.

used on the experimental data generated by executing either the calibration or capture protocols.

To generate synthetic data sets, we use a Monte Carlo method to sample pairs of joint quadrature values (X_k, Y_k) from the Husimi Q-function $Q(X_k, Y_k)$ corresponding to the estimated density matrix ρ_{est}. A uniformly distributed set of random points (X_k, Y_k) all lying within a sufficiently large radius from the origin in phase space is generated. The Q-function is computed for each of these points, and points are then discarded with probability

$$1 - \frac{Q(X, Y)}{\max_k Q(X_k, Y_k)}$$

so that the remaining points are distributed according to the Q-function. For the data sets obtained from the calibration protocol, the additional thermal noise n_{th} in the mechanical mode must be taken into account. In this case, the measured joint quadrature values are sampled not from the Q-function of the microwave mode, but from the Q-function convolved with the added thermal noise

Table B.1: Estimated density matrix elements assuming different values of n_{th} in the quadrature amplitude scaling and tomography procedures.

n_{th}	$[\rho_{\mathrm{e}}]_{00}$	$[\rho_{\mathrm{e}}]_{11}$	$[\rho_{\mathrm{e}}]_{22}$	$[\rho_{\mathrm{m}}]_{00}$	$[\rho_{\mathrm{m}}]_{11}$	$[\rho_{\mathrm{m}}]_{22}$
0.08	0.655	0.328	0.014	0.694	0.266	0.038
0.09	0.652	0.331	0.014	0.689	0.265	0.044
0.10	0.649	0.334	0.015	0.683	0.264	0.050
0.11	0.645	0.337	0.015	0.677	0.264	0.056
0.12	0.642	0.340	0.015	0.672	0.263	0.062

in the mechanical mode. We account for this added noise in our Monte Carlo sampling method by simply adding Gaussian noise to each sample.

Our finite precision in calibrating the thermal noise in the mechanical mode is a source of systematic error in the tomographic estimate of density matrix elements. Both the procedure for rescaling histograms as well as the tomography assume a mechanical thermal occupancy of $n_{\mathrm{th}} = 0.1$ quanta. We therefore investigate how the density elements would change if the value of n_{th} were different. We let n_{th} range from 0.08 to 0.12 in steps of 0.01, and for each step we obtain the density matrix for both the input electrical and converted mechanical states. The diagonal density matrices obtained with different values for n_{th} are shown in Table B.1. We find that these density matrix elements change linearly and by not more than ~ 0.02 over the range in n_{th} that we explore.

We use Eqn. 5.6 with the diagonal density matrix elements obtained via tomography to calculate $g_{\mathrm{m}}^{(2)} = 0.89$. We use the bootstrap error analysis described in Appendix B.1 to obtain a 90% confidence interval of [0.72, 0.94]. A histogram of bootstrapped values of $g_{\mathrm{m}}^{(2)}$ is displayed in Supplementary Fig. B.2. The density matrix obtained via tomography acts on a truncated Hilbert space with maximum Fock number $n = 15$. While the first 3 diagonal elements are presented in Fig. 5.10, all 16 elements are used in the calculation of $g_{\mathrm{m}}^{(2)}$. These elements rapidly become smaller with increasing n such that both $g_{\mathrm{m}}^{(2)}$ and the bounds of the confidence interval are independent of the Hilbert space truncation. We find that they converge to within 1% of our reported values once $n > 8$.

B.2 Average fidelity calculation

The formula for the average fidelity given by Eqn. 5.15 is actually only true if the process maps all states into a Hilbert space of dimension d, the same dimension as the domain of the process. In our experiment, the weak thermal occupation of the mechanical resonator leads to output states with small but non-zero density matrix elements for $n \geq 2$, in which case truncating the output density matrices to dimension $d = 2$ leads to a systematic overestimation of the average fidelity. We can account for this by using a more general expression F_{avg} which is valid in the case where the process takes states into a higher dimensional space than its domain:

$$F_{\text{avg}} = \frac{d}{d+1}(F_e + A(\mathcal{E})) \tag{B.1}$$

where

$$A(\mathcal{E}) = \frac{1}{d^2}\sum_{ij} \langle i| \mathcal{E}(|j\rangle \langle j|) |i\rangle . \tag{B.2}$$

Eqn. B.1 can be motivated by observing that for a process which does not map states into a higher dimensional space, Eqn. B.2 is a sum of traces of density matrices (which each have unit trace) and Eqn. 5.15 is recovered. That Eqn. B.1 is correct for processes which map states out of their domain can be directly verified for simple processes such as the 'erasure channel,' given by $\mathcal{E}(\rho) = (1-p)\rho + p\,|\psi_{\text{ex}}\rangle \langle\psi_{\text{ex}}|$, where $|\psi_{\text{ex}}\rangle$ is some external state. For our data the correction obtained by using Eqn. B.2 rather than Eqn. 5.15 is small, reducing the average fidelity from 0.84 to 0.83.

We obtain a 90% confidence interval on the value of the average fidelity by a bootstrap analysis similar to the one described in Appendix B.1. We generated 1,000 synthetic data sets, where each data set consists of 20,480 measurement outcomes on each of the four input and output states obtained via tomography. We then run ML on these data sets and compute F_{avg}. A histogram of the results is shown in Supplementary Fig. B.3. Our final result is $F_{\text{avg}} = 0.83$ with a 90% confidence interval of [0.77, 0.86].

To estimate the systematic error in our average fidelity calculation which results from truncating the input Hilbert space dimension, we employ the model of the capture process described

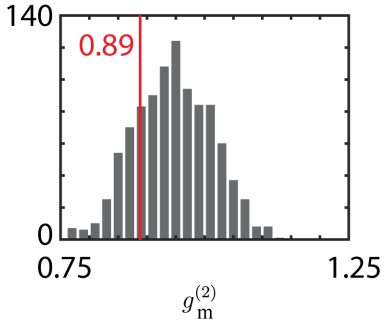

Figure B.2: Bootstrapped histograms of the calculated $g^{(2)}$ function. The figure shows a histogram of $g_{\mathrm{m}}^{(2)}$ for the captured mechanical state, obtained via bootstrapping on the density matrices estimated by ML tomography. The red bar indicates the value calculated from the estimated density matrices. The histogram is obtained by performing ML on 1,000 synthetic data sets with 102,400 measurements each.

in Section 5.5.4. Our model is a process whose average fidelity can be computed exactly; we find $F_{\mathrm{avg}}^{\mathrm{model}} = 0.82$. We then simulate the entire experiment, using the model instead of the physical capture process. Specifically, we use the four known input states to generate synthetic data which we perform tomography on. We then send the estimated states through the model process and use the output states to generate synthetic data which we again perform tomography on, before finally calculating F_{avg}. After 200 repetitions of this procedure we obtain a histogram of average fidelities with mean $\overline{F}_{\mathrm{avg}} = 0.83$. Our estimate of bias is then $\overline{F}_{\mathrm{avg}} - F_{\mathrm{avg}}^{\mathrm{model}} = 0.01$, which is small compared to the width of our 90% confidence interval of [0.77, 0.86].

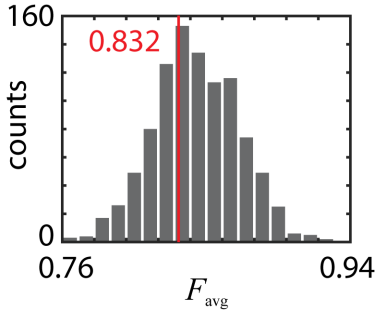

Figure B.3: Bootstrapped histograms of the average fidelity. The figure shows a histogram of average fidelities calculated with 1,000 simulated experiments. Each simulated experiment involves generating a synthetic data set of 20,480 Q-function measurements from the known input and output states given in Supplementary Table B.2. ML tomography is then performed on each synthetic data set and F_{avg} is computed. The red bar indicates the value obtained from the experimental data.

Table B.2: Estimated density matrices used to calculate the average fidelity. The states were estimated using 500 iterations of the RρR algorithm, which yields estimated density matrices of dimension $d = 16$. We present the first 3×3 elements of these matrices. The input states ρ_{e} were estimated from 20,480 measurements of the input microwave fields after executing the calibration protocol. For the capture protocol, measurements of amplified mechanical resonator state yield ρ_{m}. The states labeled with a '1' ('2') correspond to a vacuum (single photon) input. Similarly, states labeled with a '3' and '4' correspond to the an input mixed state of a superposition of zero and one photons, with a phase set by $\varphi = 0$ and $\varphi = \pi/2$, respectively.

Label	**Input state ρ_{e}**	**Mechanical state ρ_{m}**
1	$\begin{pmatrix} 0.994+0.000i & 0.007+0.005i & 0.005-0.026i \\ 0.007-0.005i & 0.004+0.000i & -0.000+0.001i \\ 0.005+0.026i & -0.000-0.001i & 0.001+0.000i \end{pmatrix}$	$\begin{pmatrix} 0.919+0.000i & 0.005+0.001i & 0.010-0.006i \\ 0.005-0.001i & 0.0620+0.000i & -0.016+0.001i \\ 0.010+0.006i & -0.016-0.001i & 0.017+0.000i \end{pmatrix}$
2	$\begin{pmatrix} 0.660+0.000i & -0.013-0.039i & 0.030-0.010i \\ -0.013+0.039i & 0.283+0.000i & 0.040-0.021i \\ 0.030+0.010i & 0.040+0.021i & 0.042+0.000i \end{pmatrix}$	$\begin{pmatrix} 0.636+0.000i & 0.004-0.016i & -0.034-0.008i \\ 0.004+0.016i & 0.281+0.000i & 0.021-0.012i \\ -0.034+0.008i & 0.021+0.012i & 0.075+0.000i \end{pmatrix}$
3	$\begin{pmatrix} 0.826+0.000i & 0.256-0.019i & 0.020-0.003i \\ 0.256+0.019i & 0.173+0.000i & 0.010-0.005i \\ 0.020+0.003i & 0.010+0.005i & 0.001+0.000i \end{pmatrix}$	$\begin{pmatrix} 0.763+0.000i & 0.180-0.035i & 0.018-0.015i \\ 0.180+0.035i & 0.197+0.000i & 0.024-0.011i \\ 0.018+0.015i & 0.024+0.011i & 0.036+0.000i \end{pmatrix}$
4	$\begin{pmatrix} 0.775+0.000i & 0.0451+0.294i & -0.037-0.015i \\ 0.0451-0.294i & 0.217+0.000i & -0.027+0.018i \\ -0.037+0.015i & -0.027-0.018i & 0.006+0.000i \end{pmatrix}$	$\begin{pmatrix} 0.759+0.000i & 0.000+0.21i & -0.031-0.014i \\ 0.000-0.21i & 0.234+0.000i & 0.019-0.017i \\ -0.031+0.014i & 0.019+0.017i & 0.004+0.000i \end{pmatrix}$